UNIVERSITÄT PADERBORN
*Die Universität der Informationsgesellschaft*

Fakultät für
Naturwissenschaften

# Ultrafast nonlinear optics: From spectral to time domain applications

Der Fakultät für Naturwissenschaften
der Universität Paderborn
zur
Erlangung des Doktorgrades
Doctor rerum naturalium
vorgelegt von

Markus Allgaier

There are no mistakes, just
happy little accidents

---

Bob Ross

# CONTENTS

CHAPTER 1

# INTRODUCTION

One of the first experiments that showed the quantum nature of light in the form of non-classical photon number corellations was the Hong-Ou-Mandel interference experiment [1]. Since these early experiments and the birth of quantum optics, the field has long ventured towards applications. By now, quantum states of light can be prepared with a multitude of properties through nonlinear processes [2, 3, 4, 5]. Semiconductor quantum dots can produce indistinguishable photons [6, 7], light-atom interactions can be controlled like never before [8, 9]. Entanglement can be distributed and harnessed in fiber networks [10, 11], and satellites are used for quantum key distribution [12]. With improving storage durations and bandwidth, quantum memories advance steadily towards usability [13, 14]. This astounding process fuels the dream of a globe-spanning "quantum internet" enabling universal quantum communication. But so far, the concept has not even remotely been realized [15]. However, a great many publications acknowledge a crucial piece to the puzzle: No single technology can accomplish all tasks in a quantum network, such as creating photons or photon pairs, distributing, storing, manipulating and finally detecting them. Using different systems instead, together with certain infrastructure for distributing quantum light, makes efficient interfaces necessary. Examples are conversion processes between different quantum systems [16] and conversion for efficiently transporting light with telecom optical fibers [17].

This works deals with the engineering of tailored nonlinear devices necessary to tackle many of the missing pieces in this "quantum infrastructure". Many before this author had set out to design such purposeful devices such as parametric down-conversion sources [18], quantum gates like the Quantum Pulse Gate [19, 20, 21], or even earlier in classical optics [22]. These publications, especially relevant ones for this work, are just examples, since at a basic level any nonlinear device has to satisfy certain criteria to perform its intended function and is therefore in a way "engineered" or "tailored". However, the concept of engineering nonlinear devices on the level of dispersive properties, i.e. "dispersion engineering" is fairly new. In linear optical devices such as optical fibers, methods to control dispersion better have been investigated since the 1980's [23], but were first mentioned in the context of nonlinear devices much later [24, 18]. The reason for the rising popularity of dispersion-engineered nonlinear devices is not just the increasing complexity and variety of tasks in a quantum network, but mainly the necessity of high efficiency, since loss is most intolerable in the world of single photons, from generation [25] to detection of quantum light [26], and anywhere in between [27]. Dispersion-engineered nonlinear devices such as the ones mentioned above have been the subject of three previous theses in this research group [28, 29, 30]. Those works introduce some of the underlying techniques like group-velocity matching and use spectral two-photon intensities to quantify functionality of the device, but focus on a certain device.

This present thesis has two goals. First, after a brief introduction to some of the necessary terms in nonlinear physics in chapter 2, one of the devices developed before, the quantum pulse gate, will be reexamined under more general considerations. In chapter 3, dispersion engineering will be re-introduced as a generalized, but adaptable ”recipe“ with the aim of tailoring devices for diverse applications. After identifying the conceptual parallels with the development of the quantum pulse gate, a number of applications of the same process will be introduced in an attempt to showcase the universal applicability of dispersion engineering. The second goal is to extend the concept of dispersion engineering to time domain applications. In chapter 4, the complete process of dispersion engineering for such an application will be outlined. The device chosen is a frequency conversion device intended for time domain upconversion detection. Considerations regarding spectral and temporal transfer function, conversion efficiency and technologal parameters will be made.

**For the novice**

For the novice who just joined the field and who might set up experiments similar to the ones presented here, each of the four experimental sections in this thesis contains two blue boxes such as this one. The main idea of each experiment is summarized in the first one, before the more detailed explanation in the main text. There are also some general guidelines on how the experiments are aligned. In addition, it might be useful to mention that all the setup sketches presented here are only ”almost“ complete. They contain all of the functional components, but may omit a few mirrors here and there that are necessary to get laser beams from A to B or for beam walking. I hope this information may be useful to the one or other reader.

CHAPTER 2

# FUNDAMENTALS OF ENGINEERING OF NONLINEAR OPTICAL DEVICES

This work concerns itself with the design of nonlinear optical devices. There is an ample supply of textbook literature to help the novice with the introduction into the topic. A brief introduction into photonics, optics, nonlinear optics, waveguides, lasers, optical fibers and detection of light - or in short, everything in the classical optician's toolbox - can be found in [31]. If a more comprehensive introduction into nonlinear optics is needed, it can be found in [32] and [33]. The latter contains an especially helpful compendium of nonlinear and phasematching properties for many materials, indispensable for device design. For a extensive review of the current state of the art of single photon generation and detection, the reader shall be advised to consider [34]. Here, the introduction to nonlinear optics shall be limited to the very basic concepts, and the importance of some aspects for dispersion engineering will be pointed out. First, the nonlinear susceptibility will be introduced. This includes an overview over the nonlinear tensors in commonly used nonlinear materials. Second, the concept of energy conservation, phasematching and quasi-phasematching in the context of nonlinear processes will be discussed. Last, input-output relations will be discussed along with their connection to group velocities and dispersion.

## 2.1. The nonlinear polarization

Nonlinear optics concerns itself with materials with nonlinear response to optical fields. Usually, this response is quantified in the dipole moment per unit volume, the polarization $\vec{P}(\vec{E})$. This polarization depends on the strength of the electric field, and the susceptibility $\chi$. This can in general be expressed as a series:

$$\begin{aligned}\vec{P}(t) &= \vec{P}^{(1)}(t) + \vec{P}^{(2)}(t) + \vec{P}^{(3)}(t) + ... \\ &= \epsilon_0 \left(\chi^{(1)}\vec{E}(t) + \chi^{(2)}\vec{E}^2(t) + \chi^{(3)}\vec{E}^3(t) + ...\right) \qquad (2.1)\end{aligned}$$

where $\epsilon_0$ is the electric constant. Every order of the series is characterized by its own susceptibility constant. Materials, where all $\chi_i$ except $\chi_1$ are negligible, are linear materials. In this work, only second-order nonlinear effects are treated, which means mostly the $\chi^{(2)}$-term is of interest. In the very simple view presented here, the nonlinear susceptibility is treated constant, and the response of the material instantaneous. The polarization is a source of electromagnetic radiation:

$$\nabla\vec{E} - \frac{n^2}{c^2}\frac{\partial\vec{E}}{\partial t} = \frac{1}{\epsilon_0 c^2}\frac{\partial^2\vec{P}}{\partial t^2} \qquad (2.2)$$

where $n$ is the refractive index and $c$ is the speed of light in vacuum. Hence, any nonlinear response of the polarization to an electric field causes ”new“ components to the emission, which depend on the initial electric field in a nonlinear fashion.

It is most important to note that $\chi$ is a material property. This concerns not only the existence of the $\chi^{(2)}$ and $\chi^{(2)}$-terms, but also their strength, and their dependence on the optical polarization direction of the impinging electric field. Therefore, the choice of material with suitable susceptibility is the first parameter of nonlinear process engineering since it influences how strong the desired nonlinear process is, or whether it is possible at all.

## 2.2. Three wave mixing

The processes most important for functional nonlinear devices are sum-frequency generation and difference frequency generation. These processes present the cases, where two different optical fields are mixed to create a third, hence the term three wave mixing. The incident field $E(t)$ is then composed of two fields with amplitudes $E_1, E_2$ at instantaneous frequency $\omega_1, \omega_2$:

$$E(t) = E_1 e^{-i\omega_1 t} + E_2 e^{-i\omega_2 t} \tag{2.3}$$

The second order term of the polarization is therefore

$$\begin{aligned} P(t) &= \epsilon_0 \chi^{(2)} E(t)^2 \\ &= \epsilon_0 \chi^{(2)} \left(E_1 e^{-i\omega_1 t} + E_2 e^{-i\omega_2 t}\right)^2 \\ &= \epsilon_0 \chi^{(2)} \left(E_1^2 e^{-2i\omega_1 t} + E_2^2 e^{-i2\omega_2 t} + 2E_1 E_2 e^{-i(\omega_1 + \omega 2)t} + 2E_1 E_2^* e^{-i(\omega_1 - \omega 2)t}\right) \\ &\quad + 2\epsilon_0 \chi^{(2)} \left(E_1 E_1^* + E_2 E_2^*\right) \end{aligned} \tag{2.4}$$

here, one can identify four terms of interest: The two first terms have instantaneous frequency $2\omega_1$ and $2\omega_2$, respectively. They are associated with second-harmonic generation (SHG). The following two terms are associated with sum-frequency generation (SFG) and difference-frequency generation (DFG). These two terms are most important in tailored nonlinear devices, as they constitute means of shifting the central frequency of an input field $E_1$ by means of a pump field $E_2$ and can in principle be used with an input on the single photon level:

$$P(\omega_1 + \omega_2) = \epsilon_0 \chi^{(2)} E_1 E_2 \quad \text{(SFG)} \tag{2.5}$$

$$P(\omega_1 - \omega_2) = \epsilon_0 \chi^{(2)} E_1^* E_2 \quad \text{(DFG)} \tag{2.6}$$

where the frequency terms have been dropped. For $E_1 = E_2$ we see that SHG is a special case of SFG. Note that negative frequency components exist as well and constitute the complex conjugates of these components. In general, the nonlinear susceptibility depends of the instantaneous frequency on the impinging fields. However, if the frequencies are far from resonance of the material (which is usually the case in the materials and optical frequencies treated here), the susceptibility can be regarded as a constant. However, the susceptibility does depend on the optical polarization of the three involved optical fields, and hence describes the interaction between different components of the optical fields. For SFG this reads (the derivation for DFG is analog):

$$P_i(\omega_3) = \omega_0 \sum_{jk} \left( \chi^{(2)}_{ijk}(\omega_3, \omega_1, \omega_2) E_j(\omega_1) E_k(\omega_2) \right) \tag{2.7}$$

where $(i, j, k)$ notate the kartesian coordinate components $(x, y, z)$. There are complicated symmetry properties associated with the susceptibility tensor $\chi^{(2)}_{ijk}(\omega_3, \omega_1, \omega_2)$, which are described in detail in [32].

## 2.3. The nonlinear susceptibility matrix

In the case of frequencies far from resonance, the susceptibility can be approximated as a constant independent of frequency, and the material as lossless, where the indices and frequencies can be permuted independently. When this condition is valid, the standard literature describes the susceptibility with the $d$-matrix, which is nothing more but half the second-order susceptibility tensor:

$$d_{ijk} = \frac{1}{2} \chi^{(2)}_{ijk} \tag{2.8}$$

where the prefactor is merely a historical convention. For arbitrary frequency permutations, the polarization is then

$$P_i(\omega_n + \omega_m) = \omega_0 \sum_{jk} \sum_{(nm)} \left( 2 d^{(2)}_{ijk} E_j(\omega_n) E_k(\omega_m) \right) \tag{2.9}$$

Now the contracted matrix representation is introduced, which is the standard way of quantifying nonlinear properties of materials in the literature. From the above symmetry assumption follows that the indices $j, k$ can be interchanged, which implies that the input fields can be switched. Then, the possible combinations are relabeled using a new index $l$:

$$\begin{array}{rcl} j,k & \rightarrow & l \\ 1,1 & \rightarrow & 1 \\ 2,2 & \rightarrow & 2 \\ 3,3 & \rightarrow & 3 \\ 2,3;\ 3,2 & \rightarrow & 4 \\ 3,1,\ 1,3 & \rightarrow & 5 \\ 1,2,\ 2,1 & \rightarrow & 6 \end{array} \tag{2.10}$$

The interaction between the field components is then described by

$$\begin{bmatrix} P_x(\omega_3) \\ P_y(\omega_3) \\ P_z(\omega_3) \end{bmatrix} = \begin{bmatrix} d_{11} & d_{12} & d_{13} & d_{14} & d_{15} & d_{16} \\ d_{21} & d_{22} & d_{23} & d_{24} & d_{25} & d_{26} \\ d_{31} & d_{32} & d_{33} & d_{34} & d_{35} & d_{36} \end{bmatrix} \times \begin{bmatrix} E_x(\omega_1)E_x(\omega_2) \\ E_y(\omega_1)E_y(\omega_2) \\ E_z(\omega_1)E_z(\omega_2) \\ E_y(\omega_1)E_z(\omega_2) + E_z(\omega_1)E_y(\omega_2) \\ E_x(\omega_1)E_z(\omega_2) + E_z(\omega_1)E_x(\omega_2) \\ E_x(\omega_1)E_y(\omega_2) + E_y(\omega_1)E_x(\omega_2) \end{bmatrix} \tag{2.11}$$

The $d$-matrix changes into an effective matrix $d_{eff}$ depending on the orientation of crystal axes, and may simplify depending on the crystal symmetry of the nonlinear material. In this work, only Lithium Niobate (LN) and Potassium Titanyl Phosphate (KTP) are used. Their crystal structures are part of symmetry group $3m$ (LN) and $mm2$ (KTP)[33] and therefore, purely derived from symmetry reasons, their $d$-matrices take the form

$$d = \begin{pmatrix} 0 & 0 & 0 & 0 & d_{31} & -d_{22} \\ -d_{22} & d_{22} & 0 & d_{31} & 0 & 0 \\ d_{31} & d_{31} & d_{33} & 0 & 0 & 0 \end{pmatrix} \quad \text{(LN)} \tag{2.12}$$

$$d = \begin{pmatrix} 0 & 0 & 0 & 0 & d_{15} & 0 \\ 0 & 0 & 0 & d_{24} & 0 & 0 \\ d_{31} & d_{32} & d_{33} & 0 & 0 & 0 \end{pmatrix} \quad \text{(KTP)} \tag{2.13}$$

In reality, the values for LN depend highly on the manufacturing parameters and, to some extent, on frequency. The same is true for KTP. Since it is difficult to directly calculate the nonlinear efficiency of such a three wave mixing process from the entries of the d-matrix, the values are more useful for comparison of different processes and materials. For example, the $d_{33}$-component of LN, associated with a SFG or DFG process where all fields have the same optical polarization, is almost 10 times as high as a $d_{31}$-process, where the polarizations are different. However, such a process may have other advantages, as will be discussed later in chapter 3. At the same time, the $d_{31}$ of LN is about twice as big as the same matrix element for KTP.

For a LN crystal grown in a stoichiometric melt, the matrix at $\lambda = 2\pi c/\omega = 1058\,nm$ entries are:

$$\begin{aligned} d_{22} &= 2.46 \pm 0.23 pm/V \\ d_{31} &= -4.64 \pm 0.66 pm/V \\ d_{33} &= -41.7 \pm 7.8 pm/V \end{aligned} \tag{2.14}$$

For KTP, measured at $\lambda = 1064\,nm$ the values are:

$$\begin{aligned} d_{15} &= 1.9 \pm 0.1 pm/V \\ d_{24} &= 3.7 \pm 0.2 pm/V \\ d_{31} &= 2.2 \pm 0.1 pm/V \\ d_{32} &= 3.7 \pm 0.2 pm/V \\ d_{33} &= 14.6 \pm 0.7 pm/V \end{aligned} \tag{2.15}$$

These values and more extensive tabulations of such material properties can be found in [35]. Basically, these tabulations are a most important ingredient in developing a tailored nonlinear process. In chapter 3 the importance of choice of material and polarization for different applications will be discussed in detail.

The third order nonlinear susceptibility will not be discussed here, but it is noteworthy that the two materials here do have a weak third order nonlinearity. It mostly manifests in spurious, unwanted processes only visible at high pump powers.

## 2.4. Properties of the generated field and phasematching

Up to now, there might be the impression that every process, as long as there is a sufficiently large entry in the $d$-matrix, will happen. This is not true. Indeed, as long as there is a sufficiently large entry in the $d$-matrix, there will be a corresponding response of the polarization. However, frequency conversion like SFG will only happen, if there is a field at $\omega_3$ emitted. The conditions for which this is possible, i.e. the so-called phasematching, will be discussed here.

In general, the generated field is described by equation 2.2, while the complex nature of the nonlinear polarization in anisotropic materials has to be considered. To make matters easier, we restrict this derivation to the cases actually treated in this thesis. Waves shall be confined to waveguides, which implies a propagation direction which is constant and identical for all three fields. The two fundamental fields shall be considered quasi-monochromatic pulses of light. This means, that the pulses cannot be considered long enough, i.e. not longer than the nonlinear medium, to be described as a continuous wave signal. Instead, they are described only as *quasi*-monochromatic, centered around a central frequency $\omega_0$. Such a field will be described by

$$\vec{E}(r,t) = \vec{E}(\vec{r},t)e^{-i\omega t} + c.c. \tag{2.16}$$

where $E(r,t)$ describes both polarization and amplitude of the field. This is broken down to

$$\vec{E}(\vec{r},t) = \hat{e}A(\vec{r},t)e^{i\vec{k}\cdot\vec{r}} \tag{2.17}$$

where $\hat{e}$ points in the direction of the electric field, $\vec{k}$ is the wave vector pointing in direction of propagation, and the amplitude $A(\vec{r},t)$ is considered to be slowly varying. This implies that the amplitude varies much slower than the oscillation of the field in both space and time, which restricts the pulse length to sufficiently long (many cycle) pulses. For a quasi-monochromatic pulse, the amplitude is centered around $\omega_0$, and the propagation is to be considered along $z$ direction:

$$A(\vec{r},t) = A_{\omega_0}(\vec{r},t) = A_{\omega_0}(z,t) \tag{2.18}$$

Further we now assume that all fields are monochromatic (the effect of violating this assumption will be discussed later) and infinite in lateral direction. Propagation direction shall be along a principal crystal axis. After all, the following simplification can be made:

$$\nabla^2 \to \frac{d^2}{dz^2}; \quad \frac{\partial^2}{\partial t^2} \to -\omega^2; \quad \frac{d^2\vec{E}}{dz^2} \to \hat{e}\left(-k^2A + 2ik\frac{dA}{dz}\right)e^{ikz} \tag{2.19}$$

The assumption of cw-fields is reasonable from a intuitive standpoint. The phasematching or other crystal properties may not depend on the shape of the spectra of the fields, i.e. the phasematching for a cw process has to be the same as for a pulsed process. Every combination of frequency components has hence its own wave equation.

Here, only the calculation for SFG will be shown, for DFG it follows in the same fashion. For SFG, the terms of the second order nonlinear polarization with field indices $s, p, i$ (signal or input, pump, and idler or output) are then

$$P_i^{(2)} = 4\epsilon_0 d_{eff} A_s A_p e^{i\Delta kz}; \quad P_{s,p}^{(2)} = 4\epsilon_0 d_{eff} A_i A_{p,s}^* e^{i\Delta kz} \tag{2.20}$$

with the phasemismatch

$$\Delta k = \hat{z}\left(k_s + k_p - k_i\right) \tag{2.21}$$

The calculation of the effective $d$-matrix simplifies if the waveguide coincides with a crystal axis, which is usually the case, or even necessary for technological reasons of waveguide fabrication. The coupled wave equations follow:

$$\frac{dA_i}{dz} = i\frac{2\omega_i}{n_i c} d_{eff} A_s A_p e^{i\Delta kz} \tag{2.22}$$

$$\frac{dA_s}{dz} = i\frac{2\omega_s}{n_i c} d_{eff} A_i A_p^* e^{-i\Delta kz} \tag{2.23}$$

$$\frac{dA_p}{dz} = i\frac{2\omega_p}{n_i c} d_{eff} A_i A_s^* e^{-i\Delta kz} \tag{2.24}$$

where the intensity $I$ and power $P$ at a certain position is

$$I_{s,p,i} = \frac{n_{s,p,i} c}{2\pi} \left|A_{s,p,i}\right|^2; \quad P_{s,p,i} = \int_C I_{s,p,i} dC \tag{2.25}$$

where the integration is performed over the area $C$ of the beam cross section. The solutions are given in terms of conversion efficiency $\eta = P_i/P_s$ in the limit of an undepleted pump according to [36].

$$\eta_i = \frac{P_i}{P_s} = \frac{8\pi^2 d_{eff}^2 L^2 I_p}{\epsilon_0 n_p n_s n_i c \lambda_i^2} \frac{\sin^2(\Delta kL/2)}{(\Delta kL/2)^2} \tag{2.26}$$

This equation contains contributions of the phasemismatch $\Delta k$, but only in the last term, which also depends on the crystal length $L$. If the dependence of $\eta_i$ on the phasemismatch is evaluated, it follows exactly this mentioned *sinc*-dependence. In other words: Far from phasematching $\Delta k = 0$, the conversion efficiency is zero. In materials with dispersion, this is a relatively complicated relation, since $k$ depends on frequency:

$$\omega = \omega(k) \tag{2.27}$$

Furthermore, the above dispersion relation is different for each polarization. With the vacuum wavelength $\lambda_0 = 2\pi c_0/\omega_0$ the wavenumber with dispersion reads

$$k = k_0 n(\omega) = \frac{2\pi}{\lambda_0} n(\omega) \tag{2.28}$$

This notation is the most common, since opticians hardly use the wavelength inside the medium to discribe a field, but rather the vacuum wavelength $\lambda_0$, which will simply be called $\lambda$ through the rest of this thesis.

We can see that, in general, the phasemismatch is non-zero for most wavelength combinations. This is usually compensated for by using a technique called quasi-phasematching. Periodically inverting crystal domains with high voltage creates a grating. This grating with period $\Lambda$ supplies an additional phase component:

$$\Delta k = \frac{2\pi}{\lambda_s} n_s(\omega_s) + \frac{2\pi}{\lambda_p} n_p(\omega_p) - \frac{2\pi}{\lambda_i} n_i(\omega_i) + \frac{2\pi}{\Lambda} \tag{2.29}$$

This can be understoof in the following way: Exactly at the point where signal and pump field would go out of phase, the inverted crystal domains forces the fields in phase again. Employing quasi-phasematching allows to shift the phasematched wavelength at will, as long as the necessary grating period is within the capabilities of fabrication. It is noteworthy that the above equation can be rewritten in terms of phase-velocity:

$$\Delta k = \frac{\omega_s}{v_{P,s}} + \frac{\omega_p}{v_{P,p}} - \frac{\omega_i}{v_{P,i}} + \frac{2\pi}{\Lambda} \tag{2.30}$$

Therefore, phasematching means matching inverse phase velocities, weighted by frequency, whereas the group velocity, $v_G = \partial\omega/\partial k$ characterizes the direction of shift of the phasematching point. The following section will outline, what this actually means. Many nonlinear materials are also birefringent, i.e. every polarization is associated with a distinct dispersion curve. This makes it useful to characterize the combinations of polarizations used, since it allows to quickly identify which dispersion curves are used for which field. With horizontal ($H$) and vertical polarization ($V$), the different processes are usually identified as

$$\begin{aligned} \text{Process}:&\quad s\ \ p \rightarrow i \\ \text{Type}-0:&\quad H\ H \rightarrow H \\ \text{Type}-0:&\quad V\ V \rightarrow V \\ \text{Type}-\text{I}:&\quad H\ V \rightarrow H \\ \text{Type}-\text{I}:&\quad V\ H \rightarrow V \\ \text{Type}-\text{II}:&\quad V\ H \rightarrow H \\ \text{Type}-\text{II}:&\quad V\ V \rightarrow H \\ \text{Type}-\text{II}:&\quad H\ H \rightarrow V \\ \text{Type}-\text{II}:&\quad H\ V \rightarrow V \end{aligned} \tag{2.31}$$

Or in other words: In a type-0 process, all fields are in the same polarization, for type-I the pump is differently polarized than the signal and idler fields, and for type-II, signal and idler have different polarization.

## 2.5. The transfer function

The functionality of a frequency conversion device is in large parts described in terms of a spectral transfer function $\Psi(\omega_s, \omega_i)$. It yields the conversion efficiency, at least up to a multiplicative factor, as a function of input and output frequency. In the quantum or single photon picture, it is frequently called two-photon intensity, or joint spectral amplitude. This description has been used for many tailored nonlinear devices so far, especially parametric down-conversion sources[18, 37, 38], but also SFG [19].

There are two things that play into this transfer function: The pump function $P(\omega_s, \omega_i)$ and the phasematching function $\Phi(\omega_s, \omega_i)$:

$$\Psi(\omega_s, \omega_i) = \Phi(\omega_s, \omega_i) \cdot P(\omega_s, \omega_i) \tag{2.32}$$

where $\Phi$ is merely the previously given efficiency as a function of $\omega_s, \omega_i$. This dependence manifests in the phasematching term. $\Delta k$ depends on three frequencies $\omega_s, \omega_p, \omega_i$, but the pump frequency is defined by the other two via $\omega_p = \omega_i - \omega_s$. The pump function is defined by the spectrum of the pump field. For example, for a cw pump it reads:

$$P(\omega_s, \omega_i) = \delta(\omega_i - \omega_s - \omega_p) \tag{2.33}$$

For a gaussian spectrum with standard deviation $\sigma_p$, it reads:

$$P(\omega_s, \omega_i) = \exp\left(-\frac{(\omega_i - \omega_s - \omega_p)^2}{2\sigma_p^2}\right) \tag{2.34}$$

Note that this spectrum is not scaled with any pump power or similar. As said before, the transfer function describes the efficiency up to a factor. When actual conversion efficiency instead of relative efficiency is described, one usually quantifies it for cw inputs in the center of the distribution.

The phasematching function is

$$\Phi(\omega_s, \omega_i) = \frac{\sin^2(\Delta k(\omega_s, \omega_i) L/2)}{(\Delta k(\omega_s, \omega_i) L/2)^2} \tag{2.35}$$

with

$$\Delta k = \frac{\omega_s}{c_0} n_s(\omega_s) + \frac{\omega_i - \omega_s}{c_0} n_p(\omega_i - \omega_s) - \frac{\omega_i}{c_0} n_i(\omega_i) + \frac{2\pi}{\Lambda} \tag{2.36}$$

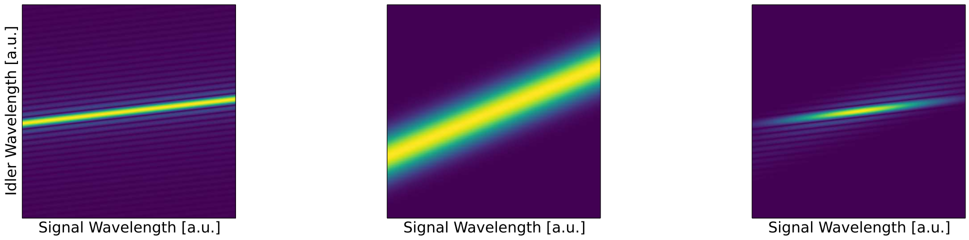

Figure 2.1.: Phasematching, pump and transfer function for a type-0 SFG process in Lithium Niobate.

For parametric down-conversion (PDC), these functions change in so far that they describe the spectral correlations between two generated photons, which is not a transfer function. The definition in terms of the frequencies changes to $\omega_i + \omega_s = \omega_p$. This definition is also valid for DFG.

In Figure 2.1, phasematching, pump and complete transfer function for an exemplary SFG process are shown. There are three distinct features to characterize such a transfer function: Phasematching and pump bandwidth, as well as the phasematching angle. This angle is connected to the dispersive properties of the used material, and in general describes the ratio between the steepness of the group-velocity curves at the signal and idler point. Since the phasematching point, i.e. the combination of frequencies at which $\Delta k = 0$, depends on the frequencies, the steepness at each point, $\omega_s$ and $\omega_i$ is

$$\frac{\partial \Delta k}{\partial \omega} = \frac{\partial}{\partial \omega}\left(k_s + k_p - k_i\right) \tag{2.37}$$

$k_s$ and $k_i$ only depend on the respective signal and idler frequencies, whereas $k_p$ depends on both, since $\omega_p = \omega_i - \omega_s$:

$$\frac{\partial \Delta k}{\partial \omega} = \frac{\partial k_s}{\partial \omega_s} + \frac{\partial k_p}{\partial \omega_s} \tag{2.38}$$

The idler behaves similarly:

$$\frac{\partial \Delta k}{\partial \omega_i} = \frac{\partial k_p}{\partial \omega_i} - \frac{\partial k_i}{\partial \omega_i} \tag{2.39}$$

Equations 2.38 and 2.39 are the two components of the vector

$$\begin{pmatrix} \frac{\partial}{\partial \omega_s} \\ \frac{\partial}{\partial \omega_i} \end{pmatrix} \Delta k \tag{2.40}$$

which is oriented at angle $\alpha$ towards the horizontal (signal) axis:

$$\alpha = \arctan\left(\frac{\frac{\partial k_p}{\partial \omega_i} - \frac{\partial k_i}{\partial \omega_i}}{\frac{\partial k_s}{\partial \omega_s} + \frac{\partial k_p}{\partial \omega_s}}\right) \tag{2.41}$$

In an analog fashion, the pump function is also oriented at an angle, but since it describes energy conservation and links signal and idler frequency in any three wave mixing process, it is always oriented at $45°$ (SFG) or $-45°$ (PDC and DFG).

This equation is associated with so-called group-velocity matching, since $v_G = \frac{\partial \omega}{\partial k}$. From a engineering perspective, the phasematching angle is of great importance for device functionality: Depending on the angle, input spectra are compressed or stretched, preserved, or such information may be erased to some extent for angles of $0°$ or $90°$. The transfer function for DFG and SFG processes holds much influence on the device functionality. It functions as a spectral input aperture, maps input to output spectrum, and defines the wavelength combination at which the device functions. "Dispersion engineering" of a tailored device means shaping the transfer function in order to achieve a certain device functionality. This implies taking control of the transfer function in any way possible: Pump spectrum, crystal length, material, polarizations, periodic poling, waveguide dispersion. In the sense of the word, engineering does not mean to harness a certain device property for functionality, but to specifically produce that necessary property.

## 2.6. Quantum frequency conversion

The quantum description of frequency conversion could be described in great detail, but this would not give any new insight to dispersion engineering. In previous attempts on the topic, while the quantum picture was described in depth, the actual "engineering" part, i.e. the choice of appropriate phasematching conditions, was done purely from a classical point of view [29, 30]. This was possible because true quantum effects such as time ordering were neglected. Basically, in the limit of low conversion efficiency, the quantum device behaves exactly the same as a classical device, except that conversion probability takes the role of conversion efficiency. On the other hand, the effects that take place at high conversion efficiency, do hardly ever contribute to a useful behavior of the device. In chapter 4 a brief outlook with numerical examples will be given, where such effects will be shown and options to account for them at the stage of device engineering will be discussed.

Let's begin to formulate a frequency conversion process, e.g. SFG, in the quantum picture. The aspiring doctoral student may have noticed during theoreticians' talks that quantum mechanics usually takes place when one can write down the Hamiltonian associated with whatever one wants to describe. The Hamiltonian for a quantum frequency conversion is usually described in the literature [19] under assumption of a bright, classical pump far from depletion as

$$H = \int dt\hat{H}(t) = \theta \iint d\omega_s d\omega_i \Psi(\omega_s, \omega_i)\hat{a}(\omega_s)\hat{c}^\dagger(\omega_i) + \text{h.c.} \tag{2.42}$$

where $a$ is the signal mode and $c$ is the idler mode, $\theta$ is a constant describing the efficiency of the process, and $\Psi(\omega_s, \omega_i)$ is the same transfer function described in the previous section. It appears that under suitable approximations the quantum mechanical description of SFG merely replaces the mapping between electric fields with mapping between ”modes“, however with the same classical transfer function derived from classical field equations. This fact should not be surprising, because these mentioned ”approximations“ allow to exclude all true quantum effects. The authors of [19] continue to use the classical transfer function to describe a functional quantum frequency conversion device, but use broadband spectral modes

$$\hat{A}_0^\dagger \left|0\right\rangle = \int d\omega \xi_0(\omega)\hat{a}^\dagger \left|0\right\rangle \tag{2.43}$$

where $\xi_i$ describes the spectral envelope of the mode of order $i$. The only requirement on the spectra $\xi_i$ is that they form a orthonormal basis, i.e. $\int d\omega\xi_i(\omega)\xi_i(\omega) = \delta_{i,j}$. It is noteworthy that this description is a fundamental step forward from the predominant description of photons using monochromatic modes, since it allows to describe the quantum mechanical object that a photon is with the same spectral envelope functions as the corresponding electric field. However, it also makes it even more apparent that the quantum mechanical description of frequency conversion and its impacts on dispersion engineering are all too similar to its classical counter part, and it only appears unique when done unaware of the classical theory of light.

For sake of completeness, it has to be mentioned that some of the approximations commonly performed in the literature, are some that appear to be invalid or easily violated under realistic conditions. The first one is the so-called ”no time-ordering“-approximation, which essentially means ignoring that the Hamiltonian (not the time-integrated one!) depends on time, since there is already something generated in the idler mode as the fields advance through the medium [39, 40]. To analyze this effect, a modal decomposition of the transfer function is performed. The parameter $\theta$ is evaluated for each mode. Without the mentioned approximation, $\theta$ has a different dependency on pump power in general, and more specifically it has a different dependency on pump power for every mode. This can be interpreted as a pump power dependent transfer function.

# CHAPTER 3

# DISPERSION ENGINEERING REVISITED

This chapter will cover the early beginnings of tailoring nonlinear processes aimed at performing a certain task. This usually involves looking for advantageous relations of parameters such as pulse walk-off, interaction length and spectral correlations, all of which are linked through the dispersive properties of the material used. Thus, the process of tailoring processes by choosing these parameters appropriately has been dubbed dispersion engineering. The first example in the literature of dispersion engineered devices are decorrelated parametric down-conversion photon pair sources [18, 2]. These sources generate decorrelated photon pairs in pure states, advantageous for certain applications in quantum optics [34]. A second device that employs the concept is the Quantum Pulse Gate (QPG), developed in parallel in this group [19, 41, 20, 42, 21], and by Raymer *et al.* [43, 44, 45], and has since become a joint effort [46]. While the author of this thesis was not immediately involved in the development of the QPG, the state of the art and the contributions of others will be summarized here in the next two sections, which cover the methods of dispersion engineering in general, and the working principle of the QPG. After that, three of the applications of the same tailored process used for the QPG outline the work of your author. The manuscripts describing these two contributions to the field were previously published: Spectral bandwidth compression inherent to the nonlinear process offers the possibility of interfacing different quantum systems [47]; Optical cross-correlation measurements offer efficient and quick characterization of the temporal intensity envelope and pulse duration of single photons [48]. Finally, the reverse process of the Quantum Pulse Gate, intended for efficient spectral reshaping of single photons for quantum communication purposes, will be outlined.

## 3.1. Methods

In this thesis, the discussion of tailored nonlinear devices will be limited to nonlinear waveguides, bulk nonlinear optics are not considered. The methods used in previously developed tailored devices will be reviewed here. Dispersion engineering is not a very well defined term, and there is no fixed recipe how to tailor a nonlinear process. There are two different classes of devices we can engineer in general: Frequency conversion devices like the QPG, or photon pair sources. All other imaginable devices such as second harmonic generators or optical parametric amplifiers fall in one of these two categories. The order of questions to answer then depends on whether one wants to design a pair source or frequency converter. For a photon pair source the following aspects have to be considered:

- What kind of spectral correlations are required?
- What wavelength combination is desired?

- What bandwidth should the generated photons have?
- Should the photons be distinguishable or indistinguishable in any degree of freedom?

These requirements can be addressed by choice of material, polarizations, pump pulse spectrum and waveguide lengths. If the same polarization is required, one can choose a type-0 or type-I process. In order to produce identical spectra, one needs to achieve both degenerate central wavelength and certain spectral correlations. The central wavelength is dictated by energy and momentum conservation:

$$E_s + E_i = E_p; \quad E_j = h\frac{\lambda_j}{c} \tag{3.1}$$

For PDC, the output wavelengths are therefore not clearly defined from energy conservation alone. Momentum conservation dictates:

$$k_s + k_i + k_{QPM} = k_p \tag{3.2}$$

where $k_{QPM}$ is the offset to the phasematching produced by periodically poling a nonlinear crystal. Since $k$ depends on wavelength (all materials are dispersive in general - which describes exactly the issue of frequency dependent wavenumber), not all wavelength combinations are phasematched, and one has to tune the phasematching to the desired point using periodic poling.

In regard of creating spectra identical in shape, we have to consult the joint spectral amplitude of the produced pair state. Two examples of joint spectral intensities (spectral phase correlations are hard to measure on the single photon level) are shown in Figure 3.1. The state in Figure 3.1a is decorrelated and degenerate: The photons have identical central wavelength and the spectra have identical shape and bandwidth. Panel b shows an anti-correlated state produced with the same source. While the central wavelength is identical, a narrower pump spectrum introduces spectral anti-correlation, which creates entanglement [49]. The source used here [2], has a peculiar phasematching angle close to 45°, which allows to select the amount and type of spectral correlations by changing the pump bandwidth. The main influence of correllations can be seen when one of the photons is *heralded*: One photon is detected, which tells the experimenter that the second photon is present as well and a pair has been generated. If now the detection of the heralding photon happens in a frequency resolved way, the detection frequency also sets the central frequency of the heralded photon, unless the source is decorrelated. In this case, the spectrum of the heralded photon is independent of the heralding measurement.

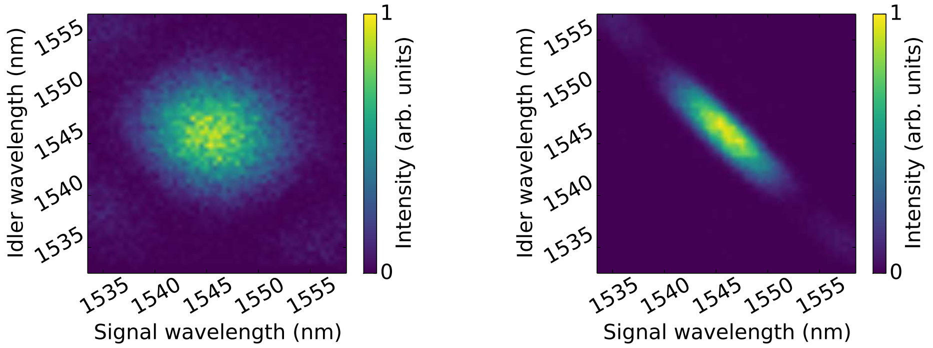

Figure 3.1.: Measured joint spectral intensities of a decorrelated PDC state (left), where the emitted photons are identical in both central wavelength and bandwidth, and an anti-correlated state, where the central wavelength and marginal spectrum are identical, but there is spectral anti-correlation.

Correlations can be introduced by either tight phasematching or tight pump function. On the other hand, decorrelation requires a certain symmetry between pump and phasematching, which will be treated in more detail in chapter 4.2.4. The phasematching angle $\alpha$ that makes this possible is linked to the group-velocities of the material:

$$\alpha = \arctan\left(\frac{\frac{\partial k_p}{\partial \omega} - \frac{\partial k_s}{\partial \omega}}{\frac{\partial k_p}{\partial \omega} - \frac{\partial k_i}{\partial \omega}}\right) \tag{3.3}$$

This relationship becomes clear from geometric considerations in the time domain: The group velocity difference between pump and signal, and pump and idler, respectively, correspond to pulse walk-off in the waveguide. The ratio between the two defines the relative walk-off, which corresponds to a relative uncertainty when the generation occurs. This relationship defines the joint temporal amplitude. The different corresponding phasematching conditions and pulse walk-offs have been discussed in detail in [29].

Therefore, whether it is possible to achieve a certain type of spectral correlation at a certain wavelength combination apparently depends on the dispersive properties of the material. Thus, the most influential ingredient for dispersion engineering of PDC sources is the choice of material. Dispersion curves of three common nonlinear materials supporting waveguides are shown in Figure 3.2. The above shown phasematching conditions were achieved in type-II processes, where the signal and idler are in different polarization. Therefore, the temporal walk-offs are not only dictated by dispersion, but also by the birefringence. It is visible that the three different materials have hugely different

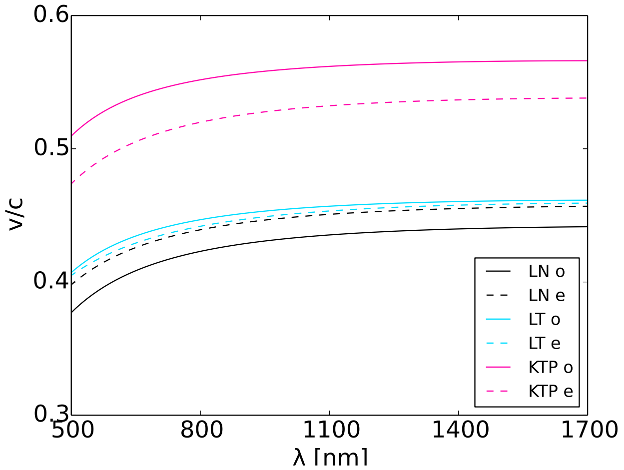

Figure 3.2.: Group velocityies of $LiNbO_3$ (black lines), KTP (magenta lines) and $LiTaO_3$ (turquoise lines)

birefringence. A combination of polarizations and wavelengths will yield hugely different phasematching angles in a different material.

Beyond the spectral correlations, the ratio between phasematching and pump bandwidths is tantamount to the output bandwidth.

In recent years, different types of sources have been implemented. Beside decorrelated, degenerate, identical-spectrum sources like the one used as an example here [18, 2], a decorrelated, non-degenerate, variable-spectrum source has been implemented in unpoled KTP waveguides [3]. Typical sources in Lithium Niobate can be bonded to fiber pig-tails [5] and have a correlated spectrum. Since waveguides in these common nonlinear materials are in general weakly guiding, the waveguide structure modifies the bulk dispersive properties only slightly, thus the choice of material, polarization and wavelength combination remains the most important tool for dispersion engineering of photon pair sources.

For SFG, the matter is more complicated. Some questions are analog, like the question of spectral or temporal correlations between input and output photon. Polarization plays a minor roll compared to PDC and can usually be used as a means of achieving certain phasematching or group velocity relations between the involved fields. The most important task however is, whether the converted light is to be preserved in some degree of freedom, altered, or whether the conversion should even serve as a means of measurement.

Designing an appropriate process is easiest, if some wavelength are freely adjustable. If the wavelength combination is already dictated by the application, once again the choice of polarization and material are the most crucial to establish the necessary spectral or temporal correlations. One example of an application with fixed wavelength combination is interfacing two systems with defined wavelength, like a quantum memory and a photon pair source. Such an interface [47] will be discussed in section 3.3. In general, a systematic way to design any process would be the following: First, identify the necessary spectral and temporal correlations (equivalent to the input-output transfer function). For any frequency conversion process (both SFG and DFG) it will be defined to three quantities:

- Phasematching angle
- Phasematching bandwidth
- Pump bandwidth

The first two are then connected to technological parameters, the group velocities (equation 3.3, Figure 3.2) and sample length (which define the phasematching bandwidth), as already discussed in chapter 2. Then, once the appropriate group-velocity relations are identified, one can check whether the necessary group-velocity matching is possible with the desired wavelength combination, or - if the wavelengths can at least partially be freely selected - select an appropriate combination. This ultimately leads to a set of parameters for manufacturing the final device: Material, sample length and poling period.

In this work, dispersion engineering for frequency conversion processes will be discussed in two different ways. First, an example for a dispersion engineered nonlinear device, the Quantum Pulse Gate will be explained. Afterwards, different applications of the same nonlinear process and the subtleties of the specific requirements of these applications will be discussed.

## 3.2. The quantum pulse gate

In this section the Quantum Pulse Gate (QPG), developed previously in this group [19, 41, 20, 42, 21] and by Raymer *et al.* [43, 44, 45] will be discussed in some more detail. The QPG is a device designed to selectively convert certain part of a signal (input) pulse shape to the idler (register or output) pulse shape. The shape of the pulse to be converted can be selected by shaping the pump pulse to this exact pulse shape, for example by using a spatial light modulator (SLM) based pulse shaper [50]. By operating the device with a basis consisting of orthonormal pulse shapes, so called temporal modes or pulsed modes, any input pulse can be analyzed, as the achieved conversion efficiency is proportional with the input pulse's overlap with every mode. It has been shown that such a device can be used to implement a quantum communication framework based on temporal modes [46]. This section contains an overview over the necessary transfer function of the QPG's nonlinear process and how the necessary group-velocity relation can be achieved.

In order to implement a mode-selective conversion, the projection of the transfer function on the signal axis, the so-called marginal signal spectrum, or short "signal marginal", is required to depend only on the pump pulse shape. This is visualized in Figure 3.3, where Hermite-Gauss modes are used. In principle, any modal basis can be used with the QPG, but the Hermite-Gauss basis is advantageous when the device is combined with PDC sources, as their joint spectral amplitudes naturally decompose into these modes [21].

For a SFG process, the pump function lies at an angle of 45°, as mentioned in chapter 2.5. Early in the development of the QPG, it became clear that a thin, flat transfer function oriented at 0° [19] would allow to selectively "gate" on the pump pulse shape, hence the name Quantum Pulse Gate. In the sketched out transfer functions it can be seen, that the signal marginal is very close to the pump pulse shape, how close depends mostly on the phasematching bandwidth [51]. In terms of dispersion engineering, one can identify two requirements on the phasematching function: A phasematching angle $\alpha$ of 0°, and a narrow idler marginal bandwidth, which in this configuration is identical to the phasematching bandwidth. We recall equation 3.3 to deduce the necessary group-velocity relations:

$$0^\circ = \alpha = \arctan\left(\frac{\frac{\partial k_p}{\partial\omega} - \frac{\partial k_s}{\partial\omega}}{\frac{\partial k_p}{\partial\omega} - \frac{\partial k_i}{\partial\omega}}\right) \tag{3.4}$$

$$\Rightarrow \quad \frac{\partial k_p}{\partial\omega} - \frac{\partial k_s}{\partial\omega} = 0 \tag{3.5}$$

where $\partial k/\partial\omega$ is the inverse group-velocity or "group-slowness". Since the group slowness difference between signal and pump has to be zero, the group velocity difference, or pulse walk-off between signal and pump also has to be zero. Naturally, all materials are dispersive, meaning that the refractive index and therefore the group-velocity depends on wavelength, which makes this type of group-velocity relation impossible to achieve in most materials, The only way is to employ a birefringent material. Luckily, the two most popular nonlinear materials with waveguides, Potassium Titanyl Phosphate (KTP) and Lithium Niobate (LN) are both birefringent. In principle, one can use the birefringence to compensate for the dispersion. A wavelength combination with successful compensation is shown in Figure 3.4.

For every signal wavelength on the slow polarization, there is exactly one pump wavelength on the fast polarization, that has the exact same group velocity. For a signal central wavelength of 1550 nm, where the engineered

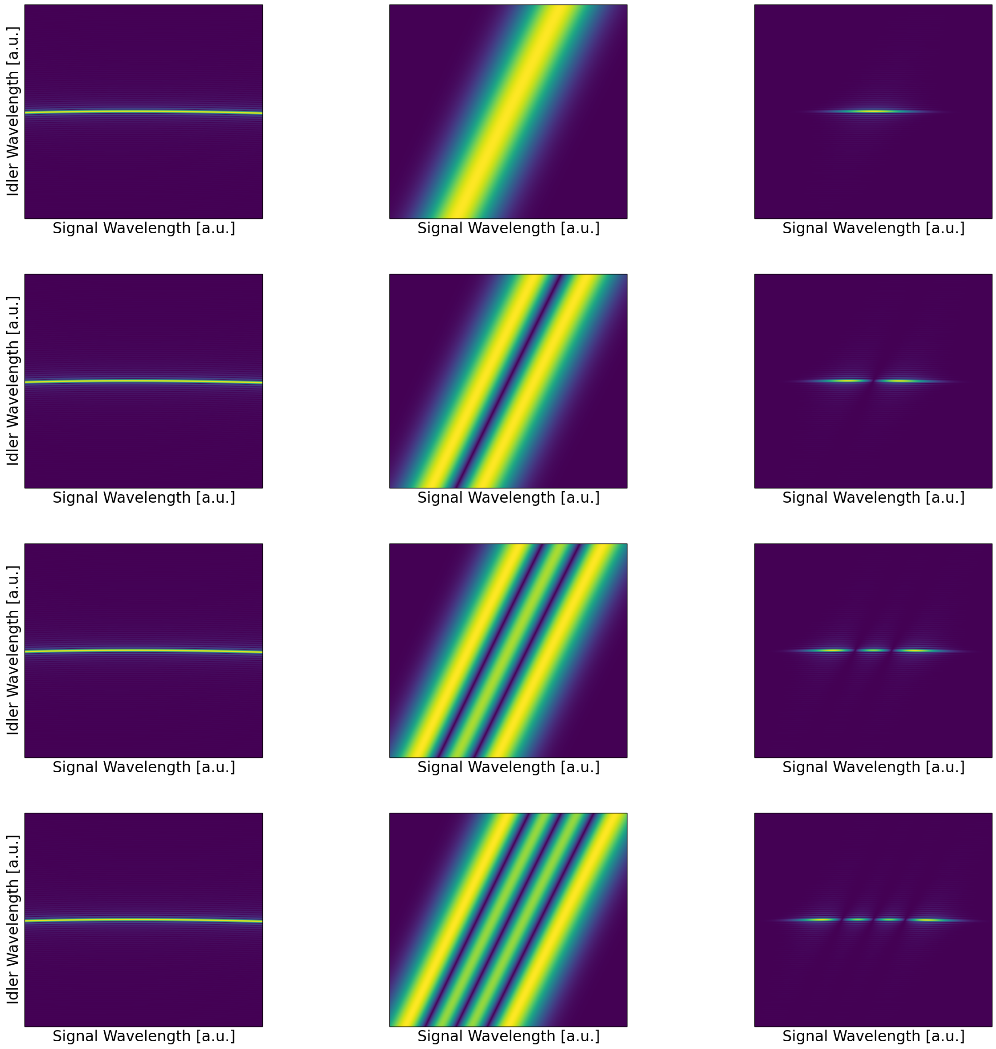

Figure 3.3.: Phasematching, pump function intensity and transfer function intensity for the first three Hermite-Gauss modes. The left column shows a numerically calculated phasematching function based on effective Sellmeier equations, the middle row shows pump intensity for different orders of Hermite-Gauss modes, and the right column shows the product of both

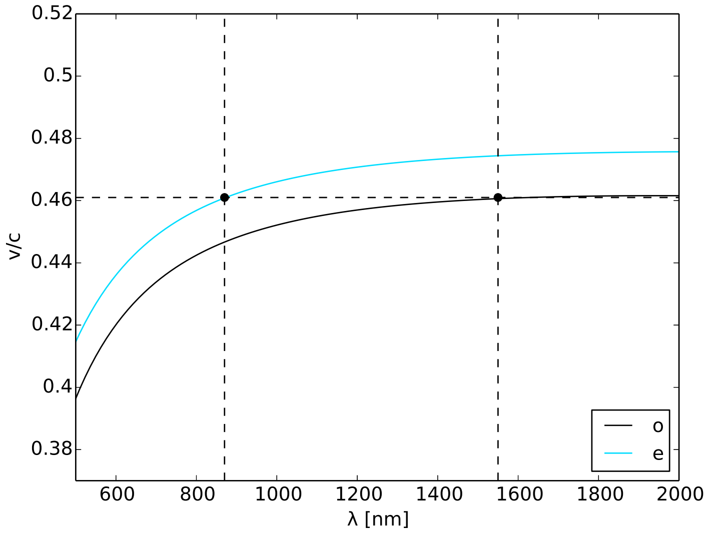

Figure 3.4.: Dispersion curves for both polarizations for Titanium-indiffused waveguides in z-cut Lithium Niobate. A Possible QPG wavelength combination with group velocity matching is marked by the black dots / dashed lines

PDC source mentioned earlier emits its photon pairs, the required pump wavelength is about 870 nm, well within the range of commercially available pulsed Ti:Sapphire laser systems. With the according walk-off of the generated idler photon, suitable phasematching bandwidths can be achieved with crystal lengths of a few centimeters. Quasi-phasematching for this wavelength combination is achieved with a poling period of 4.4 $\mu$m. The dispersion curves of other materials such as KTP and $LiTaO_3$, shown before in Figure 3.2, show that it is possible to match wavelengths that are further apart or closer together, by choosing a different material.

A first QPG was tested with coherent light by Benjamin Brecht, and basic mode selective conversion at high efficiency confirmed [20]. The device was then used to successfully perform temporal mode tomography on heralded single photons [42]. In that work, the effect on the exact modal distribution of the analyzed state was also studied in detail. The measured phasematching function [47] of one of the employed waveguides is shown in Figure 3.5. By comparing the different scales of the two axes it becomes apparent, that the phasematching is indeed flat over a signal bandwidth of 100 nm measured here: The shift in central wavelength of the idler is not more than its FWHM bandwidth.

At the same time, studies on the QPG process were performed in two other

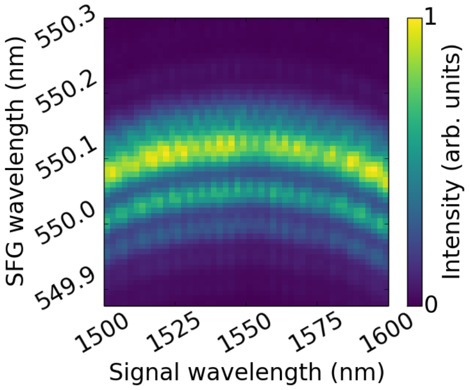

Figure 3.5.: Measured phasematching function of a QPG waveguide.

groups by others using ”quasi group-velocity matching“. They both employed an almost degenerate SFG process, where the spectral separation of signal and pump was only a few nanometers, but was not demonstrated on the single photon level [44, 45, 52]. Since all three optical fields were in the same polarization, the pump SHG would be phasematched, just like the SFG process, and the SHG wavelength would be very close to a desired single photon idler wavelength.

The QPG process has many applications. Two of those will be discussed in the following sections. Beyond these, it was shown that the QPG process can be used as an efficient means of noise filtering, that outperforms conventional spectral-temporal Fourier filtering in telecommunication [53].

## 3.3. Application: Bandwidth compression

The group-velocity-matched process developed as the QPG has more applications than just mode-selective frequency conversion, some of which shall be outlined here. The first one is spectral bandwidth compression, which refers to efficiently changing the spectral bandwidth of light, ideally lossless. Bandwidth compression plays an important roll in building hybrid quantum networks. While a quantum networks in general are still a quite undefined term, since nobody has built one yet, it is envisioned to be a network of quantum nodes [15], which may contain devices such an quantum memories, quantum repeaters, quantum computers, etc., all of which are by themselves still at a proof-of-principle stage of development. These nodes are imagined to be linked by some kind of quantum communication protocol. Early demonstrations of such a link only incorporate identical nodes [12]. Proposals and demonstrations of hybrid links, which would link nodes based on different physical systems, involve frequency conversion as an interface [54, 16]. Frequency conversion has also been widely recognized as a vital component for interfacing quantum memories and quantum light sources with fiber networks [55, 56, 57, 17]. However, adapting the central frequency of light intended for coupling into another system is not sufficient, the spectral bandwidth needs to be reduced as well. This reduction has to be carried out without significant loss of overall intensity in order to be efficient. Examples in the literature exist, but they all suffer from the one or other shortcoming: While highly efficient and tunable bandwidth compression is possible using electro-optical modulators [58], the frequency shift is limited to hundreds of gigahertz. Pulse manipulation using chirped nonlinear frequency conversion is possible [59], and large bandwidth gaps can be bridged [60, 61]. However, these demonstrations suffer from insufficient conversion efficiency to outperform a spectral filter. The conversion efficiency is inherently limited, since a broad phasematching and therefore short crystal is required. An implementation of a pulse manipulation device in a bulk diamond suffers from similar problems, and also deteriorates the photon number statistics of the converted light [62].

**Quick summary**

The idea behind the bandwidth compression experiment is to use the specific phasematching angle of the QPG to reshape the spectrum of the photons that are being converted. A flat phasematching angle and broadband pump create a transfer function that is narrow and oriented parallel to the signal axis. This means that any broadband signal spectrum is converted into a narrowband output without any additional manipulation. To show the change in spectral bandwidth, the spectrum is measured before and after conversion on the single photon level. In order to show that the spectrum is actually reshaped and not just filtered down, the efficiency of the process needs to be measured, and has to be higher than the ratio of the bandwidth after and before conversion. This is done by comparing the Klyshko efficiencies. To round everything up, the heralded second-order correlation function is measured before and after conversion, in order to show that no significant noise photons are added by the nonlinear process.

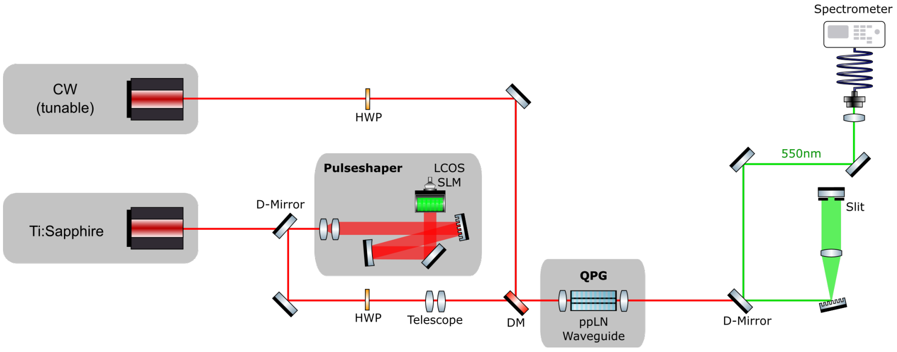

Figure 3.6.: Setup used for PDC characterization. CW: Continuous wave laser, SHG: Second harmonic generation, LCOS SLM: Liquid-crystal-on-silicon spatial light modulator, ppLN: periodically poled Lithium Niobate crystal, PDC: parametric down-conversion, DM: Dichroic mirror, SMF: Single mode fiber

### 3.3.1. Bandwidth compression in the QPG

The approach presented here is different from the previous implementations of bandwidth compression with nonlinear frequency conversion. The QPG provides the bandwidth compression intrinsically, without outside manipulation of the pump pulse or electro-optics. The reason for this lies in the special group-velocity matching between the two input fields, and the drastic group-velocity mismatch between these inputs with the output. This peculiar combination yields the phasematching function previously presented. However, here the focus lies purely in the asymmetry of this function. The transfer function can be measured using a arrangement of two lasers, one at 850 nm (Coherent Chameleon Ultra II) and a tunable continuous wave laser (Yenista Tunics SCL), and a spectrometer (Andor Shamrock 500), shown in Figure 3.6. The telecom laser is tuned, and the Ti:Sapphire oscillator is adapted to achieve maximum converted intensity. The measured spectra are stacked to produce the transfer function shown again in Figure 3.7.

Within a large window of tens of nanometers on the signal (or input) axis, the phasematching is is parallel to the signal axis and has little curvature, yielding a narrow output spectrum. The flatness is the result of the matched group-velocities of signal and pump, while the narrow output is the result of the idler group-velocity mismatch, which causes a large pulse walk-off. The shape of the phasematching alone shows, that the output bandwidth will be smaller than the input bandwidth, as long as only a sufficiently flat section of the phasematching is selected with an appropriately selected pump wavelength and bandwidth. Nevertheless, the shape of the phasematching alone raises the question, what happens with the rest of the spectrum. Is everything converted to the narrow output spectrum, or is the bandwidth first preserved and then

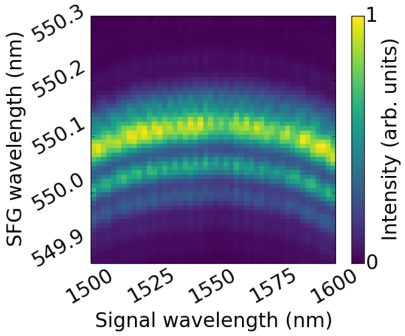

Figure 3.7.: Phasematching function of the quantum pulse gate. The spectrum of the sum-frequency generation (SFG) signal from the Ti:Sapphire laser and a tunable continuous wave telecom laser were recorded on a single-photon sensitive spectrometer.

cut, thus reducing efficiency? The experiment will show that it is the first option. In the time domain, the signal and pump have identical pulse duration. This means, that the entire pulse is converted with equal pump power, and the spectral picture, the phasematching, reveals that the entire pulse spectrum is phasematched. Therefore, there is no reason why part of the pulse wouldn't be. The angle of the phasematching, or rather the lack thereof, merely dictates the correlation between pump and signal frequency, only selecting the "good" ones that result in bandwidth compression. The crux of showing proof for bandwidth compression versus spectral filtering is that loss in the system has to be measured. While filtering a spectrum might provide the same output spectrum, the tails of the spectrum will be cut, resulting in loss, while bandwidth compression - in principle - is lossless, and the spectrum is rather reshaped than cut. Therefore, in order to provide proof of bandwidth compression, the overall system efficiency needs to be greater than the ratio of the measured bandwidths.

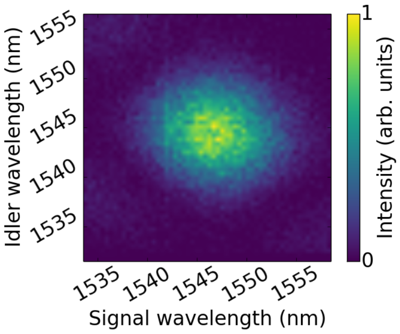

Figure 3.8.: Joint spectral intensity of the photon pairs generated in the parametric down-conversion source. The spectral were measured using two dispersive fiber time-of-flight spectrometers

### 3.3.2. The experimental apparatus

**The PDC source** The source used in the experimental demonstration is mostly identical with the experiments previously performed on the QPG and identical with the one developed in [2]. The source uses so-called ”symmetric group-velocity matching“, which means that the group velocity of the pump field is almost in the middle of the two others. This brings the phasematching angle to 45 degrees, perpendicular to the pump, allowing for the generation of spectrally decorrelated photon pairs. The crystal with a poled length of 6 mm employed here provides the decorrelated JSI shown in Figure 3.8. The 772.5 nm PDC pump beam is generated using the output from a Ti:Sapphire oscillator (Coherent Chameleon Ultra II), which in turn pumps a optical parametric oscillator (APE compact OPO). The OPO output at 1545 nm is frequency doubled using a periodically poled bulk Lithium Niobate crystal. A 4f-pulse shaper with a spatial light modulator (Hamamatsu LCOS-SLM) is used to narrow the spectral bandwidth in order to produce a decorrelated PDC state. The setup used to measure the properties of this state is depicted in Figure 3.9. The PDC photons are separated from the pump light using a bandpass filter. Since a type-II PDC process is used where signal and idler possess orthogonal polarization, a polarization beam splitter can be used to split the two photons of each pair. They are then coupled into single mode optical fibers connected to superconducting nanowire detectors. These two detections can be used to measure the Klyshko efficiency of the source [63]. This number, defined for the signal ($s$) and idler ($i$) arm, respectively, as the ratio between coincidence counts and the counts in one arm:

$$\eta_\mathrm{c} = P_\mathrm{cc}/P_\mathrm{s,i} \tag{3.6}$$

described how efficiently the source produces pairs and how well they are

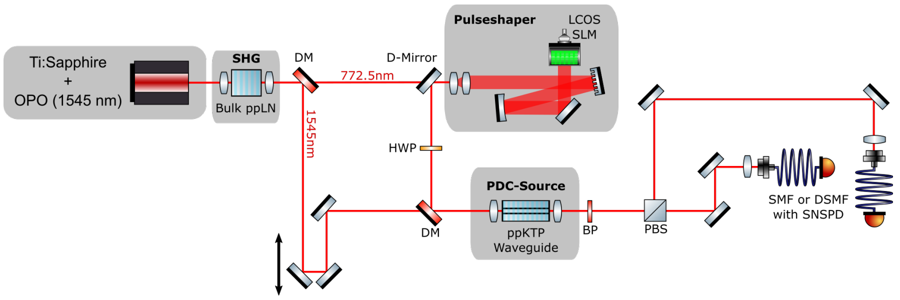

Figure 3.9.: Setup used for PDC characterization. SHG: Second harmonic generation, LCOS SLM: Liquid-crystal-on-silicon spatial light modulator, ppKTP: periodically poled potassium titanyl phosphate crystal, PDC: parametric down-conversion, BP: Band pass filter, DM: Dichroic mirror, PBS: Polarization beam splitter, SMF: Single mode fiber, SNSPD: Superconducting nanowire single photon detector

detected. This number already incorporates linear losses as well as detection losses, and can be seen as a overall system pair production efficiency. The depicted setup is used to measure the efficiency before the following frequency conversion in the QPG. The Klyshko efficiency amounts to 20.2 %, given the following raw count rates:

| | |
|---:|:---|
| herald counts ($s^{-1}$) | 430,000 |
| coincidence counts ($s^{-1}$) | 86,000 |
| Klyshko efficiency | 20.2 % |

Alternatively, dispersive single mode fibers can be connected in front of the nanowires, which facilitates a time-of-flight spectrometer [64]. This was used to measure the PDC state's joint spectral intensity shown in 3.8. With the group delay of the fibers (431 ps $nm^{-1}$) and timing jitter of the photon counting system (150 ps) known, the relative timing allows to measure relative spectra (the central wavelength has to be calibrated using a known source), with a spectral resolution of 0.35 nm. The photon pairs are generated at a central wavelength of 1545 nm and a bandwidth of $963 \pm 11$ GHz. The error of the spectral bandwidth is the error of the Gaussian fit.

For the further experimental steps the PDC signal photon is coupled into a single-mode fiber and used as a herald. The idler photon is coupled to the QPG.

**Nonlinear bandwidth compression** The QPG pump with a central wavelength of 854 nm is directly generated using the Ti:Sapphire laser, and spectrally narrowed using a second 4f-line which includes a spatial light modulator (Hamamatsu LCOS-SLM), allowing for reconfigurable filtering. In this experiment, the QPG itself consists of a 27 mm long Lithium Niobate crystal with periodi-

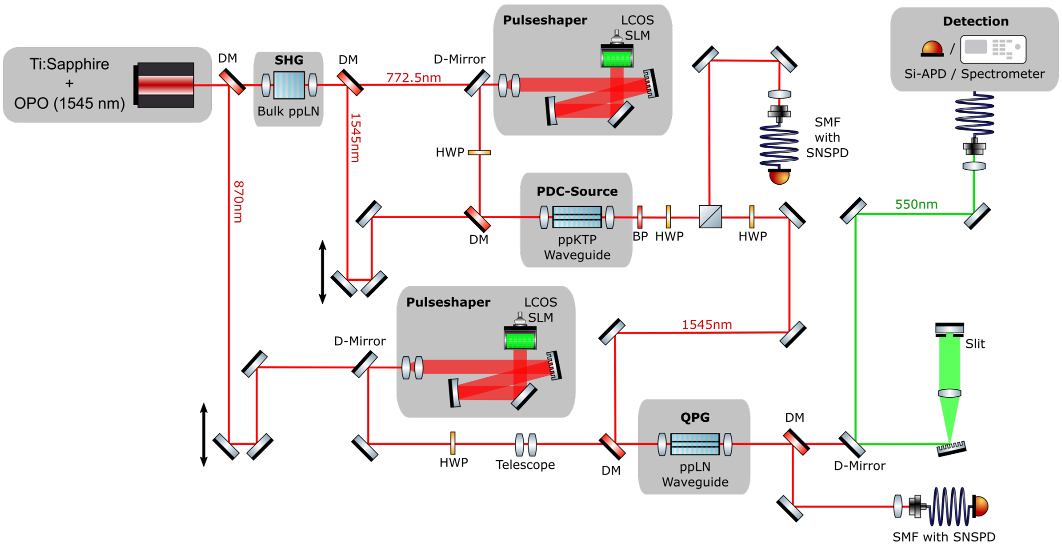

Figure 3.10.: Setup used for characterization of the QPG's transfer function as well as the measurement of conversion efficiency, correlation functions and spectra. Ti:Sa: Ti:Sapphire laser, OPO: Optical parametric oscillator, CW: Continuous wave laser, SHG: Second harmonic generation, LCOS SLM: Liquid-crystal-on-silicon spatial light modulator, ppKTP: periodically poled Potassium Titanyl Phosphate crystal, ppLN: periodically poled Lithium Niobate Crystal, PDC: parametric down-conversion, QPG: Quantum pulse gate, BP: Band pass filter, PBS: Polarizing beam splitter, DM: Dichroic mirror, SMF: Single mode fiber, MMF: Multi mode fiber, SNSPD: Superconducting nanowire single photon detector, SiAPD: Silicon avalanche photo diode

cally poled, Titanium-indiffused waveguides. The poling period is 4.4 $\mu$m. The generated light at 550 nm is separated from the other wavelength with spectral filters and coupled into a single-mode optical fiber, same as for the actual QPG experiments. The fiber can then be connected to either a silicon APD or a single-photon sensitive spectrometer. A schematic of the whole setup is shown in Figure 3.10.

To verify bandwidth compression, several things have to be measured. First, the spectra of the PDC photons before and after conversion have to be measured. The PDC spectrum was extracted from the JSI displayed in Figure 3.7, which was measured by Vahid Ansari using dispersive fiber time-of-flight spectrometers with a resolution of 0.35 nm [64], as described previously. The spectrum of the converted light was measured using a single-photon sensitive motorized Czerny-Turner spectrometer (Andor Shamrock 500 with single-photon sensitive Andor emCCD detector) with a resolution of 40 pm. Both spectra are

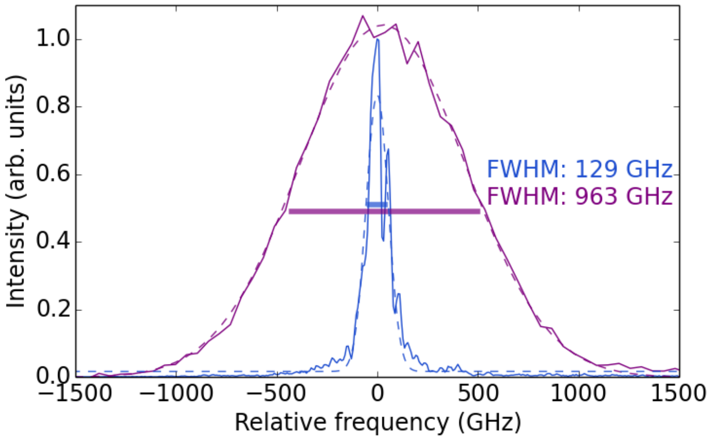

Figure 3.11.: Marginal spectra of the parametric down-conversion idler photon before (magenta) and after (blue) frequency conversion in the quantum pulse gate centered around their respective center frequencies. Dashed lines correspond to Gaussian fits from which the bandwidths were obtained. The spectrum of the idler photons were measured using a dispersive-fiber time-of-flight spectrometer. A Czerny-Turner spectrograph was used for the spectrum of the converted light.

shown in Figure 3.11. Both spectra are essentially raw data, no smoothing, filtering or background subtraction has been applied.

From the Gaussian fits to the measured spectra, the amount of bandwidth compression, which is the ratio between input and output bandwidth, is visible. The output bandwidth is 129±4 GHz, which gives a bandwidth compression ratio of 7.47±0.01. Again, the given accuracy stems from the uncertainty of the Gaussian fit. Objectively, a Gaussian function is a bad fit for the observed converted spectrum, since it resembles more of a one-sided sinc-function. However, this experiment was designed to specifically not care for experimental imperfections. While a tighter fit could be obtained using a sinc-shaped fit, or only fitting to the main peak, a Gaussian fit best described the ”overall“ bandwidth, including large sidelobes like the one observed here, and is therefore the best choice to ”blindly“ describe the bandwidth.

### 3.3.3. Efficiency and noise properties

However, at this point, it is impossible to differentiate between spectral bandwidth compression and filtering. To prove that the spectrum has not just been filtered, a measurement of the conversion efficiency is necessary. The internal conversion efficiency is measured via the depletion of Klyshko efficiency of the converted photon. It is measured in transmission through the QPG:

$$\eta_{\mathrm{t}} = P_{\mathrm{cc}}/P_{\mathrm{h}} \tag{3.7}$$

where $P_{\mathrm{cc}}$ is the coincidence-rate between the herald and transmitted PDC photon, $P_{\mathrm{h}}$ is the herald count rate. This is then measured with the QPG pump open and blocked. From these two measurements, the internal conversion efficiency is deduced:

$$\eta_{\mathrm{int}} = 1 - \frac{\eta_{\mathrm{t}}^{\mathrm{open}}}{\eta_{\mathrm{t}}^{\mathrm{blocked}}} \tag{3.8}$$

This is a direct measure of the internal conversion efficiency, which automatically excludes all losses. The only assumption is that there are no pump-induced losses. From the author's experience, there are no significant effects of this kind. The internal efficiency was measured as a function of QPG pump power, the result is shown in Figure 3.12.

The data was fitted with the expected $\sin^2$-dependence on power. The fit allows to see, whether the theoretical maximum efficiency was reached. Since the curve has not yet reached the turning point at the last data point, which corresponds to a pulse energy of 1.45 nJ, a higher conversion efficiency would be possible with the expense of even higher pump pulse energy. To verify whether this conversion efficiency is sufficient to beat spectral filtering, the external (overall system) efficiency is also measured by comparing Klyshko efficiency of the unconverted PDC idler photon right after generation $\eta_{\mathrm{i}}$, and the converted, 550 nm photon, $\eta_{\mathrm{c}}$:

$$\eta_{\mathrm{ext}} = \frac{\eta_{\mathrm{c}} \cdot \eta_{\mathrm{SNSPD}}}{\eta_{\mathrm{i}} \cdot \eta_{\mathrm{SiAPD}}} \tag{3.9}$$

where the efficiencies were scaled by the detector efficiencies for both arms $\eta_{\mathrm{SNSPD}} = 0.9$ and $\eta_{\mathrm{SiAPD}} = 0.6$. The idler before the QPG was detected using a single-photon superconducting nanowire detectors (SNSPD), the converted photon with a silicon avalanche photo diode (SiAPD). The Klyshko efficiency before the QPG was 20.2 %. After the QPG, the Klyshko efficiency was 2.27 %, ascertained from the following raw count rates:

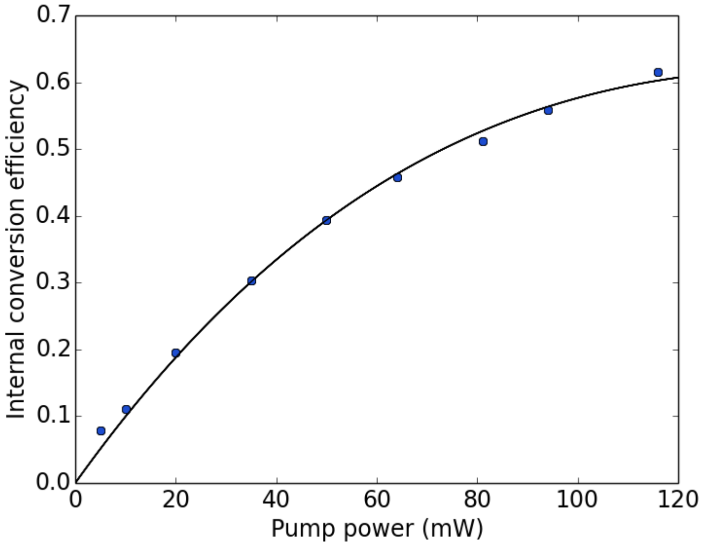

Figure 3.12.: Pump power dependence of the quantum pulse gate's internal conversion efficiency. The solid line was fitted to the data and follows $0.619 \cdot \sin^2(0.130 \cdot \sqrt{P})$. Each data point was obtained by measuring the depletion of the unconverted (transmitted) beam's count rate. Poissonian distributed statistical uncertainties of the count rates are small, error bars are therefore omitted as they are smaller than the data points

| | |
|---|---|
| herald counts (s$^{-1}$) | 465,000 |
| coincidence counts (s$^{-1}$) 0 | 10,600 |
| Klyshko efficiency | 2.27 % |

These numbers, both before and after the QPG conversion, have been obtained obtained by "fair means", meaning that they contain no corrections for experimental imperfections. The two measurement points before and after conversion contain all linear losses such as fiber and waveguide coupling losses and linear loss and reflections on optical components. In additions, the count rates were not corrected for dark counts and not time filtered, they are truly raw unaltered detector counts.

The external conversion efficiency is therefore 16.9 %. For comparison: the transmission through an ideal (lossless) bandpass filter with equal bandwidth would be 13.40±0.02 %. The error corresponds to the uncertainties of the Gaussian fits applied to the measured spectra. Therefore, the system indeed outperforms spectral filtering. The discrepancy between the internal and external conversion efficiency has several reasons: The spatial mode mismatch between the PDC source's waveguide and the QPG's waveguide limit coupling efficiency. In addition, there are reflections on optical components such as lenses, and limited bandpass transmission through the filters used to separate the converted from the unconverted and pump light.

Last but not least it has to be verified whether the frequency conversion process adds any noise photons. This can be verified by measuring the heralded second-order correlation function with a Hanbury Brown - Twiss configuration [65]:

$$g^{(2)} = \frac{P_{cc}}{P_1 \cdot P_2} \tag{3.10}$$

where $P_{\mathrm{cc}}$ is the coincidence rate, $P_1$ and $P_2$ are the single-click rates, all of which are conditioned on herald clicks. This kind of correlation function probes the single-photon character or photon number statistics of the state and is smaller than one for single photons, heralded or not. In this experiment, it was measured before and after conversion, and took the same value of 0.32±0.01, remaining unchanged by the conversion. The number was obtained using the following count rates:

| | before QPG | after QPG |
|---|---|---|
| herald counts (s$^{-1}$) | 910,000 | 970,000 |
| coincidences herald-mode1 (s$^{-1}$) | 6900 | 3900 |
| coincidences herald-mode2 (s$^{-1}$) | 7200 | 2780 |
| triple coincidences (s$^{-1}$) | 18.0 | 3.42 |

Therefore, since the conversion process does not only result in a bandwidth reduction, but is also sufficiently efficient even when the results are not renormalized for experimental imperfections, it can be concluded that the process performs actual bandwidth compression and outperforms a spectral filter. As no noise photons are added, the process preserves quantum photon number statistics. The bandwidth compression achieved here scales in principle with the length of the waveguide, however, producing very homogeneous, long waveguides has proven challenging and is a matter of ongoing research efforts.

### 3.3.4. Outlook: Tunability

One aspect of the QPG process has been neglected up to now: It has very limited tunability. The dispersion properties of Lithium Niobate, together with its birefringence, dictate the wavelength combinations that are possible. Ideally, one would like to build an interface, that converts between the telecom C-band (1530-1565 nm) and the emission or absorption wavelength of a quantum memory or source of quantum light. This also dictates a set of wavelength, which, in general, do not have the necessary group-velocity matching. Some limited tunability is possible, as the birefringence of Lithium Niobate is temperature dependent [66, 67]. With reasonable temperatures between 20 °C and 300 °C the group-velocity matching and thus the associated output wavelength could be tuned from 540 nm to 574 nm. Higher temperatures are in principle possible to some extent, but may ultimately alter the waveguide structure through accelerated diffusion effects. The wavelength combination used for this proof-of-principle experiment was simply chosen, because the temperature of 190 °C is high enough to reduce photorefraction by a large amount [68], but low enough to allow for simple heating without mayor insulation.

An application of interest for such a process would be to couple quantum light efficiently into a quantum memory, many of which have very narrow acceptance bandwidths. The memories with the largest reported bandwidths are so-called Raman-memories, that use an off-resonant, stimulated Raman passage to store light via two-photon absorption, and retrieve them through stimulated emission. Poem *et al.* [14] suggested that transitions of the charge-neutral nitrogen vacancy center (NV0) in diamond could be used to build a more broadband memory, with bandwidths of the order of a few GHz, certainly within reach with the device presented here. At least the efficient bandwidth reduction can increase the coupling to such a Raman-memory, even if not to 100 %. Figure 3.13 shows the relative group-velocity mismatch between the input and pump field for the process used here. The data for two temperatures, 190 °C and 300 °C have been plotted on top of each other, the left white stripe with perfect velocity matching corresponds to 190 °C, the right one to 300 °C. The solid white lines follow wavelength combinations, that yield output wavelengths of 550 nm for the left one, and 574 nm for the right one. Only the white line and the white area of the color map cross, can a certain wavelength combination be perfectly group-velocity matched. Two things can be observed.

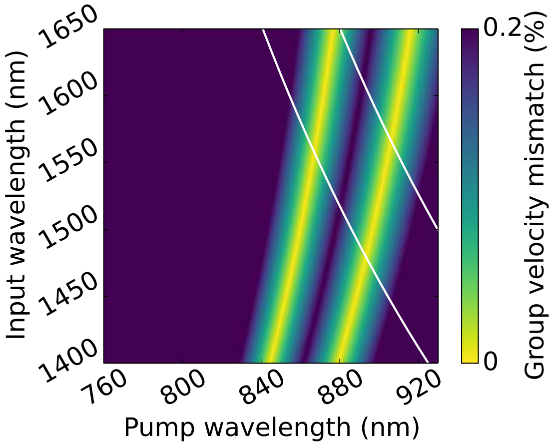

Figure 3.13.: Group velocity matching in Ti:LiNbO$_3$ between waveguide modes in ordinary and extraordinary polarization at two different temperatures (left stripe: 190° C, right stripe: 300° C). The solid white lines indicate wavelength combinations where the sum-frequency generation process reaches the desired wavelength of 574 nm (right line) for the transition of the charge neutral nitrogen vacancy center or the wavelength of 550 nm (left line) chosen in this article.

First, to keep the input wavelengths of roughly 1550 nm, but tune to another output wavelength, the temperature has to be changed. Second, changing the temperature also allows to keep the output wavelength constant, but with different inputs. Note that another parameter that has to be adapted whenever one wishes to use different wavelengths is the poling. Therefore, the process is not tunable in the sense that the wavelength combination can be changed on the fly for one waveguide, but merely that it is possible to produce a waveguide for the desired combination.

If a wavelength combination beyond this tuning range needs interfacing, the only option is to move to a different material, that offers an entirely different birefringence and dispersive properties. Other nonlinear materials that offer the possibility of waveguides are Potassium Titanyl Phosphate (KTP) and Lithium Tantalate (LiTaO$_3$). Both are in principle available commercially, although not as widely as the more popular Lithium Niobate and at the same quality. The group-velocities of all three materials, previously shown in chapter 3.1, are once again displayed in Figure 3.14. KTP has a higher birefringence than LiNbO$_3$ [69], and allows to match the velocities of wavelengths that are further apart. Therefore, one could build a QPG with the same input wavelength in the telecom C-band, but an output in the blue or UV. LiTaO$_3$ on the other hand is less birefringent [70], and therefore allows to match wavelengths that are closer, and bridge a smaller spectral range, in order to reach output

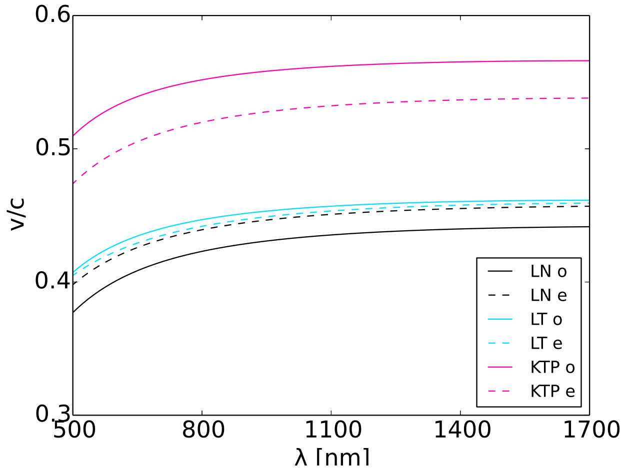

Figure 3.14.: Group velocityies of $LiNbO_3$, KTP and $LiTaO_3$.

wavelengths in the red or infrared range.

One example is shown in Figure 3.15. The target wavelength 738 nm could address a memory based on a silicon vacancy center in diamond. These memories have first been proposed a few years ago [71] and have seen growing interest since then [72, 73, 74]

At the expense of pump suppression, quasi group velocity matching is possible by employing a almost degenerate SFG, where the pump and input central wavelength are only separated by a few nanometers [52, 44] and thus have very little walk-off. Applications of this kind of group-velocity matching on the single photon level have so far not been demonstrated.

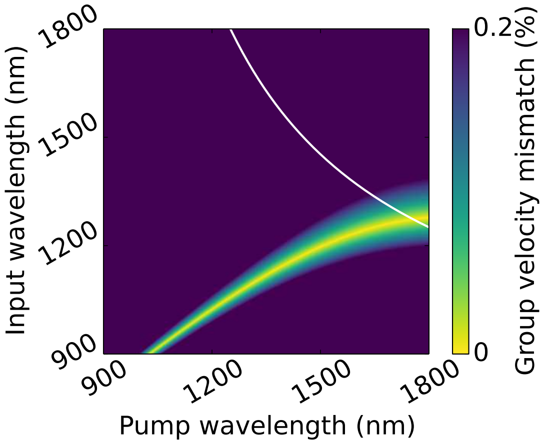

Figure 3.15.: Group velocity mismatch in bulk $LiTaO_3$ the ordinary and extraordinary polarization at 190°C. Here, the white line indicates an output wavelength of 738 nm, corresponding to the silicon vacancy transition in diamond.

**Alignment procedure**

Alignment for this experiment is straight forward. Since all detectors are fiber coupled, no additional alignment is necessary for measuring each quantity presented here.

First, the PDC source is aligned. To do this, the pump beam is coupled through the waveguide by centering the beam on the lens, moving the waveguide in position, adjusting focus, and beam walking for maximum throughput. This is not critical, since there is more than sufficient to compensate for bad pump coupling. Using a 4f-line (with a slit or SLM), the pump bandwidth is set to roughly the phasematching bandwidth. Using a throughcoupled 1550 nm alignment beam, the fiber couplings are aligned by beamwalking the input mirrors, lens position and focus. If there is trouble finding the fiber core, it is helpful to first optimize coupling into a multimode fiber, which is much easier and helps to center the focus on the fiber. After this is finished, the fibers can be connected to the TOF spectrometer fibers, and/or single photon counters. These will be used to measure the JSI and Klyshko efficiency to verify good coupling and proper pump bandwidth.

Second, the QPG is aligned. First, the 1550 nm alignment beam is coupled through and to prealign the waveguide and fiber couplings the same way as for the PDC source. The coupling is then optimized using the single photon beam and a photon counter. The focus of the incoupling to the waveguide then remains fixed. The pump beam is only coupled using the incoupling mirrors, a optional telescope can be used to compensate for the focus mismatch at the incoupling.

The easiest way to find the delay between the PDC and pump pulse at the QPG is to strongly attenuate the pump beam using a ND6 filter and observing both pulses simultaneously on the arrival time histogram of the photon counter. This allows to set the pump delay with a precision of roughly 100 ps. The fine adjustment is done using the single photon sensitive spectrometer as a detector for the converted light. If the converted light cannot be found, the 1550 nm alignment beam has to be used instead. Looking for seeded PDC helps to align the alignment beam and PDC delay.

Once the converted PDC can be observed, optimize the coupling of the pump to the correct spatial mode, by aligning on the strongest peak in the green spectrum. Then, use a 4f line to block out the others. Finally, change the center wavelength, spectral bandwidth and spectral phase of the pump using the SLM pulse shaper in order to optimize for maximum coincidences between PDC idler and converted green light.

For photon counting experiments, all data was recorded until the size of the raw data reached about 2 GB, which corresponds to roughly 250 Billion timetags, including laser trigger timetags, which is usually to allow for negligible statistic errors.

## 3.4. Application: nonlinear cross correlation measurements

A second application of the so-called Quantum Pulse Gate nonlinear process is nonlinear cross-correlation. It harnesses the mode-selective nature of the frequency conversion as a means of measuring the temporal intensity envelope of single photons. The key for this is that the mode-selectivity works for any arbitrary basis. A particularly simple one is the time bin basis. It can be employed by using pump pulses of very short pulse duration and variable delay, in contrast to the Hermite-Gauss basis used before. Every delay then corresponds to a different time-bin. By measuring the click-rate for every time bin, a temporal intensity profile can be constructed.

The research and Figures 3.17 through 3.20 were previously published in [48].

In general, complete pulse characterization of single photons, including both spectral intensity and phase, directly or through combined measurements in time and spectrum, is challenging and rarely demonstrated. The most popular classical pulse characterization techniques, optical auto-correlation [75] and frequency resolved optical gating (FROG, [76]) in all its variations, use the correlation times between two photons from a pulse to reconstruct a pulse profile, and are thus fundamentally impossible to apply to single photons. A work-around would be a cross-FROG [77], which essentially replaces one of the photons with a known reference pulse. However, this measurement is highly non-trivial to set up and to the best of my knowledge has never been demonstrated on the single photon level. Another powerful technique, spectral phase interferometry for direct electric-field reconstruction, has only recently been demonstrated on the single photon level, thanks to advances in fast electro-optic modulators that replaced chirped-pulse-pumped upconversion as a means of spectral shearing. Streak-cameras work on single photons in principle, but only for very advantageous configurations [78, 79]. However, for many measurement scenarios, knowledge of the full spectral-temporal pulse shape is not required, it is often sufficient to only measure the time-bandwidth product, for which spectral and temporal intensity measurements are needed, but not the phase. One of those applications will be discussed here: Assessment of the spectral purity of single photons. Spectrally pure single photons are a key asset in quantum optics. The most important common way of measuring the purity is through the joint spectral intensity and doing a modal decomposition. If the state is single-mode, it is also pure [80]. However, the JSI is blind to any quadratic or higher-order spectral phases, which increases the time-bandwidth product, and decreases purity [81]. The technique summarized here is not entirely new and has been demonstrated before [37], but is performed in a more efficient manner, which allows for a much shorter measurement duration.

In the following the experimental apparatus is explained, and the method is applied to single photons from a PDC source in order to establish bounds of their spectral purity.

**Quick summary**

If the group velocity of signal and pump are matched, the overlap between the two pulses stays constant when they travel through the crystal. Since the conversion efficiency is proportional to the overlap, this constant overlap can be used to sample the signal pulse by using a short pump pulse. The temporal intensity profile of the signal pulse can then be recovered as a function of the delay between signal and pump pulse. The delay is in this implementation set by rotating a thick glass plate, where the optical path depends on the rotation angle. Trigger signals for the laser and the glass plate's rotation are recorded to facilitate synchronization and recovery of the delay. Because of the large conversion efficiency of the QPG process and the fast moving delay system, the measurement is much quicker than other similar examples in the literature.

### 3.4.1. Experimental apparatus

The method used here uses the mode-selectivity to measure the relative content in time bins, defined by the pump pulse temporal profile. In other words, the measured (single photon) pulse is sampled. The temporal intensity profile is then reconstructed from the click rate of the converted light as a function of delay between input and pump pulse. This is exactly what was done in [37] and applied by others [82]. Here, the technique was paired with the same highly efficient nonlinear waveguide used as a Quantum Pulse Gate and for the bandwidth compression demonstration [47]. The much higher conversion efficiency allows to reduce the measurement time significantly. While the authors of [37] report a measurement time of roughly 24 minutes, the process used here allowed to sample the same interval 30 times faster. In addition, the measurement was simplified by using a spinning glass plate as a delay device instead of manual delay stages, to adjust the delay between input and pump pulse. Such a delay device is found in many optical auto-correlators [83] and has also been demonstrated in other sampling measurements such as Terahertz imaging [84, 85].

The first main building stone is the nonlinear process used to facilitate the sampling. The setup with this nonlinear Lithium Niobate waveguide, the same

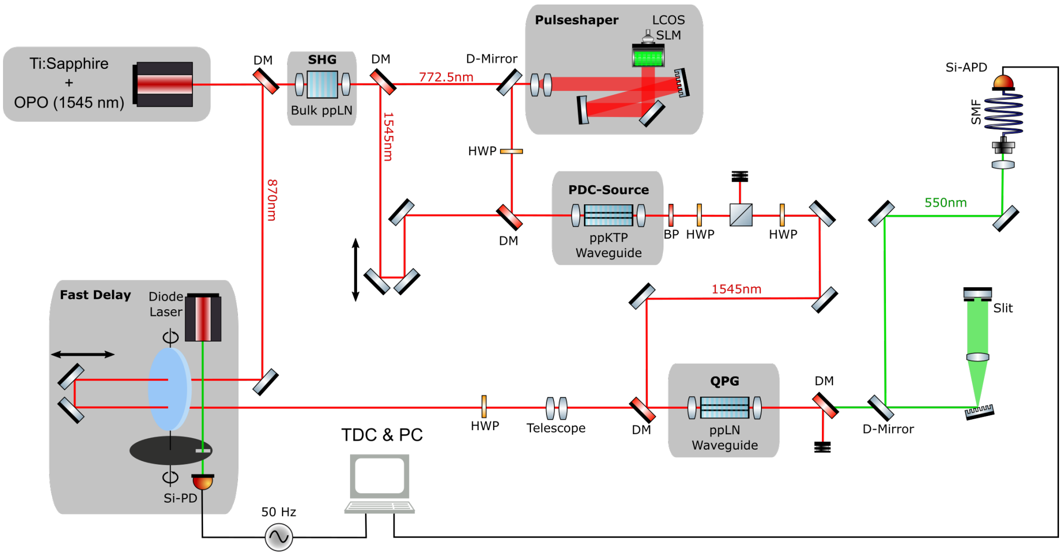

Figure 3.16.: Setup used in the sampling experiment.OPO: Optical parametric oscillator, SHG: Second harmonic generation, LCOS SLM: Liquid-crystal-on-silicon spatial light modulator, BP: Band pass filter, PBS: Polarizing beam splitter, DM: Dichroic mirror, SMF: Single mode fiber, SiAPD: Silicon avalanche photodiode, TDC: Time-to-digital converter

as used in [47], resembles much the one for the bandwidth compression measurement and is shown in Figure 3.16. The PDC source could in principle be replaced by any light source with pulsed emission in the telecom band. In addition to the previously used setup, the fast delay device has been added, which also provides a trigger signal, which heralds a complete sampling run. This signal is recorded together and correlated with the signal from a silicon APD used to detect the converted 550 nm light.

The fast delay device, shown in Figure 3.17, consists of a 12 mm-thick, 50 mm diameter plate of glass mounted onto a 3D-printed frame. The frame is rotating at 3000 revolutions per minute, driven by a DC motor. The frequency was chosen because the frame and support seemed not to vibrate as much at this frequency. The frame also holds a chopper wheel, which lets through a 532 nm laser beam once every rotation. The beam is detected on a silicon photodiode to generate a signal that heralds one full revolution. As shown in Figure 3.17, the pump laser beam traverses the plate twice, and perpendicular to the rotation axis. Therefore, there is no beam wandering as the glass plate turns. The optical path through the plate is given by Snellius' law:

$$d_{\mathrm{o}}(\alpha) = \frac{d}{\cos\left(\arcsin\frac{\sin\alpha}{n}\right)} \tag{3.11}$$

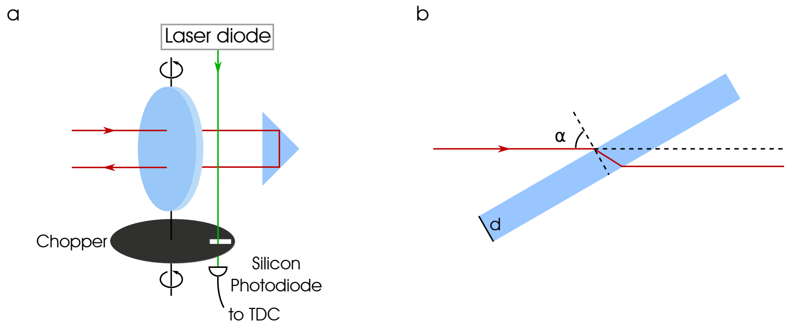

Figure 3.17.: (a) Schematic of the fast delay employed in the experiment. The laser beam is transmitted through a spinning glass plate, making use of the angle dependent optical path. Traversing the plate twice and perpendicular to the rotation axis eliminates beam wandering. The beam from a laser diode, coupled through a chopper wheel and onto a silicon avalanche diode, provides a trigger signal for each full rotation. (b) Optical path through the fast delay device

where $\alpha$ is the incidence angle of the beam on the plate and $n = 1.45$ is the silica glass plate's refractive index. The maximum optical path depends on the maximum angle, at which the the beam is not cut off by the frame's aperture. The maximum delay is

$$\Delta\tau_{\mathrm{max}} = 2 \cdot \frac{d_{\mathrm{o}}(\alpha_{\mathrm{C}}) - d}{c_0} \quad . \tag{3.12}$$

The polarization if set to be parallel to the glass plate, and with the aid of a second manual delay stage the pulse delay is adjusted so that the input waveform is sampled exactly when the plate is at the Brewster angle. This ensures maximum transmission through the plate and thus available pump power. The plate increases and decreases the optical path twice per rotation, hence the waveform is sampled 4 times per rotation and 200 times every second. If the maximum delay of 12.8 ps, sampling frequency of 200 Hz and laser repetition frequency of 80.165 MHz are known, it is straight forward to calculate that the waveform is sampled with roughly 1000 points, resulting is a sample distance of 12.8 fs. This is the delay introduced from shot to shot. Since it is smaller than the minimal pump laser pulse duration of 150 fs, the measured waveform is sufficiently sampled. Fluctuation of the rotation frequency can be a source of error, since it changes the rotation period and therefore the sample distance and number of samples. To evaluate this effect, the rotation speed was tracked, and from the maximum slope of the curve a uncertainty of 70 fs for the resolution was estimated. In addition, the dispersion of the glass plate stretches the pump pulse by another 4 to 5.5 fs, depending on the angle. Still, the initial pump pulse duration is the limiting source of error. To verify this, a known reference, generated by the laser system's OPO, was measured. From optical autocorrelation the pulse length was known to be 350 fs. From the measurement, an actual measurement accuracy of 300 fs could be ascertained. The source of the additional error could not be identified clearly, but may stem from vibration of the glass plate's mount, which may in principle cause additional delays which are synchronized to the rotation frequency.

When the delay trigger signal and the converted light clicks are recorded, the single photon temporal intensity envelope can be recovered using the relative arrival time of the photon and the delay trigger signal.

**Alignment procedure**

The alignment of this experiment is most similar to the one for bandwidth compression presented in section 3.3. This is true for the alignment and initial characterization of the PDC source, QPG and fiber couplings. There is no pulse shaper in the QPG pump beam path. Additional care has to be taken when the fast delay is added to the setup.
Start by adding a back-and-forth style delay line with a retroreflector (90-degree double mirror holder or 90-degree prism retroreflector). The delay device is designed for 125 mm beam height, same as the rest of the QPG pump beam path. Make sure that the beams are parallel and have this constant beam height. Otherwise, there would be beam wandering observed when the delay plate is spinning.
Insert the delay plate at a 90 degree angle towards the two beams. Due to the parallel double pass geometry any beam displacement by the glass plate is reversed on the return path. However, this misplacement should anyway be minimal if the beams were aligned correctly before inserting the delay. Continue with aligning the delays between the PDC and QPG pump pulses.

### 3.4.2. Demonstration of purity measurements for single photons

The spectral purity of single photons is an important figure for their application [34]. Measuring it is possible through interference with a reference pulse [86]. However, the purity is in many cases only estimated using the JSI, which is only possible when the are no quadratic or higher order spectral phases, which implies the photons are Fourier-limited or, in other words, are at their minimum time-bandwidth product (TBP) [87, 81]. Unfortunately, the JSI overestimates the purity if such phase contributions exist. While the TBP of one photon from a PDC state alone is not suitable to directly measure the purity, it will still show directly *whether* the photon is pure or not. To estimate a lower bound of the purity, modeling of the source is necessary.

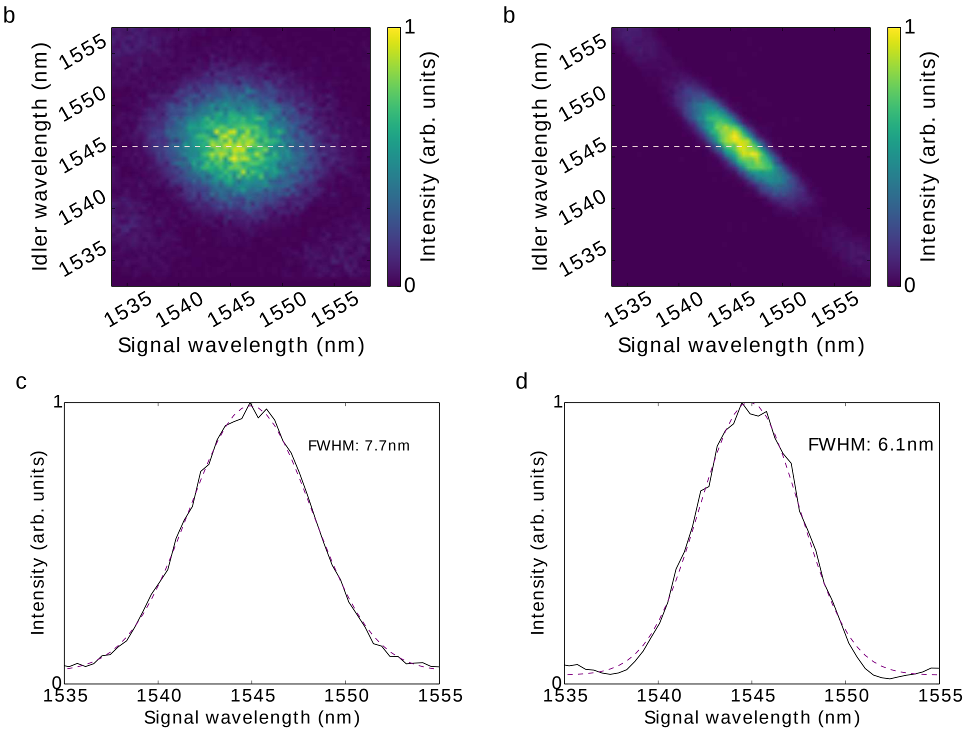

Figure 3.18.: (a) and (b): Joint spectral intensities of the decorrelated and correlated PDC state measured with a pair of dispersive fiber time-of-flight spectrometers. The dashed lines indicate where the cuts for the calculation of the expected temporal envelopes were taken. (c) and (d): Respective marginal spectral of the signal photons, obtained by integrating the respective JSIs over all idler wavelengths.

The source measured here was the same decorrelated PDC source used in previous experiments [2]. By changing the PDC pump bandwidth using the 4f-line shown in Figure 3.16, two different PDC stated were produced: One with decorrelated joint spectral intensity, and an anti-correlated one. The JSIs were measured by Vahid Ansari using a pair of dispersive fiber time-of-flight spectrometers [64]. The results, including cuts along the signal-axis, are shown in Figure 3.18. The marginal signal spectra were fitted with Gaussians (red dashed lines in Figures 3.18c and d) to obtain the spectral FWHMs. These bandwidths are $\Delta\lambda$=7.7 nm±0.1 nm or $\Delta\nu$=966 GHz for the decorrelated PDC state and $\Delta\lambda$=6.1±0.1 nm or $\Delta\nu$=766 GHz for the correlated state.

The temporal intensity profiles were measured with the setup presented here. Each profile was obtained with a measurement duration of 150 s. The recorded converted detector clicks were analyzed in terms of arrival time relative to the

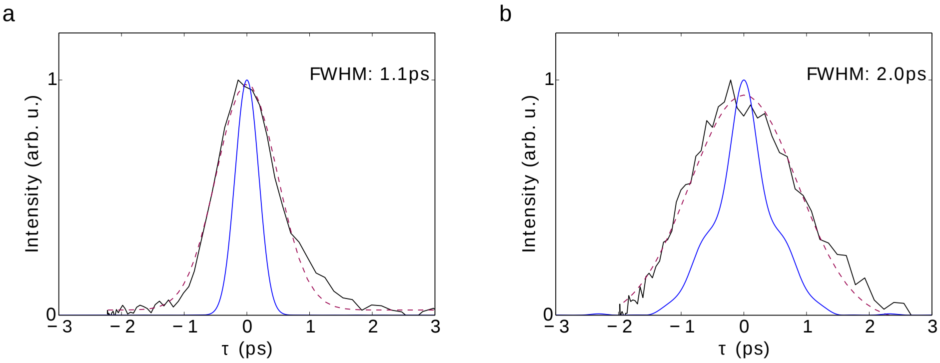

Figure 3.19.: Temporal envelopes for decorrelated (a) and correlated (b) state extracted from the sampling measurement. Solid lines black are data, the dashed lines correspond to Gaussian fits to the data. The solid blue lines correspond to the expected temporal envelope, calculated from cuts through the JSIs, as indicated in Figures 3.18a and b.

delay trigger signal, and then treated in a series of slicing, binning, and background subtraction operations in order to obtain the temporal intensity profiles. The details of this procedure are compiled in appendix A. The profiles are presented in Figure 3.19. Again, the measured intensity envelopes were fitted with Gaussians. For comparison, the cuts through the JSIs along the signal axis were Fourier transformed to obtain a prediction under the assumption of a flat phase. These predictions are plotted in solid blue. As we can see, the FWHMs of the two curves are $\Delta\tau$=1.1±0.2 ps for the decorrelated state and $\Delta\tau$=2.0±0.2 ps, significantly above the predicted pulse durations.

From these numbers the TBP is easily calculated:

$$\mathrm{TBP} = \Delta\tau\Delta\nu \tag{3.13}$$

where $\Delta\tau$ and $\Delta\nu$ are the intensity FWHM of the temporal and spectral envelopes, respectively. From measurements one obtains TBPs for decorrelated and correlated state of TBP=1.1±0.2 and TBP=1.5±0.2, respectively, which are significantly above the expected values of TBP=0.57 and TBP=1.1. Note that these predictions under the assumption of a flat spectral phase are not required to be at the minimum value for a Gaussian of 0.44, but higher, since they were obtained from the measured spectra, not from Gaussian approximations. Especially for the anticorrelated and therefore multimode state, a higher TBP is to be expected, since the marginal spectrum is not Gaussian.

From these numbers alone, we can already conclude that both states are not spectrally pure. This is not all a surprise for the anticorrelated state, since with a mode number of K=2.10 (obtained through modal decomposition of the JSI) it wasn't expected to be pure anyway. The decorrelated state with a mode number of K=1.08, however, should be close to the Fourier limit. Therefore, it can be concluded that the JSA contains higher order spectral phase contributions invisible to the JSI. Still, the purity extracted from the JSI as

$$P = tr\left(\rho^2\right) = \frac{1}{\mathrm{K}} \tag{3.14}$$

forms an upper bound for the purity. $\rho$ is the density matrix of the state and $K$ is the cooperativity or Schmidt number.

The measurement alone does unfortunately not tell us where the higher order phase originates from, whether is comes from a chirped pump, chirped phasematching, or occurred even through dispersion behind the source. It is known that for example a chirp on the pump influences both purity and TBP of the generated photons [88, 87]. Assuming that the chirp was introduced before or during generation of the photon pair is the worst case, which can easily be modeled. Here, the following recipe is used: From the known parameters of the source, such as dispersion data for the waveguide, phasematching- and pump bandwidths, a joint spectral amplitude which includes a pump chirp, is calculated. The associated JSI matches the measured one in shape and Schmidt number K, but is blind to the chirp. Then, through Schmidt decomposition of the JSA, the real Schmidt number and purity are extracted. A Fourier transform allows to extract the TBP, analog to the evaluation of the measurement. This is done for both PDC states. The results are displayed in Figure 3.20.

Through equation 3.14 we can see that the respective purities for zero chirp match the measured ones. The solid lines correspond to the purity extracted from the model, the dashed lines to respective TBP divided by the ideal (Fourier-limited) TBP. The red lines indicate the points where the measured TBP is reached, allowing to extract both the purity and PDC pump chirp. This chirp parameter C is defined as $\exp(i\omega^2 C)$. The extracted chirps are $15616\,\mathrm{fs}^2$ and $21400\,\mathrm{fs}^2$, respectively, which correspond to TBPs 1.92 and 1.36 times the respective Fourier limit. These chirps correspond to the dispersion of 0.81 m and 1.11 m of silica glass, respectively. The estimated numbers for the decorrelated and anticorrelated states' purity are 0.656 and 0.472. Since attributing all of the chirp to the PDC pump is essentially the worst case, these can be seen as lower bounds for the purity, placing the purity of the decorrelated state between 0.656 and 0.93, and the purity of the anticorrelated state between 0.472 and 0.48. It strikes the eye that apparently the decorrelated state is affected by the chirp in a much more drastic way, while the purity of the other state barely changes. Hence, the TBP seems to be a much more sensitive measure for the presence of chirps than the purity. The purity can also be measured using the unheralded second order correlation function $g^{(2)}(0)$ [80], which is sensitive to chirps, but will not hint towards the presence of higher order spec-

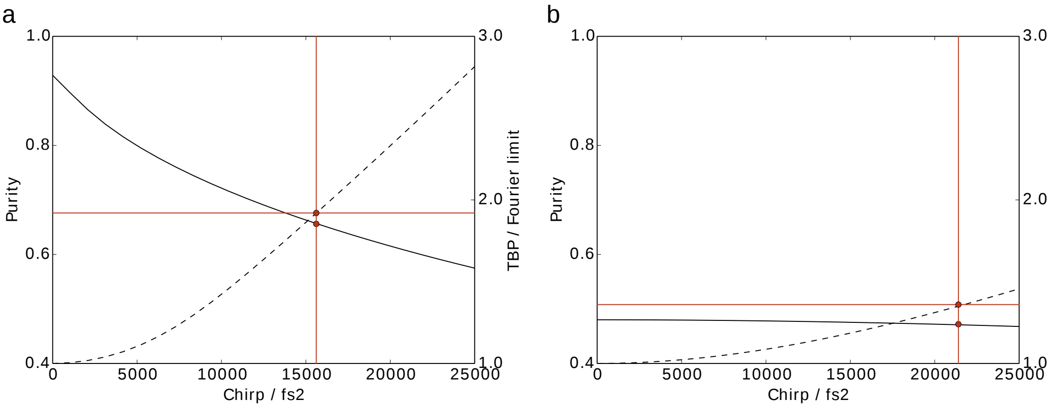

Figure 3.20.: Simulated data of a PDC source with the same properties as the one employed in this work. The solid line shows purity over pump chirp. The dashed line shows how far the produced state is above the Fourier limit. The dots indicate the point corresponding to the measured state: Panel (a) shows the simulation for the decorrelated state with $\Delta\nu_{PM}/\Delta\nu_{pump} = 1$, panel (b) shows the correlated case with $\Delta\nu_{PM}/\Delta\nu_{pump} = 3.25$

tral phases, due to the insensitivity of the purity to such phases for multimode states. Simply put: The $g^{(2)}(0)$ can be used to dial in a flat-phase decorrelated state, but not an arbitrary flat-phase multimode state. Even if the $g^{(2)}(0)$ has already been used to optimize for zero pump chirp for a decorrelated state, the TBP will still reveal any sources of chirps behind the source, which is still of great importance for interference experiments or further nonlinear processing.

### 3.4.3. Outlook: Extension to X-FROG measurements

This optical single-photon cross-correlation technique is not just an extension of the QPG phasematching configuration, it can also enrich the functionality of the setup in the lab in many ways, such as identifying chirps on single photons, source optimization, and source characterization. Since delay devices are part of any pulsed nonlinear setup, the method can easily be implemented, even without the fast delay device employed here. Detecting the upconverted light on a spectrometer presents another promising extension: While the FROG is the extension of optical auto-correlation, the cross- or X-FROG is the analog extension for optical cross-correlation. It has already been discussed earlier that the output spectrum of the QPG is insensitive to the input spectrum at least in the limit of a broadband input, which unfortunately indicates that such a XFROG implementation would suffer from strong bandwidth limitations.

## 3.5. The quantum pulse shaper

**Quick summary**

The quantum pulse shaper is nothing else than the reverse process of the QPG, i.e. a DFG process where the pump and idler group velocity is matched. This process, given a large pump bandwidth, has a transfer function at an angle of 90 degrees, i.e. parallel to the idler axis. This means, that whatever the spectrum the pump has, is transferred to the idler, allowing for controlled pulse reshaping. In this first experiment, this feature is to be characterized. All further measurements, such as efficiency or noise characteristics, would require a pulsed, ideally single-photon level input at 550 nm, which was not available at the time. To measure how well the spectral reshaping works, a spectrum is programmed on the pump pulse shaper, the output spectrum is recorded on a spectrometer, and the overlap between programmed and observed spectrum is calculated. To interpret the results, the experimental limitations and imperfections are modeled and compared to the observations.

### 3.5.1. Purpose and background

**The nomenclature of classical communication** Quantum communication in the pulsed mode framework requires, same as any telecommunication scheme, encoding and decoding devices as well as multiplexing and demultiplexing devices [46]. In this context, it is necessary to establish the nomenclature and draw connections between the nonlinear devices from quantum optics experiments and the devices used in classical fiber communication. In a classical scheme [31], the alphabet (zeros and ones, since a binary or two-dimensional alphabet is used) is encoded onto the degree of freedom of choice. The process of transmitting several information channels at once is called multiplexing. The multiplexer or add-device takes the channel, where information is already encoded, and adds it to a ensemble of other channels without modifying them. The channels occupy a different degree of freedom from the one used for encoding. For example, the classical encoding can be done on the phase of the signal (quadrature phase shift keying - QPSK), while the channels use different wavelengths (wavelength division multiplexing - WDM). The signal is then transmitted using a link of optical fibers. At the receiving end, the demultiplexer or drop device separates the channels one by one, and the information carried by each channel is decoded.

The same is done in quantum communication, where popular degrees of freedom for encoding are orbitall angular momentum [89, 90, 91], polarization

[12] and, last but not least, temporal modes [21].

**The QPG is a chameleon of telecom devices** The question is: What roles takes the quantum pulse gate here? The answer is complicated and depends on the application. Lets assume one wants to do quantum communication using a two-dimensional alphabet. Here, the encoding could be done in a pair of modes where “0” is one of them, “1” is the other. Then, multiplexing could be done, by using many temporal modes. One channel could occupy modes 0 and 1, one channel 2 and 3, and so on. In this case, the QPG detects which modes are present in the mix, effectively serving as decoder *and* demultiplexer at the same time. A different, much more appealing scenario would be to use a larger alphabet, where every “letter” of the alphabet occupies one temporal mode. Therefore, a large number of temporal modes would be already occupied by one channel, making additional multiplexing in another degree of freedom, such as wavelength or polarization, necessary. In this configuration, the QPG would only serve as decoder. In principle, it is thinkable to use time bin encoding, and use temporal modes exclusively for multiplexing, which would make the QPG exclusively a drop device. So far, the application using a large alphabet has been concretely discussed [92, 46] and offers significant security advantages over a two-dimensional alphabet encoding.

The necessary requirements for a “good” QPG have been summarized before [46]:

- Mode selectivity: How well is a target mode converted, and not an undesired mode?
- Mode separability: How much of this target mode is converted?
- Efficiency: How much of the input light is converted?

Here, high efficiency combined with high selectivity result in high mode separability.

**The role of the Quantum Pulse shaper** For a complete framework we require an encoder and add-device as well, which is dubbed the *Quantum Pulse Shaper* (QPS) in an analog fashion to the QPG. Just like the QPG, the QPS can be anything you like. Again, in the appealing application with a large alphabet, the QPS serves as encoder. To be more precise, the QPS would take a single photon prepared elsewhere (for example using a PDC source), and shape it into the desired temporal mode, or mode combination. In order for this device to function as intended, there are several requirements, which can be formulated analog to the QPG

- Mode selectivity: Is the light from the register mode only converted to one temporal mode?

- Efficiency: How much of the register mode is converted?

We see that the requirements have changed slightly. If a mode cannot be targeted correctly, it is not likely that a set of orthonormal target modes can be produced. However, even if the pulse shapes produced are orthogonal, the decoding process is much simplified if the shape of the modes is actually the intended Hermite-Gaussian basis. Here, we remind ourselves, that this assumption is not necessary for decoding with the QPG, but additional calibration becomes necessary, if either the exact shape of the input basis, or the measurement basis are not as assumed [51]. Hence, orthogonality is not required for the QPG, since at least it is fundamental that any input state can be decomposed in *any* basis, as long as we can produce a measurement in an actually orthogonal basis. For the QPS however, we add this requirement, since otherwise there would be "real" mixing between alphabet letters, not just "measurement induced" mixing. Efficiency obviously is desirably high, but a lack thereof merely affects the overall system performance, for example in terms of secure key rate. The selectivity of the conversion process is probed most easily in a spectral overlap measurement. This will be discussed in the following chapter.

### 3.5.2. The QPS' nonlinear process

The QPS is not only a "reverse" QPG in the sense that it is the encoder, whereas the QPG is the decoder for temporal mode based quantum communication, it also employs the reverse nonlinear process. Where the QPG uses a group-velocity matched sum-frequency generation:

$$\begin{aligned}&\mathrm{QPG:}\quad 1550\mathrm{nm(s)}\;+\;870\mathrm{nm(p)}\;\Rightarrow\;557\mathrm{nm(i)}\\&v_{g,s}\;=\;v_{g,p}\;>\;v_{g,i}\end{aligned}$$

the QPS uses a group-velocity matched difference-frequency generation:

$$\begin{aligned}&\mathrm{QPS:}\quad 557\mathrm{nm(s)}\;-\;870\mathrm{nm(p)}\;\Rightarrow\;1550\mathrm{nm(i)}\\&v_{g,s}\;<\;v_{g,p}\;=\;v_{g,i}\end{aligned}$$

Note that for both the QPG and QPS process, the role of the two matched fields can in principle be exchanged without changing the basic concept. This is actually done for the following QPS demonstration, since precise, absolute-frequency calibrated and actively stabilized pulse shapers are available for the telecom band at 1550 nm, which reduces the experimental effort significantly. In Figure 3.21 the experimentally measured phasematching for the QPG is shown again, alongside a phasematching for the QPS process, which is merely

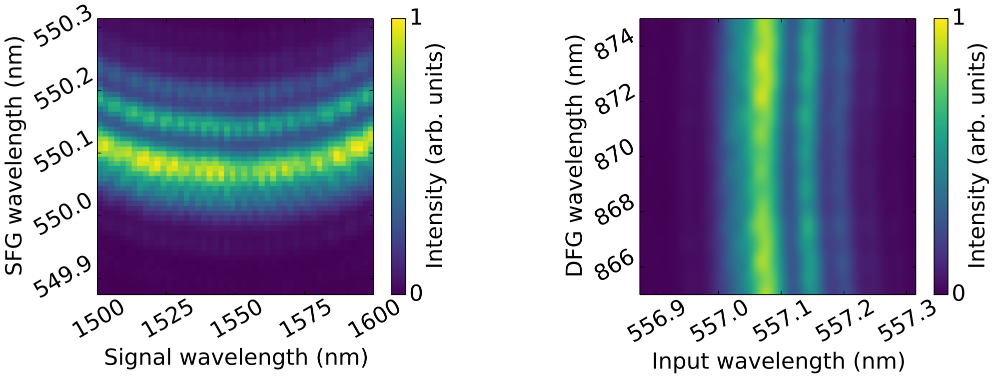

Figure 3.21.: Phasematching measurements of the QPG and QPS procces. Left: Phasematching measurement of the QPG process in the waveguide used here. Right: A QPS phasmeatching derived from the measurement in the left panel.

derived from the QPG measurement. This means, that the measured phasematching was turned by 90 degrees and rescaled according to the desired wavelength combination. This is a good approximation die to the low curvature in the used range. Figure 3.22 shows a cut through this phasematching, which was measured by scanning the dye laser over a fixed wavelength CW laser at 1550 nm. Unfortunately, the output wavelength of the dye laser can not be reproduced reliably enough to perform multiple scans and layer them to measure the full phasematching picture in two dimensions. However, the single scan shows that the phasematching along the signal axis is as narrow as expected, thus confirming the orientation of the phasematching, and within the resolution limit the side lobes are visible as well.

### 3.5.3. Classical characterization

**Mode selectivity** The principle of characterizing the mode selectivity is fairly simple. A target spectrum is programmed onto a pulse shaper, the light is fed through the nonlinear waveguide together with CW light, and the DFG spectrum is measured on a spectrometer. We only assume that all spectral phases introduced in the setup can in principle be compensated for, and therefore a spectral intensity measurement is sufficient for a first characterization. Hence, the setup is simple in comparison, especially since a commercial, fiber coupled pulse shaper (Finisar Waveshaper 4000s) is used. The setup is shown in Figure 3.23.

Both pump and input light are generated with a cascade of lasers. The pump light is generated by a cascade of the same Ti:Sapphire laser and OPO as used

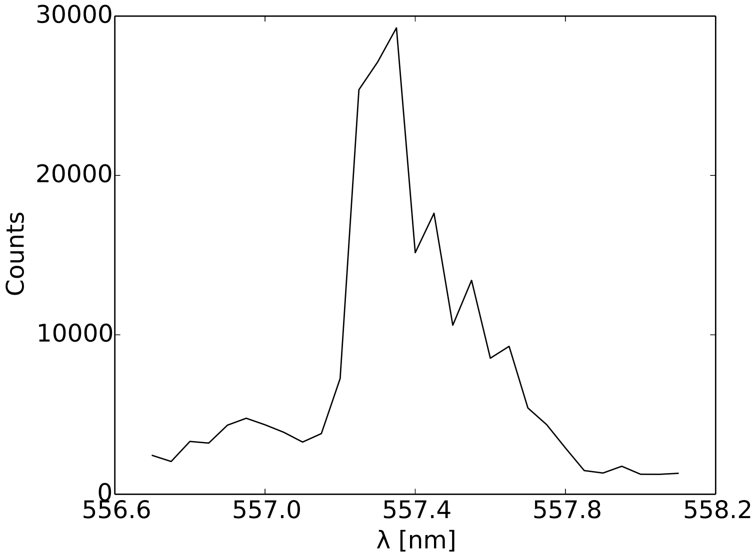

Figure 3.22.: A measured scan along the signal axis through the phasematching of the waveguide in the QPS configuration.

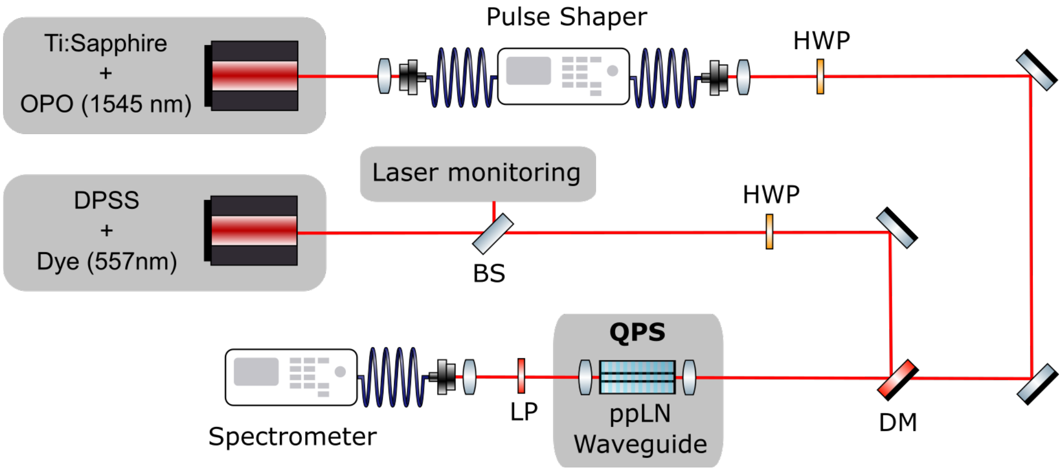

Figure 3.23.: Setup for the mode selectivity measurement of the QPS. OPO: Optical parametric oscillator, HWP: Half wave place, LP: Long pass filter, ppLN: Periodically poled Lithium Niobate, DPSS: Diode pumped solid state laser, Dye: Continuous wave dye laser, DM: Dichroic mirror, BS: Beam sampler.

in the other experiments. The 1550 nm light is coupled to single mode fibers, the spectrum is then shaped by a fiber-coupled pulse shaper, which employs an internal laser source for active stabilization and absolute-frequency calibration. The OPO provides pulses at 80.165 MHz repetition rate and a FWHM of 17 nm. The 557 nm input light is obtained using a dye laser (Radiant Dyes Standing Wave CW) which employs Rhodamine-560, dissolved in Ethylene Glycole, as a gain medium. It is pumped at 514 nm with a diode pumped Nd:YAG (Coherent Genesis), where the 1030 nm-line is pumped and frequency doubled. The laser dye is dissolved at a concentration of 250 mg/l, which is close to the maximum solubility of Rhodamine. The actual weight-concentration was increased slightly with each dye change to account for the increasing water content of the hydroscopic dye. Maximum optical output power achieved with the laser system was 160 mW at an optical linewidth of typically below 5 GHz. The linewidth was monitored during experiments using a 20 mm-long scanning Fabry-Perot cavity with mirror reflectivity of 99 %. Central wavelength was monitored using an Ocean Optics USB2000 spectrometer, which also served as a means of automatizing wavelength tuning.

In principle, it is possible to obtain the input wavelength of 557 nm using light from the OPO at 1114 nm and a home-made SHG crystal. However, this would fix the OPO wavelength, and we would lack 1550 nm pulses. To pump the process with the alternative 870 nm is also not possible, because the low OPO output wavelength fixes the Ti:Sapphire wavelength to below 800 nm. Therefore, the laser combination used here was the only option of producing all necessary wavelengths without purchasing additional lasers.

The two beams are combined on a dichroic mirror and coupled to the exact same waveguide also used in the cross-correlation and bandwidth compression experiments presented before. The output light and pump are separated from the residual 557 nm input using a long pass filter. The remaining 1550 nm pump and 870 nm DFG output are coupled to a single mode fiber, and finally to a spectrometer (Andor Shamrock 500 with Andor emCCD camera). A 1200 lines/mm grating provides 0.05 nm resolution at 870 nm. The 1550 nm light is used to pre-align the fiber coupling, but does not disturb the final measurement, since the silicon-based sensor of the camera is insensitive to it.

The mode selectivity is then verified as follows: As a target spectrum we choose the first 5 Hermite-Gauss modes. For each mode, the bandwidth of the underlying Gaussian is varied between 0.25 and 10 nm. For each set of parameters, 8 spectra with 4 seconds integration time each are measured. Therefore, 320 measurements are taken for every mode. The entire set of measurements is completed within a couple of hours. Then, an overlap integral between the target spectrum and the averaged 8 spectra for each parameter set is computed. The standard deviation of the overlap with each of the 8 individual measurements is used to generate error bars. For this overlap integral the spectra (modeled and measured) are area-normalized:

$$OL = \frac{\left(\int S(\lambda)T(\lambda)\right)^2}{\int S^2(\lambda) \cdot \int T^2(\lambda)} \tag{3.15}$$

where $S(\lambda)$ and $T(\lambda)$ are the measured and modeled target spectra, respectively. The model contains experimental limitations and will be discussed further on. The results are displayed in Figure 3.23.

The magenta points are measured overlaps. The dashed black lines denote 90 % overlap. It can be seen that for moderate bandwidths around 4-5 nm this goal is met for all 5 modes, however, there are significant deviations for the smallest and largest bandwidths. The deviations are larger for higher order modes, which is not surprising because they are in general more complex (more nodes) and occupy a larger spectrum (since the underlying Gaussian is scaled up by the Hermite polynomial). These are modeled by modifying the target spectrum with known experimental limitations, and calculating these model spectra's overlaps with the target spectra. This model overlap is shown as solid lines. We can see that the general trend of the model is followed, however, the measured overlap is lower in general, and systematically much lower for large bandwidths.

The model incorporates several experimental imperfections originating in the input and pump lasers, pulse shaper, nonlinear process and measurement. The first one is insufficient pump bandwidth.

Figure 3.24 shows its influence for the first five Hermite-Gauss orders.The effect has actually three sources. The first is pump laser bandwidth of 17 nm, and the second is limited phasematching bandwidth, which factors in at 20 nm. The third effect is the limited range of the pulse shaper, which cuts the spectrum outside of the telecom C-band, below 1530 and above 1565 nm. The model spectrum $M(\lambda)$ has been calculated from the target spectrum $T(\lambda)$ as follows:

$$M(\lambda) = F(\lambda) \cdot T(\lambda) \tag{3.16}$$

where F is the described filter function that cuts the spectrum, which is the product of two Gaussians of 20 and 17 nm FWHM, and is cut outside the telecom C-band. The limited bandwidth only affects large bandwidths.

The second contribution is what shall be called “convolution effects”. They stem from limited shaping and measurement resolution as well as the quite substantial linewidth of the dye laser. Here, the model spectrum $M(\lambda)$ has been calculated from the target spectrum $T(\lambda)$ through convolution with the

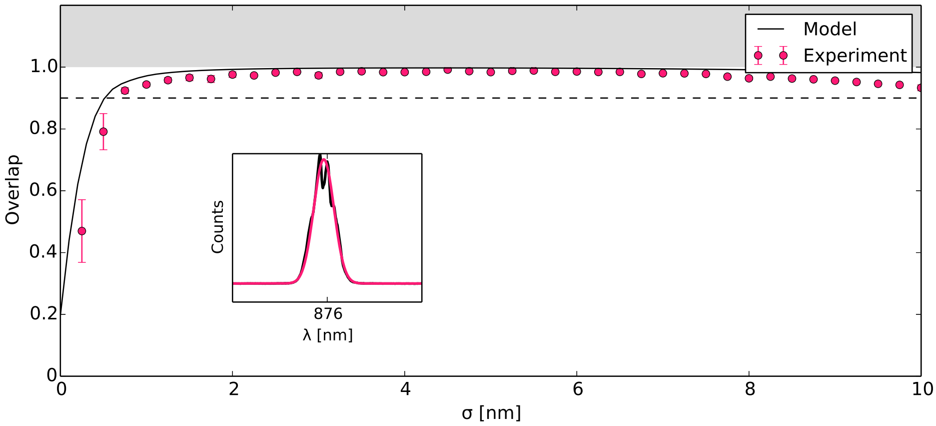
Model
Experiment
Overlap
1.0
0.8
0.6
0.4
0.2
0
Counts
876
λ [nm]
0
2
4
6
8
10
σ [nm]

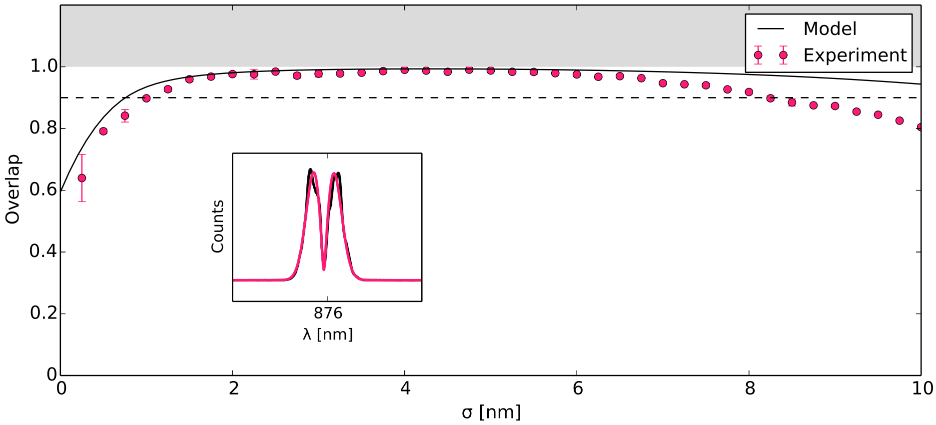
Model
Experiment
Overlap
1.0
0.8
0.6
0.4
0.2
0
Counts
876
λ [nm]
0
2
4
6
8
10
σ [nm]

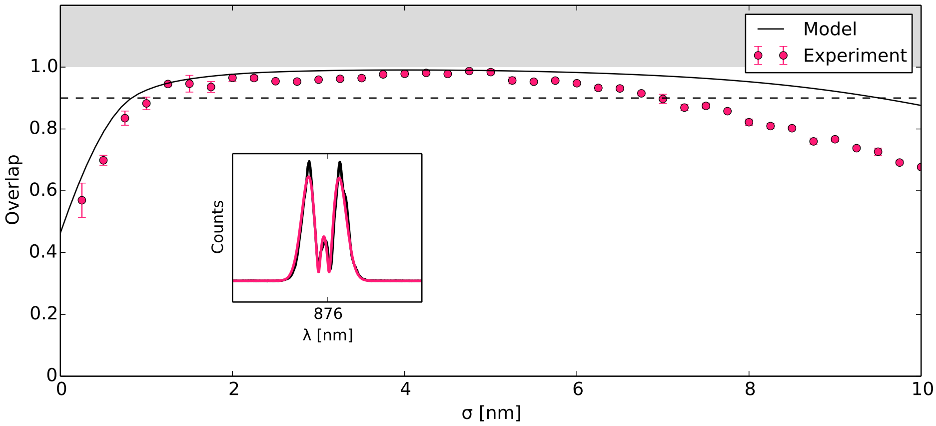
Model
Experiment
Overlap
1.0
0.8
0.6
0.4
0.2
0
Counts
876
λ [nm]
0
2
4
6
8
10
σ [nm]

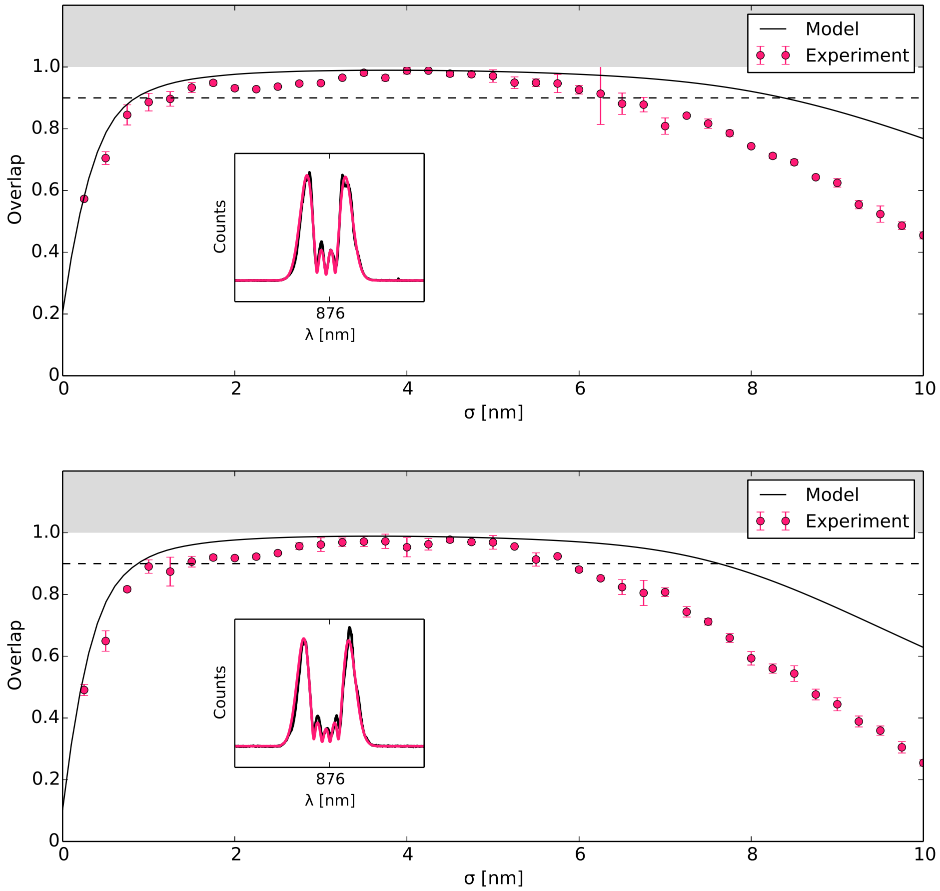

Figure 3.23.: Overlap between the programmed and measured Hermite-Gauss spectra for the first five modes. Magenta symbols indicate the measured overlaps. The dashed lines indicate a overlap of 90 %. Solid black line indicate the overlap between the programmed and modeled spectrum, which includes experimental limitations. The inserts show the programmed modeled (magenta) and measured spectra (black) for each mode and a bandwidth of 5 nm.

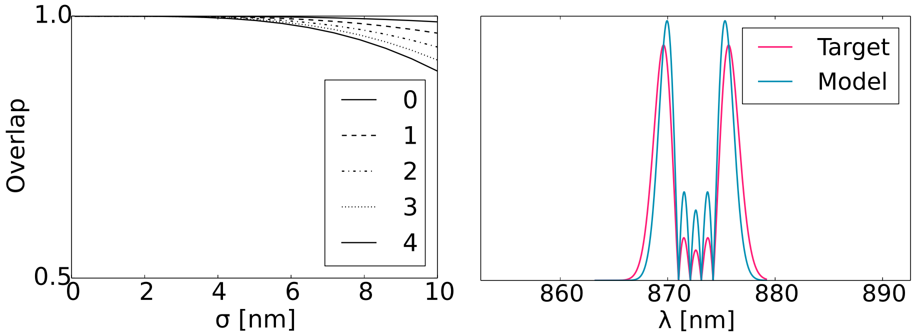

Figure 3.24.: Overlap for five first Hermite-Gauss modes with limited pump bandwidth, phasematching bandwidth and shaper range (left). Target and model spectra for the fourth order mode and a bandwidth of 10 nm (right)

experimental Gaussian response function:

$$M(\lambda) = \int d\lambda' T(\lambda') \exp\left(-\frac{(\lambda - \lambda_0 - \lambda')^2}{2\sigma_m^2}\right) \tag{3.17}$$

with

$$\sigma_m = \sqrt{\sigma_1^2 + \sigma_2^2 + \sigma_3^2} \tag{3.18}$$

Here, $\sigma_m$ is the standard deviation of the combined experimental response function, containing the shaper and spectrometer resolution of $\sigma_1 = 5\,GHz$ and $\sigma_2 = 0.05\,nm$, respectively, and also the dye laser bandwidth of $\sigma_3 = 5\,GHz$.

The effect of this contribution to the model is shown in Figure 3.25. The effect is only apparent for the smallest of bandwidths. Two examples of model spectra for the forth order are displayed in Figures 3.25b and c. While the limited overall system resolution completely blurs the target spectrum for 0.1 nm bandwidths, the effect is barely visible for 5 nm, where it only slightly diminishes the visibility of the dips.

The last effect modeled originates again from the dye-laser. As the only available light source at the desired wavelength, it comes, unfortunately, with some performance limitations. The laser employs a birefringent filter inside the cavity for tuning. Within its filter passband, two cavity modes can in principle participate in lasing. On a scale of seconds, mode competition and jumping between these two lines can be observed. The observed spectra contain effectively a contribution from both. Especially for small bandwidths, or sharp features in general, this effect reduces the observable overlap drastically. The model is shown in Figure 3.26

The effect is very similar to the convolution effects discussed earlier. The spectrum is significantly widened and overlap is lost. This also affects mostly

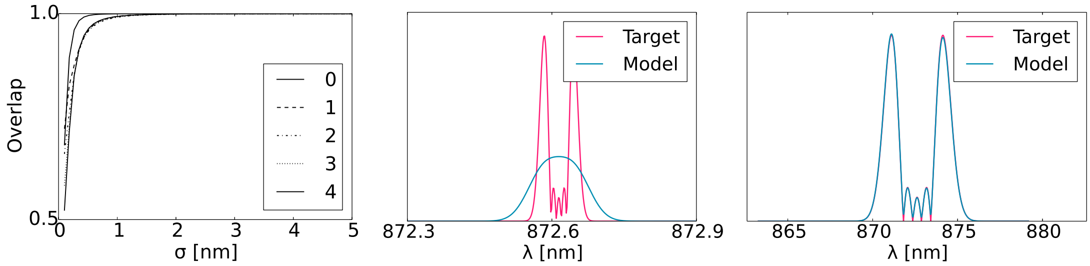

Figure 3.25.: Overlap for five first Hermite-Gauss modes with limited system resolution (left). The right two panels show target and model spectra for the fourth order mode and a bandwidth of 0.1 nm and 5.0 nm, respectively

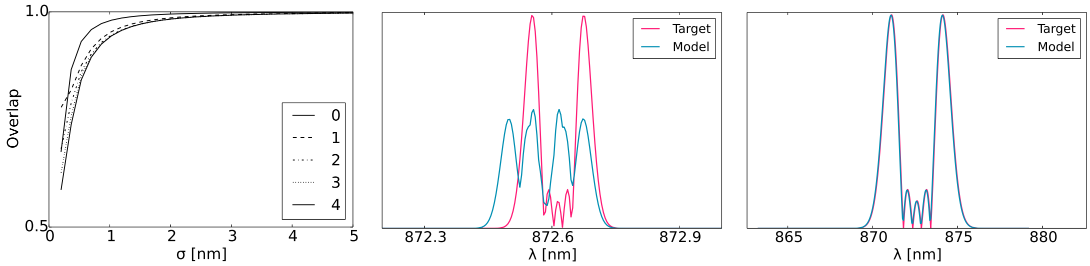

Figure 3.26.: Overlap for five first Hermite-Gauss modes with simulated mode competition of the laser (left). The right two panels show target and model spectra for the fourth order mode and a bandwidth of 02. nm and 5 nm, respectively.

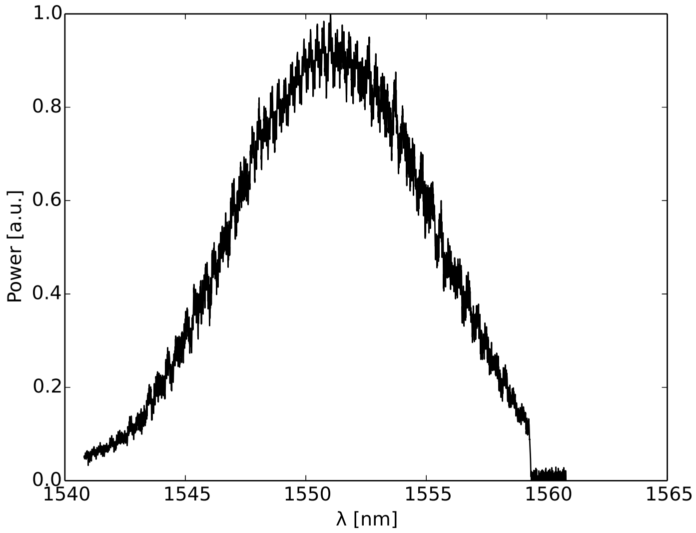

Figure 3.27.: Pump spectrum for the zero order Hermite-Gauss mode and a bandwidth of 10 nm.

smaller bandwidths, but not as small as the convolution effect. For very small bandwidths, the effect is even more pronounced, however, for the shown bandwidth of 5 nm the model spectrum cannot be differentiated from the one with convolution effects.

The one thing that cannot be reliably modeled is that the pump spectrum is not actually Gaussian. Some interference and loss effects cause fringes on the spectrum. In Figure 3.27 the pump spectrum for the fundamental spectral mode with a FWHM bandwidth of 10 nm is shown, where the fringing as well as the cut spectrum due to the shaper's limited range can be clearly observed. The spectrum was measured using an optical spectrum analyzer via a second output port of the pulse shaper, to which 10 % of the total intensity was directed. The output was found to be uniform across all four output ports.

The effect of normal distributed noise on the spectrum was modeled, but excluded here since the effect was minor. It is discussed in Appendix B.

**Conversion efficiency** Measuring the conversion directly in the current setup is not possible without assumptions, because a continuous wave signal and pulsed pump laser are used. There are two ways of estimating the conversion efficiency. Either, one measures the count rate of the unconverted light, and compares the count rate with the pump turned on or off. The depletion of the throughcoupled signal gives a direct measure of internal conversion efficiency and has also been used in the bandwidth compression characterization (chapter 3.3). This is not possible, because the depletion dip in the throughcoupled

CW signal is too small and on a very short time scale. The time scale of overlap with the pump in the crystal is exactly the pulse length of the QPG output. This has been measured for this exact waveguide to be 27 ps [93]. In comparison, the temporal jitter of the detection system is of the order of 100ps. Therefore, even at 100 % internal conversion efficiency, only a visibility of 25 % can be expected. However, no dip could be identified. Unfortunately, the intensity fluctuations of the input dye laser alone amount to roughly 10 %, obscuring the measurement even more.

A second way is to measure the converted counts, characterize all couplings and linear losses, and measure the unconverted counts. Here, the above assumption on the temporal overlap has also to be taken into account. Unfortunately, the final fiber coupling of the 870 nm light into the fiber cannot be measured accurately, since the spatial mode combination coming out of the waveguide is unclear, and impact the coupling efficiency drastically. Due to the massively higher counts for the unconverted light (CW light), an additional ND filter was used here, which was also characterized beforehand. After careful characterization of all couplings and losses, the internal conversion efficiency was estimated to be 0.5 % within the time interval, where the signal and pump travel through the waveguide together, at a pump pulse energy of 20 pJ. For comparison, the QPG process in the same waveguide achieves a conversion efficiency of 61.5 % at 1.5 nJ pump pulse energy. Such a high pump pulse energy cannot be provided by the laser system in the current configuration.

**Alignment procedure**

The alignment of this experiment is fairly time consuming compared to the previously presented experiments, mostly due to the problematic dye laser system.

Assuming that the laser has been filled with fresh laser dye recently (less than 2-4 weeks ago at maximum), the alignment starts by optimizing the output power of the dye laser. Adjust all 3 cavity mirrors carefully. The rear mirror is very sensitive and hardly ever has to be aligned. The pump mirror assembly is the component most prone to misalignment and has to be adjusted daily. While aligning, observe the spectrum on the Ocean Optics spectrometer, since there are two dominant cavity modes. Try to suppress one, partially blocking the cavity mode with the alignment aperture can help.

Next, align the waveguide coupling for the green light. It is not important to do this first, since there is no preferred focus position for the incoupling lens - this would be only the case if one of the inputs is at the single-photon level. The output mode of the laser is not very clean, therefore no larger throughcoupling efficiency than 10 % can be expected.

Next, align the OPO fiber input coupling. You can then use an optical spectrum analyzer or spectrometer to measure the central wavelength. This is necessary because the OPO's internal wavemeter is inaccurate (even on a day-to-day basis). Make sure that the pulse shapes programmed on the pulse shaper are centered on the laser spectrum. Program a large bandwidth to measure the central wavelength, and a more narrowband 1st order Hermite-Gauss function to check that both spectra are centered. Note that the mismatch of the OPO wavemeter can be as large as 5 nm.

Next, couple the 1550 nm beam through the waveguide, and into the fiber. Having both waveguide couplings and the fiber coupling aligned to at least 10 % should be sufficient to observe the DFG output on the spectrometer and use it directly for further alignment. Remember that the fiber coupling still needs to be aligned for the DFG output wavelength using the spectrometer signal, and that the waveguide incoupling lens can usually be moved to a more optical focus somewhere in between the optical foci for 1550 nm and 557 nm.

### 3.5.4. Outlook: Limitation for pulsed operation

The model can serve as a means of estimating the ultimate limitations for the quantum domain. For this, it is necessary to exclude all *auxiliary device dependent* contributions, which are limitation arising firstly from devices other than the waveguide itself, such as laser, pulse shaper and detection, and are secondly not fundamental, but rather of a technological nature. This excludes the convolution effects from input laser and spectrometer, as well as the problem of limited available bandwidths. We are left with convolution effects stemming from the input photon bandwidth and signal phasematching bandwidth, and the limited idler phasematching bandwidth.

The input photon's spectral bandwidth could be as wide as the the signal phasematching (for the current waveguide: 0.1 nm [47]). If the input spectrum were to be more broadband, it would be cut by the phasematching, causing insertion loss. With such a wide input spectrum the pulse shaper's resolution of 10 GHz will be small in comparison and neglected. The phasematching bandwidth along the output axis is mostly limited by the phasematching's curvature and would thus not strongly depend on the bandwidth, but is taken into account. This will result in a limitation for high shaping bandwidths identical to the one shown in Figure 3.23, but weaker, since the limited pump bandwidth is neglected. Using those benchmark numbers, calculations identical to the model already presented were prepared to simulate the effect of the input and phasematching bandwidth on pulsed operation performance.

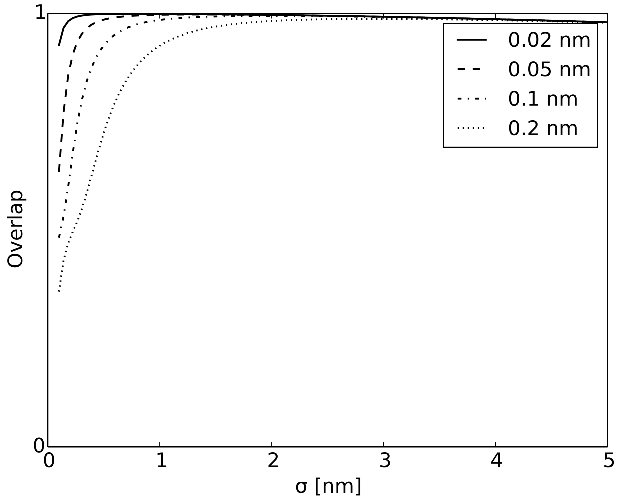

Figure 3.28.: Overlap between the programmed and modeled spectra of the forth Hermite-Gauss order for various phasematching bandwidths.

The limitations are stronger for higher order modes, because they have more narrowband features and a higher overall bandwidth. Therefore, only the result for the 4th order Hermite-Gauss mode in Figure 3.28, since it is the highest order treated here. It can be seen that for a more narrow phasematching bandwidth than the one for the waveguide used in this work, shaping bandwidths under 1 nm is certainly possible. This is highly desirable in the light of optical fiber dispersion and spectral information density. At the same time, high shaping fidelity for small bandwidth features also allows to shape higher order modes efficiently. There is only a weak limitation for high bandwidths.

### 3.5.5. Outlook: A demonstration of broadband pulsed mode rotation

Since the QPS reshapes photons, it can be used to change their temporal mode. However, it can only operate on light at 557 nm, or in general a register mode at visible wavelength. Therefore, direct mode rotation of telecom single photon is not possible and would require an additional QPG in front of the QPS. The two combine could tackle the task of picking a single temporal mode from a multimode state like demonstrated in [42] and then reshaping the light in that mode to a different temporal single mode. This process has been proposed in [46]. While doing so, the basis width in terms of Gaussian bandwidth could be changed as well, for example to interface between different communication network systems. A complete setup for this application is depicted in Figure 3.29.

For efficiency and noise measurement, the output can be detected using an SNSPD. The spectral intensity can be measured on a spectrometer. For a proper experimental modal decomposition, the detection would have to be done using a second QPG. All in all, the setup becomes quite complicated: Three SLM-based pulse shapers are necessary, or four if a second QPG is used, with a total of four nonlinear waveguides. In principle, the back-and-forth conversion with reshaping can be implemented in a single pass in one waveguide [94], however, has not yet been demonstrated on the single photon level. In fact, no one outside this research group has so far demonstrated a QPG on the single photon level.

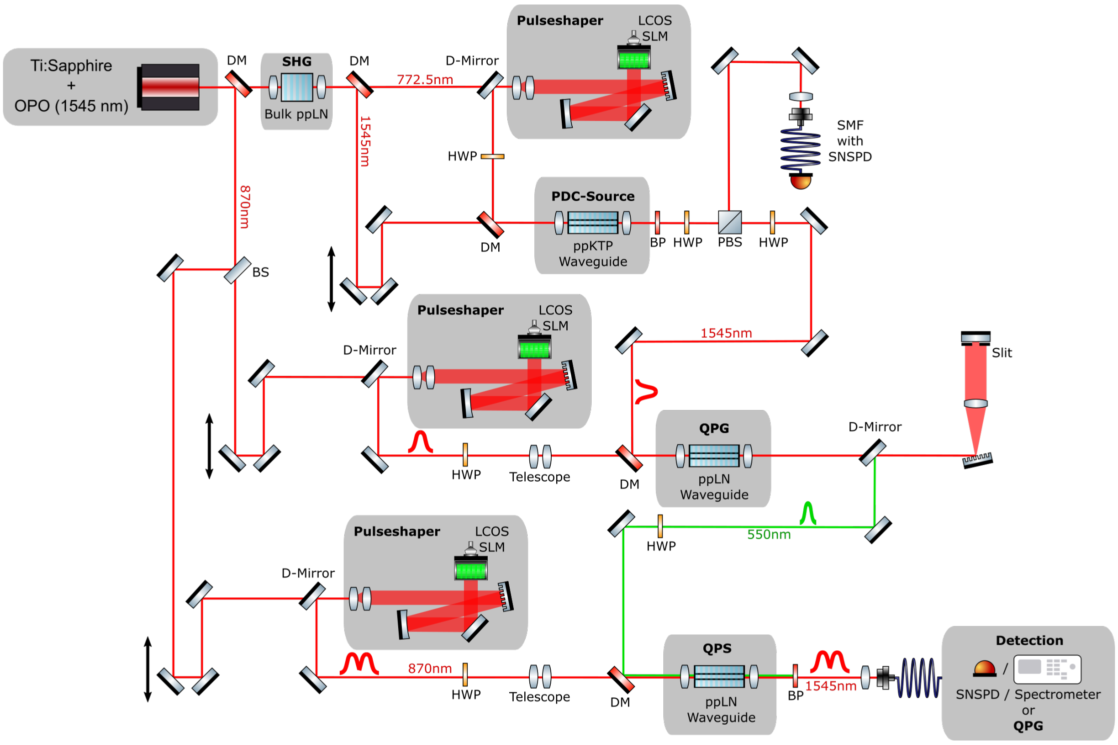

Figure 3.29.: Setup for temporal mode generation and rotation. The setup used a KTP PDC source to generate photons, a QPG to convert a selected mode to the green, and a QPS to back-convert and reshape into a different temporal mode in the telecom band. OPO: Optical parametric oscillator, BS: Beam splitter, PBS: Polarization beam splitter, HWP: Half wave plate, LP: Long pass filter, ppLN: Periodically poled Lithium Niobate, ppKTP: Periodically poled Potassium Titanyl Phosphate, LCOS-SLM: Liquid-crystal-on-silicon spatial light modulator, SNSPD: Superconducting nanowire single photon detector

CHAPTER 4

# TIME DOMAIN UPCONVERSION DETECTION

In third chapter will outline the complete process of designing a tailored nonlinear device for a novel task, upconversion time-domain detection, will be outlined. This chapter will outline the complete process of designing a tailored nonlinear device for a novel task, upconversion time-domain detection. This includes extending the concept of controlling the spectral transfer function of a process to the temporal transfer function. After general considerations, a summary of a proof of principle experiment will be presented, followed by a design road map for unsuitable processes for the final design. That chapter will walk the reader through all steps: Practical requirements will be discussed, suitable spectral and temporal correlations identified, put into context with suitable wavelength combinations and expectations on efficiency, and in the end performance benchmark measurements will be presented. The results of the described proof-of-principle experiment were previously published in [93]

## 4.1. Introduction

### 4.1.1. Time-domain measurements

Time domain measurements of light have been of interest for a long time. The two most popular direct measurement techniques for temporal intensity profiles are optical auto-correlation [75, 95], and the streak camera, a device developed in the 1980's [96]. Streak cameras use photo-cathodes to perform a optical-to-electric conversion, similar to a photo multiplier tube (PMT). The electrons are then deflected using an alternating high voltage, which constitutes a mapping from arrival time to a transverse spacial coordinate. Streak cameras are especially popular in the semiconductor community, as the second, free spatial coordinate can be used to resolve the spectrum, allowing to measure time-resolved spectra. Other usage of the second coordinate are also possible [97, 98]. For example, it can be used to resolve individual pulses, especially useful in single photon measurements [78, 99, 100].

While other methods to measure the temporal profile of pulses of light exist, they measure the spectral intensity and phase, allowing for a complete Fourier transform. Such techniques are namely SPIDER [101, 102], that employs spectral shearing interferometry, and FROG [76], where SHG produced from identical but temporally shifted pulses is spectrally resolved.

In the few examples of dim light streak camera measurements, be it the characterization of semiconductor systems [103, 104, 105, 100], fluorescence and parametric down-conversion [106], or organic molecule emission [79], the wavelength of the measured light was always shorter than 900 nm. In the visible and near infrared region, cathode materials are available that provide high quantum efficiency of the order of 10 %, while offering low noise at the same time.

Pletnev *et al.* [107] hint that a prototype for a sensitive infrared streak camera with metal-silicon-metal photocathode exists, and the author received rumors about the device, but so far, no manufacturer offers information.

### 4.1.2. Upconversion detection

In the early 1980s, when cathode materials for the infrared spectrum were not available yet, upconversion was used to perform measurements of infrared light using a photo multiplier tube (PMT) [108]. Since streak cameras are very similar to PMTs, the technique was soon employed to temporally resolve emission of an InGaAsP diode laser [22].

The upconversion technique was soon abandoned, when cathode materials allowing direct detection became available [109] at least for wavelength as large as 1600 nm [110], and was rarely afterwards. Later examples include mid-infrared measurements [107]. It will be shown here, that the technique is still of substantial value today, especially in the advent of semiconductor-based single photon sources such as quantum dots [6, 7].

Especially for quantum light, high detection efficiency is a key resource. Until recently, the best click detectors were available in the visible and near-infrared range, which is why upconversion was harnessed to efficiently detect infrared light [111, 112, 113].

### 4.1.3. General considerations: Efficiency and resolution

The idea is really simple. Let's assume the quantum efficiency of a detector is $\eta_0$ at the initial (emission) system wavelength $\lambda_0$, but a more efficient detector with efficiency $\eta_1 > \eta_0$ is available at $\lambda_1$. To achieve a better overall detection efficiency, light is converted from $\lambda_0$ to $\lambda_1$. Tthe external conversion efficiency $\eta_c$ of the used frequency conversion process has to be larger than

$$\eta_c = \eta_0/\eta_1 \tag{4.1}$$

As an example, he best InGaAs APDs for detection at 1550 nm have a efficiency of roughly 20 %, while Silicon APDs for detection of visible light with efficiencies of roughly 60 % are available. A suitable frequency conversion device needs therefore an external efficiency (including linear losses such as coupling losses) of at least 34 %, which is roughly the state of the art [112]. The matter is much easier for photocathode based detectors such as PMTs and streak cameras. The difference in efficiency for the most common infrared-sensitive photocathodes and materials available for detection of visible light is several orders of magnitude [114]. Therefore, a suitable upconversion process needs only little conversion efficiency to already enable improvement.

Regarding the quantum efficiency of the streak camera itself, it is noteworthy that it is possible to optimize the SNR by employing strong electron multiplication to the extent of creating an electron avalanche for a single photon event, together with carefully calibrated background subtraction. This makes single photon measurements in principle easier in terms of achievable SNR [115, 100]. However, due to the avalanche effect, the maximum saturation of the phosphorus screen is reached even for a single photon detection. This makes analog integration i.e. the integration of the signal through camera exposure times much longer than the repetition rate, impossible due to the long decay time of the phosphorus response, i.e. dead-time. Therefore, the reduction of repetition rate to the time scale of phosphorus afterglow and camera frame rate is required in order to exclude multiple detection events in the same location of the screen. Thus, the measurement is more difficult to set up and more time consuming.

Efficiency is not the only thing that has to be considered. Click detection has the advantage that merely the presence of *something* is detected. Click detectors are usually "non-vacuum detectors“ that are triggered by anything from a single photon to a bright laser pulse. The detector itself does not resolve any additional degrees of freedom, but this is not the case for streak cameras, where the temporal intensity envelope is being measured. Therefore, the pulse shape has to be preserved by the upconversion process. This is best visualized by taking the spectral transfer function $\Psi(\omega_s, \omega_i)$ defined in chapter 2.5, and performing a Fourier transform. The resulting temporal transfer function $\hat{\Psi}(\tau_s, \tau_i)$, where $\tau_s, \tau_i$ describe the signal and idler field's arrival times relative to an arbitrary reference:

$$\hat{\Psi}(\tau_s, \tau_i) = \iint d\tau_s d\tau_i \Psi(\omega_s, \omega_i) e^{-2\pi i(\omega_s \tau_s + \omega_i \tau_i)} \tag{4.2}$$

An exemplary temporal transfer function is sketched in Figure 4.1. It can be seen that for a elliptical transfer function (which assumes that both phasematching and pump can be approximated by a Gaussians) terms like the resolution $R$ and point-spread-function ($PSF$), magnification $M$ and apertures, analog to their counterparts in spatial imaging, are easily defined purely from geometric considerations. It is obvious that these parameters stand in a close relationship to each other, and are all linked to the ellipse angle $\varphi$, as well as the width $\Delta\tau$ along the narrow axis of the double-Gaussian ellipse:

$$M = \tan M \tag{4.3}$$

$$PSF = \frac{\Delta\tau}{\cos\varphi} \tag{4.4}$$

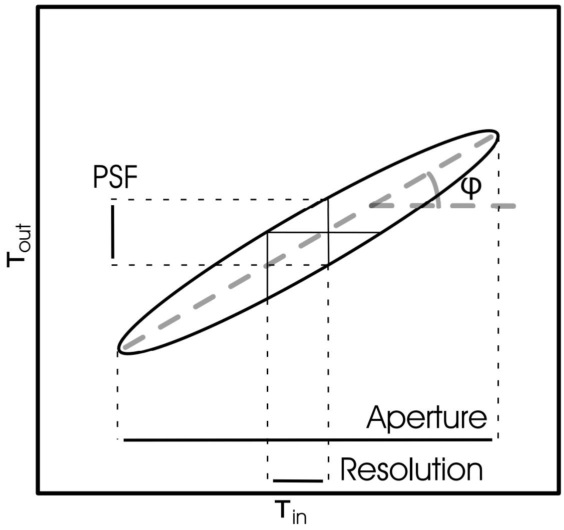

Figure 4.1.: Sketch of a temporal transfer function without any particular group velocity matching

$$R = \frac{\Delta\tau}{\sin\varphi} \tag{4.5}$$

These parameter's descriptive meaning is quickly explained. The magnification describes by what factor a temporal envelope will be stretched. A magnification larger than one describes stretching, smaller than one describes compression. A negative sign corresponds to a flipping of the pulse. The resolution describes how close two arbitrarily short pulses can be separated to still be resolved on the idler side, idler detection resolution ignored. The PSF corresponds to the temporal duration that an arbitrarily short input pulse will have on the output side.

In summary, the main difference between upconversion in the time domain and ordinary upconversion click detection is that in the time-domain, there is something to lose. Any realistic process will deteriorate the pulse shape somehow through limited conversion resolution. This may be acceptable since the detector will also have limited temporal resolution. Taking spectral response of click detectors into account, the aperture problem is not new and may be present both in time domain and click detection. However, the possibility of pulse stretching further increases the practicality of the technique. Not only can the efficiency of the overall apparatus be improved, but also the temporal resolution.

## 4.2. Proof-of-principle experiment

To showcase the usefulness of upconversion processes for time-domain measurements, a proof-of-principle experiment was performed, mainly focusing on efficiency issues. A streak camera was provided by our collaborators in Manfred Bayer's group at the TU Dortmund, and the previously used QPG sample was employed to upconvert yet again light from the PDC source set up in our lab. The experiment was able to show that upconversion on the single photon level also works with streak camera detectors, which is the main novelty compared to previous work on upconversion detection [113]. This result was accompanied by a review of noise sources in such devices, which are partially identical with the ones found in photo multiplier tubes, but extend beyond that. In this section, the experiment will be outlined along with a brief discussion on the transfer function of the employed nonlinear process.

**Quick summary**

The experiment focuses only on the aspect of overall detection efficiency. The principle is therefore simple and does not involve actually resolving any pulse shapes. The only goal is to observe a infrared single photon signal on a streak camera by using a sufficiently efficient frequency conversion in between. Here, the photon source is the usual PDC source, and the frequency converter is the QPG.

### 4.2.1. Experimental apparatus

Same as in previously presented experiments, the light source used here is a decorrelated telecom PDC source, identical with the one used in [47, 48], based on the principals outlined in [18, 2]. The upconversion setup is again identical with the one from [47], except that the detection is now carried out with the streak camera. Since the streak camera does not allow for heralded detection, the measured signal is effectively a non-heralded thermal state at the single photon level. The complete setup is depicted in Figure 4.2.

Figure 4.3 contains a rough outline of the streak camera's inner components. The input port is shielded by an additional aperture made of black cardboard that shields some stray light. Inside is a bandpass filter that provides some spectral suppression of stray light. Directly at the input sits a photocathode onto which the light is focused. From the photocathode, electrons are emitted for a portion of the impinging photons. This portion is material dependent. Available materials have long been optimized and have not changed much since the 1970's [114, 110, 116]. The electrons are then ac-

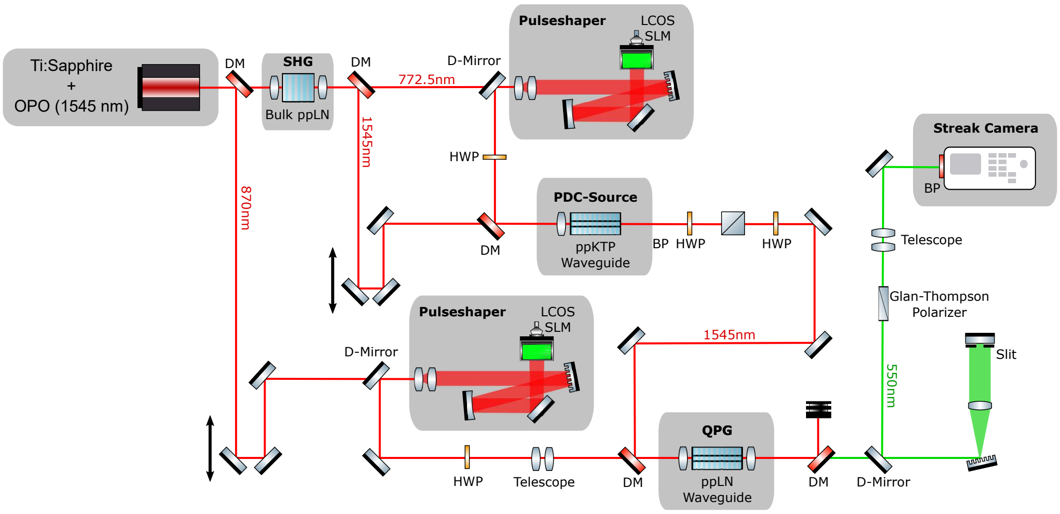

Figure 4.2.: Setup used in the experiment. Ti:Sa: Titanium Sapphire laser, OPO: Optical parametric oscillator, SHG: Second harmonic generation, LCOS SLM: Liquid-crystal-on-silicon spatial light modulator, BP: Band pass filter, PBS: Polarizing beam splitter, DM: Dichroic mirror

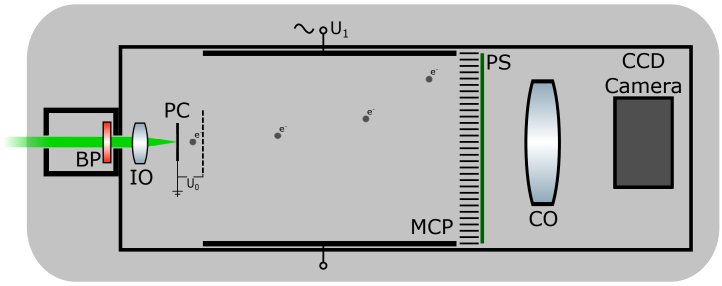

Figure 4.3.: Sketch of the streak camera. BP: bandpass, IO: Incoupling optics, PC: Photocathode, CO: Camera objective, MCP: Multi channel plate, PS: Phosphorus screen, CCD: Charge coupled device

celerated through a transverse, time-depending electric field. The sinusoidal voltage is synchronized to the laser repetition rate, so that the deflection of electrons arriving at a certain delay from the laser trigger signal is identical for each pulse. Therefore, the deflection circuit effectively maps arrival time to space. The electrons are finally multiplied in a multi-channel-plate, and detected on a phosphorus screen which is imaged into a CCD camera. Potential noise sources are thermionic emission from the photocathode, unwanted electronic emission events from the multi channel plate, CCD readout noise and CCD thermal noise. The few numbers in the literature suggest that the dominating noise source is actually thermionic emission, which is purely additive [117] and immediately causes a problem. While the thermionic emission is not tied at all to the wavelength of the detected light and therefore constant, the cathode's quantum efficiency does strongly depend on wavelength. For the commonly used NaKSbCs cathode material, also commonly referred to as "S-20", the dark count rate from thermionic emission alone is roughly 500 counts per second (assuming a 5 mm-diameter cathode) [118], while the quantum efficiency at 900 nm (the band gap of GaAs, a commonly used benchmark in semiconductor emission detection) is as low as 0.1 %[114, 110, 116]. This implies that a SNR of 1 can only be achieved with impinging photon rates of over 500,000/s. This makes experiments on the single photon level very difficult. The streak camera used in the experiment is equipped with a AgOCs (known as "S-1") cathode with a response of only 1 mA/W over a large wavelength region ranging from visible to near-infrared. However, using upconversion, one would be able to use the S-20's response of 40 mA/W at 500 nm.

In the present experiment, the PDC source was pumped with a pump pulse energy of 120 pJ, resulting in an average photon number of 0.2 per pulse. The photons are then converted using the previously used QPG waveguide, pumped at 854 nm. The converted light at 550 nm is then detected using a Hamamatsu C5680 streak camera. The device is equipped with a S-1 photo cathode and Peltier-cooled ORCA-ER CCD camera. The cathode's response is specified to 1 mA/W at 550 nm, and below $10^{-3}$ mA/W at 1550 nm, i.e. basically not even specified in the data sheets [110], which would make a measurement directly at 1550 nm impossible due to insufficient SNR. The deflection circuit was operated in so-called synchro-scan mode, where the deflection voltage is synchronized to the laser repetition rate of 80,165 MHz. The laser repetition rate fluctuated during measurement due to automatic adjustment of the laser cavity, but the streak camera's delay generator was able to keep the lock and no drifts of the signal timing were observed.

### 4.2.2. Results

The measurement was performed using analog integration. In this mode, the camera shutter is left open for a long time compared to laser repetition rate

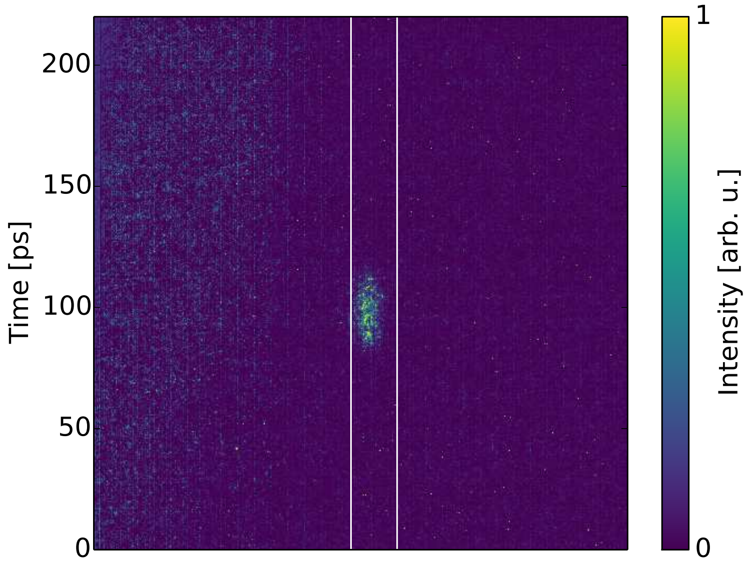

Figure 4.4.: Streak camera image for the upconverted PDC photon, obtained by analog integration over 32 exposures with 10 seconds exposure time each. The white lines indicate the integration boundaries used to obtain the temporal profile. The horizontal axis covers merely the spatial degree of freedom and carries no physical information in this measurement scenario.

and phosphorus response. The integration was performed over 32 exposures of 10 seconds each, the maximum exposure time allowed by the CCD camera. Longer exposure would be preferable, since it reduces the effect of readout noise, but would not impact the effect of cathode noise. To leave the cathode noise at a bearable level, the multi channel plate gain was set to only 80 % of the maximum level. The recorded background-subtracted image is shown in Figure 4.4. This image is quite remarkable, since thin vertical lines, hot-spots where the readout leads are positioned within the CCD, have similar signal level to the recorded signal. The raw images for the recorded PDC signal, the background and the calibration image used to assess the temporal resolution are discussed in appendix C.

From this image, a temporal intensity profile was extracted by integrating over columns between the white lines. This profile is shown in Figure 4.5. Error bars represent the standard deviation within 5 ps windows, which is comparable to the streak camera's temporal resolution of 7.5 ps. This profile allows to extract the pulse duration, which is 22.6±0.5 ps.

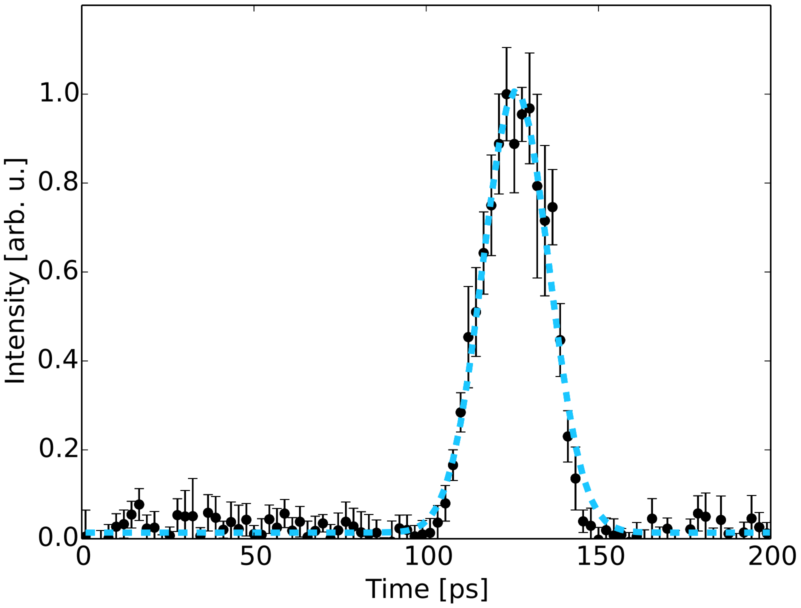

Figure 4.5.: Integrated temporal profile of the upconverted PDC photon obtained from the streak camera image in Figure 4.2. Error bars were calculated using the standard deviation around the averaged counts in 5 ps bins. The blue dashed line indicates a Gaussian fit used to obtain the temporal duration.

**Alignment procedure**

Again, the alignment of this experiment is most similar to the one for bandwidth compression presented in section 3.3. This is true for the alignment and initial characterization of the PDC source and QPG. The only notable difference is that there are no fiber couplings used, the streak camera is free-space coupled. This complicates things regarding background suppression, since stray light and unwanted wavelength and polarization components couple easier than in SM fibers.

Key to good resolution and SNR in the streak camera is background suppression and small waist size on the photocathode.

For background subtraction, there are several necessary steps. First, stray light is suppressed using a black cardboard box for shielding the input hole. Second, spectral suppression is achieved using the same 4f filter for the green light used in the previous experiments. Then, a additional narrow bandpass filter is added inside the cardboard box. In a last step, add a Glan-Thompson polarizer into the beam path to suppress any light that is orthogonally polarized to the green converted light.

Achieving a small beam waist at the focus on the photocathode is tricky given the possibly unmatched input optics and the beam profile coming out of the waveguide. Add an additional telescope to adjust beam waist and divergence in front the actual incoupling optics.

Note that streak cameras are extremely sensitive and can very well be damaged by a too bright input. Keep the lab dark at all times when the shutter is open. Start with attenuated bright light and the electron multiplier turned off, open the input slit slowly. If there is nothing observed, first check and adjust incoupling. It is wise to first increase the MCP gain before increasing brightness.

### 4.2.3. The “right” and the “wrong” nonlinear process

The successful measurement of the temporal envelope - or rather *some* temporal envelope - shows, that the upconversion technique solves the issues with streak camera imaging of weak infrared light. However, the measured profile has to be closely examined to judge the quality of the imaged temporal profile. Therefore, it is necessary to examine the influence of the frequency conversion implemented in the QPG. Fortunately, formulas for the output temporal pulse shape $s(t)$ of SFG is readily available in the literature [119]:

$$\begin{aligned} s(t) \propto \int d\omega e^{j\omega t} \int d\omega_2 F_1(\omega - \omega_2) F_2(\omega_2) \\ \times e^{-j\omega_2 \tau} e^{j(\Delta k + \alpha\omega)L/2} \times \operatorname{sinc}\left( (\Delta k + \alpha\omega)\frac{L}{2} \right) \end{aligned} \tag{4.6}$$

where $\alpha = \dot{k}_s - \dot{k}_1$ denotes mismatch between inverse group velocities of output and input, $\Delta k$ again denotes the corresponding phase-mismatch, $F_1(\omega)$ and $F_2(\omega)$ are the spectral intensities of input and pump with respect to angular frequencies, respectively, and $L$ is the effective crystal length, i.e. the length of the periodically poled region (outside of which there is no phasematching). Since phasemismatch and group velocities are known in the QPG to be $\dot{k}_1 - \dot{k}_2 = 0$, and we can neglect dispersion since the phasematching function is sufficiently flat, i.e. the curvature is small compared to its bandwidth, the equation simplifies significantly:

$$\begin{aligned} s(t) = FT\left( \int d\omega_2 F_1(\omega - \omega_2) F_2(\omega_2) \right) \\ * FT\left( \operatorname{sinc}\left( (\Delta k + \alpha\omega)\frac{L}{2} \right) \right) \end{aligned} \tag{4.7}$$

where the Fourier transform of a product of functions has been rewritten as the convolution of individual Fourier transforms. For the crystal length of 27 mm, and a input bandwidth of 7 nm, it becomes apparent that the two contributions to $s(t)$ have drastically different time scales. The phasematching contribution with the given crystal length results in a box shaped pulse profile of 27 ps length. The pulse duration before conversion is only 1 ps (characterized using the cross correlation measurement presented before in chapter 3.4), which means that the first contribution dominates the output pulse profile. Even faithful deconvolution, challenging in general, may be very difficult here, since the phase of the phasematching function is not known. It can be concluded, that there is only significant information about the input pulse in the process' output pulse profile, if the input pulse is sufficiently long, at least as long as the pulse walk-off of 27 ps.

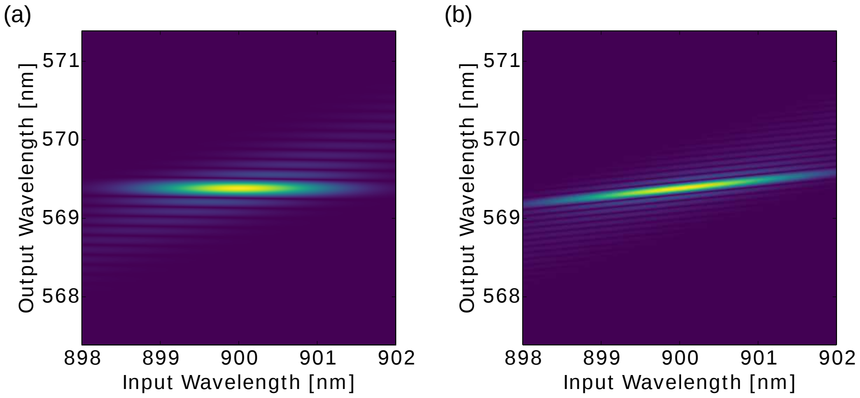

Figure 4.6.: a) Spectral transfer function of the upconversion process employed in this work. b) Spectral transfer function of the proposed up-frequency generation process.

Off course, this reshaping has no effect on the overall improvement of detection efficiency. With at least 3 orders of magnitude higher spectral response at the output wavelength, and the external conversion efficiency of 27.1 % [47], the overall improvement is at least a factor of 250. Employing a photocathode optimized for detection at 550 nm (The S-1 is mostly used because of its comparably wide detection window, and decent efficiency in the near infrared spectrum), e.g. a S-20 cathode, another 2 orders of magnitude can be gained. In conclusion, even a frequency conversion process with small external conversion efficiency of the order of 1 % yields a drastic overall improvement.

Still, the goal of upconversion detection in the time domain is not to perform click detection, where the temporal profile does not matter, but to actually measure the input photon's temporal (intensity) profile. Therefore, one would prefer a nonlinear process that preserves the pulse shape. From what is known about the QPG one can already see that its nonlinear process is not suited to preserve the pulse, since the modal decomposition of the transfer function yields a single mode. Single mode transfer functions are equivalent to having a decorrelated transfer function with no spectral (and therefore temporal) correlations between input and output fields. However, strong correlations are necessary to faithfully and blindly convert arbitrary pulse shapes. Even slight modification of the employed process shows immediately what can be possible in Lithium Niobate. The numerical transfer functions of the QPG process as well as a type-0 process with the same wavelength combination are shown in Figure 4.6.

While the QPG's transfer function is flat and therefore images all spectra within the spectral aperture onto basically the same output spectrum, the non-zero angle in the type-0 transfer function constitutes a direct mapping. The spectrum is merely compressed (which corresponds to a stretching in the time domain), where the phasematching bandwidth corresponds to a finite temporal resolution of the mapping. The next chapter will contain a more thorough analysis, where these parameters are properly defined and quantified.

### 4.2.4. Shaping the transfer function

As mentioned before, the functionality of a time domain upconversion device has to be judged by its temporal transfer function $\hat{\Psi}(\tau_s, \tau_i)$. In the following, an analytical study will be presented on how the key parameters like resolution, magnification and apertures relate to the physical properties of the nonlinear process, namely phasematching angle, pump and phasematching bandwidth. For this, the transfer function shall be approximated using a double Gaussian, i.e. both the pump pulse spectrum and the phasematching function will be rotated two-dimensional Gaussian functions. Both those Gaussians take the form

$$\Phi_i(x, y) = \exp\left(-\left(\frac{\cos^2\varphi_i}{2\sigma_i^2}x^2 - \frac{2\sin 2\varphi_i}{4\sigma_i^2}xy + \frac{\sin^2\varphi_i}{2\sigma_i^2}y^2\right)\right) \tag{4.8}$$

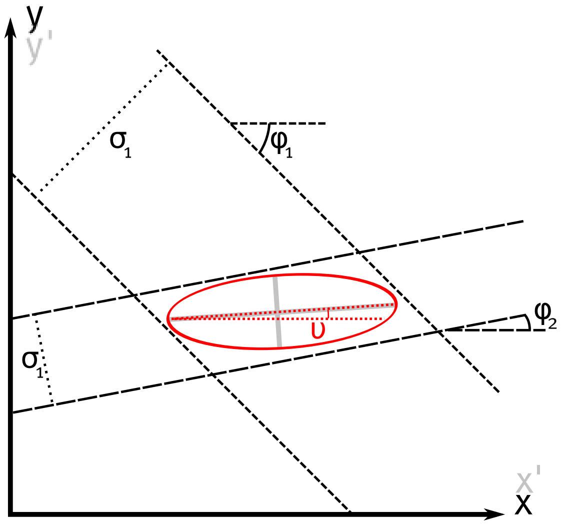

Figure 4.7.: Definition of angles and coordinate systems for the rotated description of the double Gaussian transfer function

where the index $i$ denotes the two functions for phasematching and pump. These two multiplied together describe the spectral transfer function. However, the pump function is oriented at $\varphi_P = 45°$, and the phasematching at the phasematching angle $\varphi_{PM} = \alpha$. The goal now is to find a description as a double Gaussian with perpendicular axes, i.e. one that is described in the coordinate system of the ellipse axes. In general, any rotated two-dimensional Gaussian has terms associated with the two axes (see $x^2$ and $y^2$-terms above), and also cross-terms. In the correct coordinate system that aligns with the ellipse axes, these cross terms have to vanish. Thus, the first step is to perform a general coordinate transformation by rotating by an angle $\nu$:

$$x = x' \cos\nu - y' \sin\nu \tag{4.9}$$

$$y = x' \sin\nu + y' \cos\nu \tag{4.10}$$

It is straight forwards to see that this is a counter-clockwise rotation. Substituting into equation 4.8, only writing down the summands of the exponent and denoting the new coordinate system with x,y:

$$\begin{aligned} -\ln\left(\Phi_i(x,y)\right) = & \frac{\cos^2\varphi_i}{2\sigma_i^2}(x\cos\nu + y\sin\nu)^2 \\ & - \frac{2\sin 2\varphi_i}{4\sigma_i^2}(x\cos\nu + y\sin\nu)(-x\sin\nu + y\cos\nu) \\ & + \frac{\sin^2\varphi_i}{2\sigma_i^2}(-x\sin\nu + y\cos\nu)^2 \end{aligned} \tag{4.11}$$

We now multiply pump and phasematching in the following fashion:

$$\Psi(x,y) = \Phi_1 \cdot \Phi_2 \tag{4.12}$$

which results in the exponents being added, meaning that all of the above terms appear twice, one for pump and phasematching each. Is is straight forward to see that we end up with cross terms, four in total. We write those down using the following definitions:

$$\mathrm{I} \quad \left(\frac{\cos^2\varphi_1}{\sigma_1^2} + \frac{\cos^2\varphi_2}{\sigma_2^2}\right)\cos\nu\sin\nu\cdot xy \quad \equiv \quad \alpha\cos\nu\sin\nu\cdot xy \tag{4.13}$$

$$\mathrm{II} \quad \left(\frac{\sin 2\varphi_1}{2\sigma_1^2} + \frac{\sin 2\varphi_2}{2\sigma_2^2}\right)\sin^2\nu\cdot xy \quad \equiv \quad \beta\sin^2\nu\cdot xy \tag{4.14}$$

$$\mathrm{III} \quad -\left(\frac{\sin 2\varphi_1}{2\sigma_1^2} + \frac{\sin 2\varphi_2}{2\sigma_2^2}\right)\cos^2\nu\cdot xy \quad \equiv \quad -\beta\cos^2\nu\cdot xy \tag{4.15}$$

$$\mathrm{IV} \quad -\left(\frac{\sin^2\varphi_1}{\sigma_1^2} + \frac{\sin^2\varphi_2}{\sigma_2^2}\right)\sin\nu\cos\nu\cdot xy \quad \equiv \quad \gamma\cos\nu\sin\nu\cdot xy \tag{4.16}$$

As mentioned before, we now require these cross terms to cancel out, since a two-dimensional Gaussian, where the two components align with the axes of the coordinate system, does not have cross terms. Hence one can write:

$$(\alpha+\gamma)\sin\nu\cos\nu+\beta(\sin^2\nu-\cos^2\nu)=0 \tag{4.17}$$

$$\frac{\alpha+\gamma}{2}\sin(2\nu)-\beta\cos(2\nu)=0 \tag{4.18}$$

$$\frac{2\beta}{\alpha+\gamma}=\frac{\sin(2\nu)}{\cos(2\nu)} \tag{4.19}$$

$$\tan(2\nu)=\frac{2\beta}{\alpha+\gamma} \tag{4.20}$$

We expand this result again:

$$\tan(2\nu)=\frac{\frac{\sin 2\varphi_1}{\sigma_1^2}+\frac{\sin 2\varphi_2}{\sigma_2^2}}{\frac{\cos^2\varphi_1}{\sigma_1^2}+\frac{\cos^2\varphi_2}{\sigma_2^2}-\frac{\sin^2\varphi_1}{\sigma_1^2}-\frac{\sin^2\varphi_2}{\sigma_2^2}}=\frac{\frac{\sin 2\varphi_1}{\sigma_1^2}+\frac{\sin 2\varphi_2}{\sigma_2^2}}{\frac{\cos 2\varphi_1}{\sigma_1^2}+\frac{\cos 2\varphi_2}{\sigma_2^2}} \tag{4.21}$$

To obtain the description of the ellipse in this new coordinate system, substitute $\nu$ into $\Psi(x,y)$:

$$\begin{aligned}-\ln(\Psi(x,y))=&\left(\frac{\cos^2\varphi_1}{2\sigma_1^2}+\frac{\cos^2\varphi_2}{2\sigma_2^2}\right)(x^2\cos^2\nu+y^2\sin^2\nu)\\&-\left(\frac{\sin 2\varphi_1}{2\sigma_1^2}+\frac{\sin 2\varphi_2}{2\sigma_2^2}\right)(x^2\sin\nu\cos\nu-y^2\sin\nu\cos\nu)\\&+\left(\frac{\sin^2\varphi_1}{2\sigma_1^2}+\frac{\sin^2\varphi_2}{2\sigma_2^2}\right)(x^2\sin^2\nu+y^2\cos^2\nu)\end{aligned} \tag{4.22}$$

One can observe that this is a quadratic equation, and using the identity $\sin 2x=2\sin x\cos x$ on the second term, we arrive at

$$\begin{aligned}-\ln(\Psi(x,y))=&\frac{1}{2}\left[\left(\left(\frac{\cos\varphi_1\cos\nu}{\sigma_1}-\frac{\sin\varphi_1\sin\nu}{\sigma_1}\right)^2+\left(\frac{\cos\varphi_2\cos\nu}{\sigma_2}-\frac{\sin\varphi_2\sin\nu}{\sigma_2}\right)^2\right)x^2\right.\\&\left.+\left(\left(\frac{\cos\varphi_1\sin\nu}{\sigma_1}+\frac{\sin\varphi_1\cos\nu}{\sigma_1}\right)^2+\left(\frac{\cos\varphi_2\sin\nu}{\sigma_2}+\frac{\sin\varphi_2\cos\nu}{\sigma_2}\right)^2\right)y^2\right]\end{aligned} \tag{4.23}$$

From this we can read the standard deviations along the two axis:

$$\sigma_1' = \sqrt{\left(\frac{\cos\varphi_1\cos\nu}{\sigma_1} - \frac{\sin\varphi_1\sin\nu}{\sigma_1}\right)^2 + \left(\frac{\cos\varphi_2\cos\nu}{\sigma_2} - \frac{\sin\varphi_2\sin\nu}{\sigma_2}\right)^2}^{-1} \tag{4.24}$$

$$\sigma_2' = \sqrt{\left(\frac{\cos\varphi_1\sin\nu}{\sigma_1} + \frac{\sin\varphi_1\cos\nu}{\sigma_1}\right)^2 + \left(\frac{\cos\varphi_2\sin\nu}{\sigma_2} + \frac{\sin\varphi_2\cos\nu}{\sigma_2}\right)^2}^{-1} \tag{4.25}$$

With the rotation angle $\nu$ and the two width parameters $\sigma_{1,2}$, whichever is smaller, the imaging parameters resolution, PSF and magnification are fully described through the physical parameters $\varphi_1 = \alpha$ and the phasematching and pump bandwidths $\sigma_{1,2}$. Before these relations are analyzed further, there are a couple of interesting cases to consider. First, let's assume one of the widths, pump or phasematching bandwidth, is much larger than the other. For example, this is the case for a CW-pumped process in a short crystal, where the phasematching is fairly wide, i.e. $\sigma_1 >> \sigma_2$. The smaller feature will then dominate the ellipse angle.

$$\tan 2\nu = \frac{\frac{\sigma_2^2\sin 2\varphi_1}{\sigma_1^2} + \sin 2\varphi_2}{\frac{\sigma_2^2\cos 2\varphi_1}{\sigma 1^2} + \cos 2\varphi_2} = \tan 2\varphi_2 \tag{4.26}$$

$$\iff \quad \nu = \varphi_2 \tag{4.27}$$

Same goes for the opposite case, $\sigma_2 >> \sigma_1$. Next, equal bandwidths for pump and phasematching $\sigma_1 = \sigma_2$ will create a ellipse, where the angle $\nu$ is exactly in between the pump and phasematching angle:

$$\tan 2\nu = \frac{\sin 2\varphi_1 + \sin 2\varphi_2}{\cos 2\varphi_1 + \cos 2\varphi_2} = \frac{2\sin(\varphi_1+\varphi_2)\cos(\varphi_1-\varphi_2)}{2\cos(\varphi_1+\varphi_2)\cos(\varphi_1-\varphi_2)} = \tan(\varphi_1+\varphi_2) \tag{4.28}$$

$$\iff \quad \nu = \frac{\varphi_1+\varphi_2}{2} \tag{4.29}$$

So for equal pump and phasematching bandwidth, the angle of the transfer ellipse is the average angle of the two. Last, there is an interesting case for dispersion engineering, especially for tailoring PDC sources. To design a singlemode source (assuming a gaussian phasematching), the phasematching is not required to be at $\varphi_1 = 45°$, it merely has to cut through the quadrants opposite to the pump, which is (for PDC) always at $\varphi_2 = -45° = 135°$:

$$\tan\phi_1 > 0; \quad \tan\varphi_2 = -1 \tag{4.30}$$

Within those constraints, there exists a combination of bandwidths $\sigma_1/\sigma_2$ for which the transfer function decomposes into a single mode, or in other words:

$$\nu = n \cdot \frac{\pi}{2}; \quad n \in \mathbb{N} \tag{4.31}$$

which implies that the ellipse aligns with the axis of the coordinate system, i.e. $\nu \in \{0°, 90°, 180°, 270°\}$. This results in $\tan 2\nu = 0$:

$$0 = \frac{\frac{\sin 2\varphi_1}{\sigma_1^2} + \frac{\sin(-2\cdot 45°)}{\sigma_2^2}}{\frac{\cos 2\varphi_1}{\sigma_1^2} + \frac{\cos(-2\cdot 45°)}{\sigma_2^2}} = \frac{\sin 2\varphi_1 - \frac{\sigma_1^2}{\sigma_2^2}}{\cos 2\varphi_2} \tag{4.32}$$

$$\iff \quad \varphi_1 = \frac{1}{2}\arcsin\frac{\sigma_1^2}{\sigma_2^2} \tag{4.33}$$

For DFG, the angle is the same as for PDC, since PDC is essentially a degenerate DFG. For SFG and SHG this only changes slightly since $\varphi_2 = 45° = 225°$.

The next step is to visualize these relations for arbitrary phasematching angle and pump bandwidth. Here, the phasematching bandwidth, set by the crystal length, is held constant, since it cannot be changed on the fly. On the other hand, the phasematching angle can be influenced by changing the wavelengths involved, and the pump bandwidth can be shaped at will. Figure 4.8 shows the resulting parameters.

The plotted phasematching angles range from 0 to 180°, since the the transfer function is point-symmetric. There are several interesting features in the plotted parameters. For the magnification, small pump bandwidths, i.e. narrowband or cw light, $M$ goes to -1, implying a phasematching angle of 45°, dictated by the pump angle. For large pump bandwidths the magnification becomes independent of pump bandwidth and is only defined by the phasematching angle. Another interesting feature is in the right half of the plot: There is a $U$-shaped line that has magnification of 0, and then jumps to a $\pm\infty$ line, which corresponds to ellipse angles of 0 or infinite magnification, respectively. At the transition, at an angle of 135° and equal bandwidths, the magnification is undefined and the transfer function is perfectly symmetric.

Another interesting feature shows up for resolution and PSF. For a phasematching angle of $45°$, when it coincides with the pump, the resolution and and

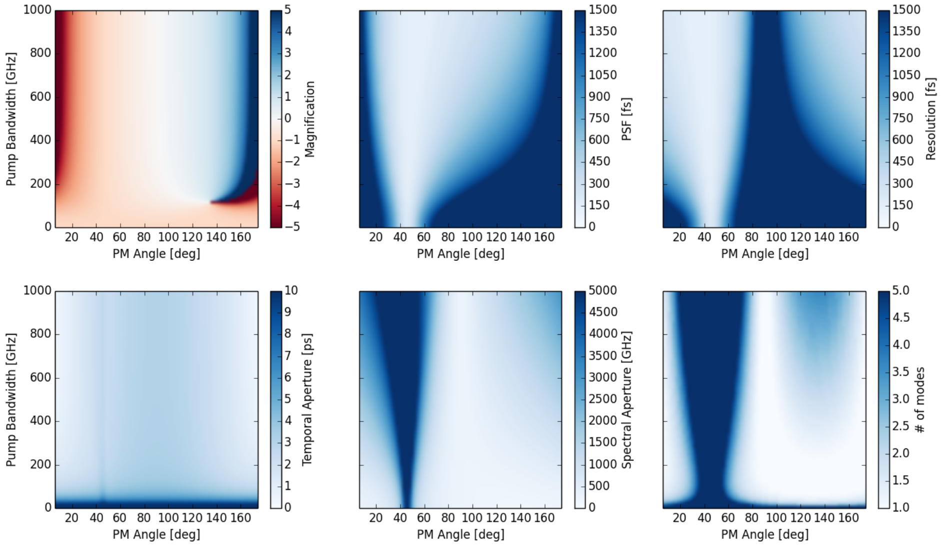

Figure 4.8.: Magnification, resolution, point spread function, apertures and pulse complexity for a phasematching bandwidth of 120 GHz

PSF go to zero, i.e. the imaging becomes perfect. The reason for this is that the spectral transfer function becomes infinite in one direction, and thus the temporal transfer function becomes infinitely narrow. Of course this cannot be the case in a real process, because of second order dispersion, which causes a curvature of the phasematching function. Still, for perfectly preserving a pulse shape, this is the optical phasematching angle.

The aperture functions give a measure of how wide a pulse may be in the spectral and temporal domain before it gets cut by the limited width of the transfer functions in spectral and time domain. The mode number plotted in the last panel is a more interesting parameter. If one would do a modal decomposition of the transfer function, a high number of involved modes is desirable, as it can describe a more complex pulse. This value is analog to the ratio between resolution and temporal aperture. A single mode transfer function is the equivalent of equal resolution and aperture. i.e. a Gaussian pulse of appropriate duration is perfectly imaged, but no other pulse shape can be imaged faithfully. Again, this parameter is best for phasematching angles around 45°.

### 4.2.5. Revisiting dispersive properties of common nonlinear materials

To achieve a good mapping at useful magnification and resolution, while being able to faithfully convert complex pulse shapes, it seems advantageous to have a phasematching angle not too different from 45°, and sufficiently far away from 0° or 90°. At the same time, magnification can only be harnessed for narrow phasematching, i.e. long crystals, in combination with broadband pump pulses. If such pulses are not available and the pump has to be cw, a short crystal is preferable. In other words, the best combinations of parameters are in the left half of the above parameter spaces, and at the very top or bottom edges. The corresponding phasematching angles luckily correspond to no *particular* group velocity matching like one finds in the QPG configuration. For the wavelength order $\lambda_p > \lambda_s > \lambda_i$, the phasematching angles for most materials that show normal dispersion, i.e. $dn/d\lambda < 0$, are between 0° or 90°. The group-velocity curves are shown again Figure 4.9. A phasematching angle of 45° corresponds to symmetric group velocity matching:

$$v_{G,p} - v_{G,s} = v_{G,s} - v_{G,i} \tag{4.34}$$

All types of processes could in principle provide such group velocity relations, but only for specific wavelength combinations, which are usually at least partially fixed by the application and available lasers. A typical measurement scenario in semiconductor characterization would be upconversion from $\lambda_S = 900\,\mathrm{nm}$ (the band gap of GaAs), pumped with a telecom laser or OPO system in the infrared, e.g. $\lambda_P = 1600\,\mathrm{nm}$. Angles of roughly 20° can be achieved in all three materials with type-0 processes, where Lithium Niobate would be favorable because of the larger nonlinear tensor element. Type-I processes in KTP or LN are also useful, with slightly steeper phasematching angles, however, at the expense of efficiency. Since the difference in phasematching angle is not significant, Lithium Niobate is chosen for the process.

But first, let's revisit the QPG process to show how useful it can be exactly for this application, and under what circumstances any information can be gained from the measurement setup presented as a proof-of-principle experiment.

We therefore examine the actual material dispersion data for Lithium Niobate. For the QPG process, the above parameters were recalculated and are displayed in Figure 4.10. The phasematching angle as a free parameter has now been replaces by pump wavelength, since this is the only parameter that influences the phasematching angle and is actually accessible in the lab without producing a new crystal. What can be seen is that for large pump bandwidth, the magnification is $\pm\infty$, with very large PSF and very low pulse complexity. Basically, this is a very bad situation to image and preserve a pulse shape. This analysis confirms the observations made using equation 4.6.

Since a type-0 process was proposed, let's examine the situation for this one as well. The calculated parameters are plotted in Figure 4.11.

First, it can be seen that all parameters lie in a much more mellow range. We observe neither extreme magnification, apertures or single-modeness, and in contrast to the QPG process, the parameters are fairly constant over a wide range of pump wavelengths. Again, the optimal parameters lie in the top part of the plots, where the pump bandwidth, here as high as 1 THz, are much larger

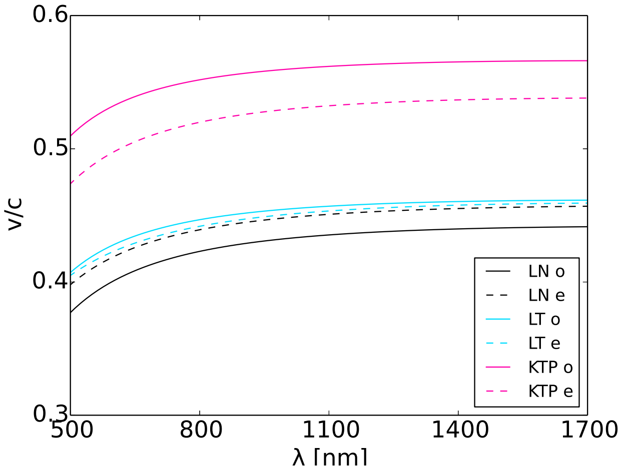

Figure 4.9.: Group velocities of $LiNbO_3$, KTP and $LiTaO_3$.

than the phasematching bandwidth. In this regime, both PSF and Resolution lie in the range lie in the range of 1 ps, with a temporal aperture of the order of several picoseconds, allowing for sufficient pulse complexity to characterize even non-Gaussian pulse shapes. Most interestingly, the magnification lies between 2 and 3. With a PSF of about 1 ps - less than the resolution of the previously employed streak camera, 5 ps - the converter presents an actual improvement of temporal resolution by a factor of 2.

## 4.3. Conversion efficiency of waveguides nonlinear processes

One of the key parameters in upconversion detection, employing time-resolved detection or otherwise, is conversion efficiency, since the main goal of the method is to achieve an overall system efficiency greater than the detection efficiency available at the fundamental wavelength. This has been described in equation 4.1. It is therefore tantamount for developing upconversion detectors to assess their conversion efficiency. The efficiency will be calculated numerically.

### 4.3.1. Numerical calculation

The numerical algorithm employed here solves the classical coupled field equations for all three fields. The fields are described inside the waveguides, using effective Sellmeier equations for the guided modes in order to describe the waveguide's actual dispersion and phasematching properties as accurate as possible. The coupled wave equations are then solved using a split-step

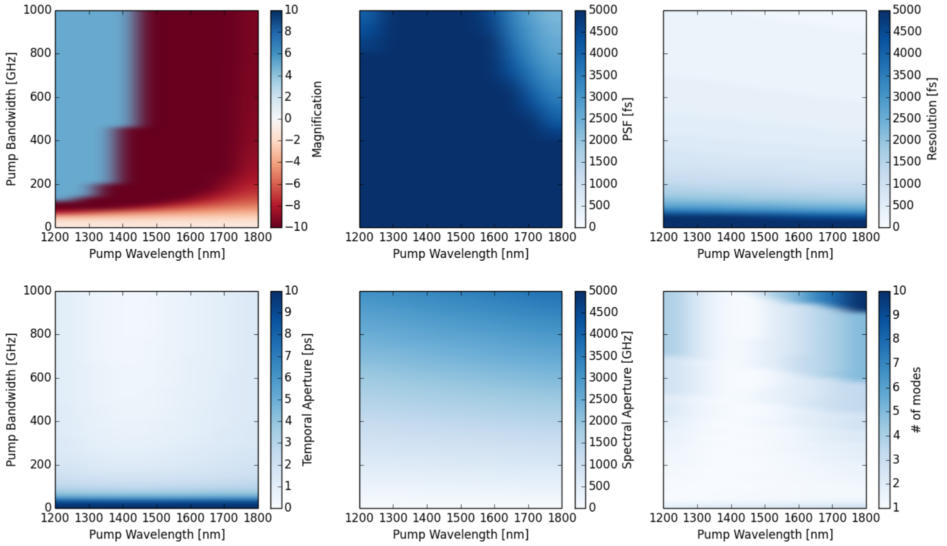

Figure 4.10.: Magnification, resolution, point spread function, apertures and pulse complexity for the QPG process in a 20mm-long Lithium Niobate waveguide

Fourier method (SSFM). This method is a well established approach to nonlinear wave propagation [120, 121]. The term ”split step“ refers to the splitting of each propagation step into two half steps, where the linear evolution of the fields by applying a phase term corresponding to linear propagation to each field, and one nonlinear step, where the coupling between the fields is calculated. For the nonlinear step, a Cash-Karp [122] method is employed. The Cash-Karp algorithm solves sets of differential equations using a Runge-Kutta method [123], but calculates the appropriate step size by comparing the results for different orders of the Runge-Kutta method. The algorithm, implemented in *python*, calculates not only intensity, but also the pulse shapes of the fields, thus allowing to judge both conversion efficiency and quality, i.e. distortion of the fields.

First, the proposed type-0 process in Lithium Niobate waveguides is investigated. From the general imaging parameter study presented before, the optimal pump scheme is to use broadband pulses. A bandwidth of 1 THz, typical for many commercially available laser systems, was chosen for the numerical calculation. Figure 4.12 shows the resulting conversion efficiency for 10 mm, 20 mm, and 40 mm long waveguides. It becomes apparent, that the conversion efficiency that can be reached with reasonable pump pulse energies (1 nJ or pump pulse energy corresponds to 80 mW average power in the Ti:Sapphire laser system used throughout this thesis) is limited, and the maximum value depends on the waveguide length. In the light of the drastic difference in de-

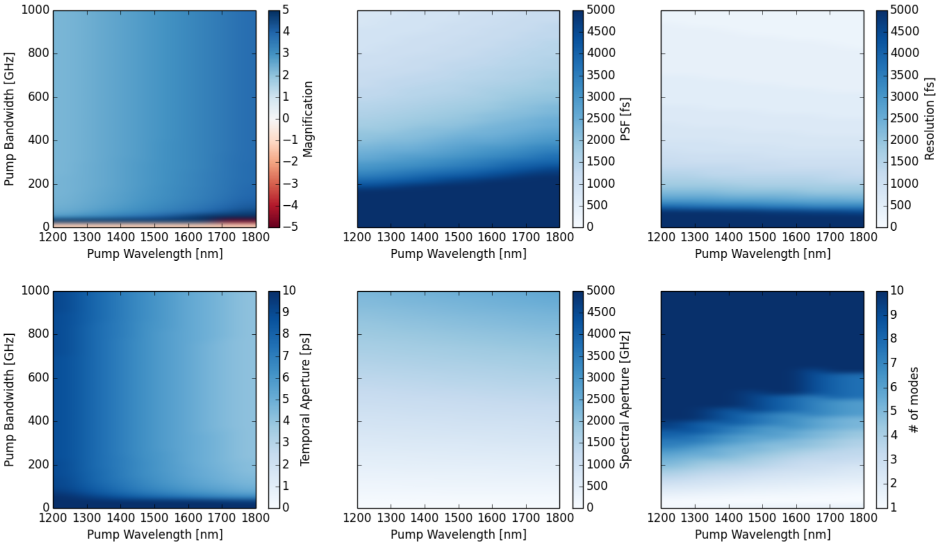

Figure 4.11.: Magnification, resolution, point spread function, apertures and pulse complexity for a type-0 process in a 40mm-long Lithium Niobate waveguide

tection efficiency for streak camera photocathodes this is more than sufficient to facilitate an overall improvement of several orders of magnitude.

Figure 4.13 shows the conversion efficiency for the same process, but pumped with quasi-CW light in the form of nanosecond pulses, where the average power during the pulse is given as a measure of pump intensity. Due to the much smaller pulse energy and temporal overlap, the conversion efficiency is visibly reduced to the order of 1 %. This is still sufficient to facilitate a useful upconversion streak camera. Moreover, the conversion efficiency is still in a linear regime, and not saturated yet. It is notable that pump powers of over 1 W are not advisable, since even small pieces of dust or other impurities can cause the waveguide facet to get burnt.

The linear regime here is highly desirable. The reason lies in the fact that the pulses get distorted in the limit of high conversion efficiency. This is visualized in the three plots shown in Figure 4.14. The temporal pulse shape of the idler mode at the output is shown for three different pump pulse energies. At 0.2 nJ, the idler mode looks as it should (gaussian profile). At 0.5 nJ, the onset of distortion can already be seen in the left shoulder of the pulse. At 1 nJ, a side peak is strongly visible, with the phase profile being scrambled. When compared with Figure 4.12, it can be seen that the value of 0.5 nJ for the 40 mm long waveguides places the conversion efficiency already in the saturation regime. This shows, that in this regime, the pulse gets back-converted, starting with the front of the pulse, which had been converted first. Hence, to preserve the pulse shape, it is advisable to limit the conversion efficiency to

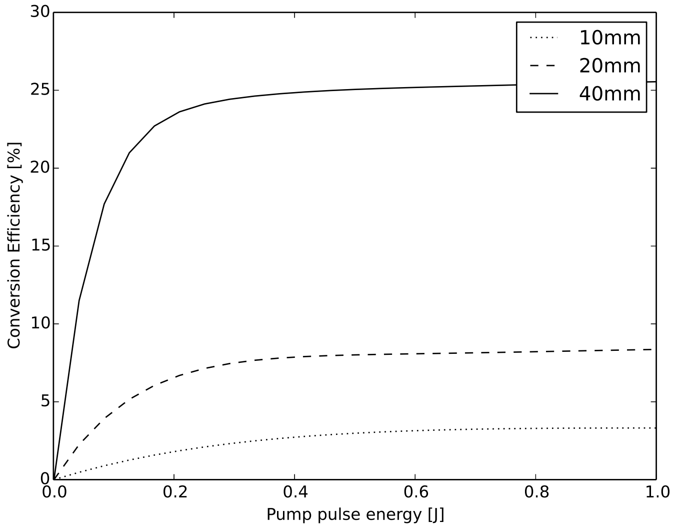

Figure 4.12.: Conversion efficiency of the type-0 upconverter as a function of pump pulse energy. Pump pulse bandwidth is 1 THz or 8 nm at the pump wavelength of 1700 nm.

the non-saturated regime.

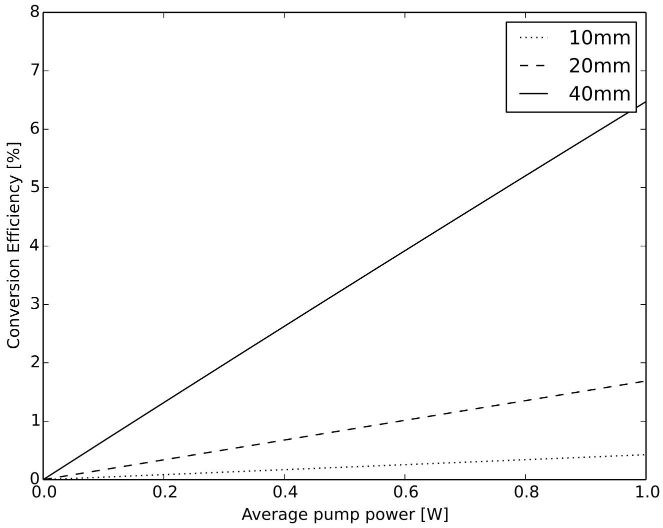

Figure 4.13.: Conversion efficiency of the type-0 upconverter as a function of average pump power in the case of a quasi-CW pump at a wavelength of 1700 nm.

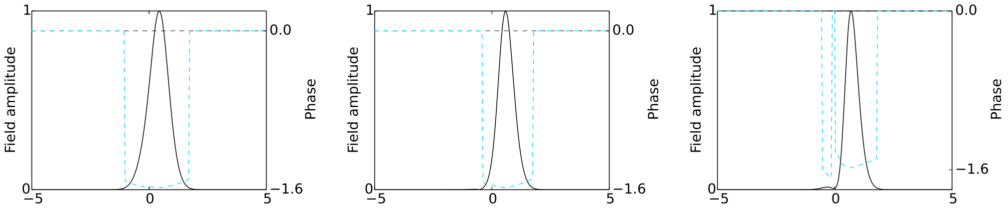

Figure 4.14.: Idler field temporal pulse shape at three different pump pulse energies of 0.2, 0.5 and 1 nJ for the pulsed pump type-0 process. Solid lines correspond to field amplitude, dashed black lines to input phase, and dashed turquoise lines to output phase.

### 4.3.2. Performance of the final upconverter

To see how well such an upconversion detection system performs with these efficiencies, it is useful to look at an example. In general, the responses $N_{kt}$ of photocathodes, specified as electric current per optical power, can be easily converted into quantum efficiency:

$$N_{kt}\,\left[\frac{A}{W}\right] = N_{kt}\,\left[\frac{C}{J}\right] = \eta\frac{e\lambda}{hc_0} \tag{4.35}$$

where $e$ is the charge of an electron, $h$ is Planck's constant, $c_0$ the vacuum speed of light, $\lambda$ is the wavelength of the impinging light, and finally $\eta$ is the quantum efficiency. The following values for the cathode response can be found in [114].

Light at 900 nm is usually detected using an S-1 cathode with a photocurrent of about 2 mA/W, which corresponds to a quantum efficiency of 0.28 %. When converted to 590 nm, the efficient S-20 material can be used, which responds with about 60 mA/W at that wavelength, corresponding to a quantum efficiency of 12.8 %. This is an improvement by a factor of 46. Off course this assumes that one has access to both cathodes in the first place. If an S-20 cathode is used at 900 nm as well, where its quantum efficiency is merely 0.07 %, the improvement is by a factor of roughly 183.

According to equation 4.1, the minimum conversion efficiency necessary to achieve an improvement through the upconversion technique is 2.2 % for the use of the optimal cathode material for every wavelength, or 0.5 % when only the S-20 material is used. These values are surpassed at least in the 40 mm long waveguide for CW pumping (extraordinary pump powers are needed in shorter crystals). For broadband pump pulses, the necessary efficiency is easily reached within the linear regime in waveguides as short as 20 mm. Any additional linear losses in the setup have to be accounted for as well and depend on the actual setup.

With these final parameters set, samples were produced. Depending on desired efficiency and resolution, three lengths of 10 mm, 20 mm and 40 mm were chosen. Polarization along the Lithium Niobate crystal's extraordinary axis has been chosen, because a matching photomask to produce the poling period of roughly 9 $\mu$m was already available. Using ordinary polarization instead would make no difference, since losses are comparable and the nonlinear coefficient is identical. The samples were then finished by applying anti-reflective optical coatings for all three involved wavelengths: The input (signal) is intended to be between 900 and 1000 nm, with the pump spectrum centered at around 1700 nm. The output (idler) is therefore at roughly 600 nm. The finished samples are ready to be set up at the TU Dortmund to be used in upconversion detection experiments on semiconductor quantum dot laser emission.

# CHAPTER 5

# CONCLUSION

In this thesis, many concepts of nonlinear optics have been revisited from the perspective of dispersion engineering. The goal of this was to formulate a systematic approach to tailoring nonlinear devices.

In chapter 2, the necessary concepts from nonlinear optics were introduced. As the most important material property, the nonlinear susceptibility matrix was discussed with the aim of establishing which nonlinear processes work in a certain material and how efficient they can be. Dispersion and birefringence were discussed as a means of altering group-velocity matching and spectral correlations. Finally, the approximations necessary to describe quantum frequency conversion with the classical transfer function have been introduced. This concept is simple, but yet very successful, since the approach allowed to realize a variety of functional devices, which were presented in later chapters.

In the following third chapter, a particular nonlinear process was discussed. The *Quantum Pulse Gate* process, developed by the author's predecessors, uses a particular combination of wavelengths and polarizations to achieve group-velocity matching of different fields. The process was revisited with the aim of establishing a systematic connection between the spectral and temporal correlations required for its applications, and design parameters such as crystal length and wavelengths. Since several applications may possess identical requirements for a nonlinear process, two of them were discussed in detail. Spectral bandwidth compression relies on the same group-velocity relationship. Through absent spectral correlations between input and output fields, and a narrow phasematching bandwidth, the output field has a reduced spectral bandwidth. Bandwidth compression by a factor of 7.47 was measured. Through measurement of the Klyshko efficiency before and after conversion, efficient reshaping was proven. By monitoring the second order correlation function, the absence of noise photons added by the nonlinear process was verified. In an outlook, tunability of the process has been discussed. Numerical calculations showed that the process can both be detuned to different wavelength through temperature, and also implemented in materials with different amount of birefringence.

As a second application, optical cross-correlation measurements were discussed. The group-velocity matching in the QPG process allows to implement a sampling-method for measuring the temporal intensity envelope of single photon. A fast delay in the form of a spinning plate of glass was used to decrease measurement time. The introduced apparatus was employed to measure the temporal envelope of PDC photons. Together with spectral measurements, a method to establish lower bounds for the photon's spectral purity was demonstrated. In result, it was shown that correlated or anticorrelated states of quantum light are more robust to chirps than decorrelated states. Finally, it was noted, that the process can under certain conditions be used to implement a cross-FROG measurement.

In the forth chapter, the previously introduced approach to dispersion engineering was applied to a new problem. While upconversion detection is a well established approach to improve detection efficiency when efficient detectors are available in a different spectral domain, it has rarely been applied to time-resolved measurements. A frequency conversion process for such an application has to be both efficient and preserve the temporal envelope of the pulse. The required efficiency was demonstrated in a proof-of-principle experiment, in which the measurement of the temporal intensity envelope of light generated with a PDC source was demonstrated using a commercially available streak camera. In the following sections, the influence of spectral correlations on the pulse-imaging properties of the nonlinear process were investigated. Using a double-Gaussian approximation of the transfer function, it was shown that imaging parameters such as resolution, apertures and magnification can be described analytically. The derived parameters for the phasematching were then compared to numerical simulations using actual material and waveguide dispersion parameters. As a result, it was shown that the dispersion properties of Lithium Niobate allow to implement functional devices for time-domain upconversion detection.

# BIBLIOGRAPHY

[1] C. K. Hong, Z. Y. Ou, and L. Mandel. Measurement of subpicosecond time intervals between two photons by interference. *Physical Review Letters*, 59(18):2044–2046, 1987.

[2] G. Harder, V. Ansari, B. Brecht, T. Dirmeier, C. Marquardt, and C. Silberhorn. An optimized photon pair source for quantum circuits. *Opt. Express*, 21(12):13975–13985, 2013.

[3] V. Ansari, E. Roccia, M. Santandrea, M. Doostdar, C. Eigner, L. Padberg, I. Gianani, M. Sbroscia, J. M. Donohue, L. Mancino, M. Barbieri, and C. Silberhorn. Heralded generation of high-purity ultrashort single photons in programmable temporal shapes. *Optics Express*, 26(3): 2764–2774, 2018.

[4] F. Graffitti, P. Barrow, M. Proietti, D. Kundys, and A. Fedrizzi. Independent high-purity photons created in domain-engineered crystals. *Optica*, 5(5):514, 2018.

[5] N. Montaut, L. Sansoni, E. Meyer-Scott, R. Ricken, V. Quiring, H. Herrmann, and C. Silberhorn. High-Efficiency Plug-and-Play Source of Heralded Single Photons. *Physical Review Applied*, 8(2):024021, 2017.

[6] A. C. Dada, T. S. Santana, R. N. E. Malein, A. Koutroumanis, Y. Ma, J. M. Zajac, J. Y. Lim, J. D. Song, and B. D. Gerardot. Indistinguishable single photons with flexible electronic triggering. *Optica*, 3(5):493, 2016.

[7] G. Kiršanskė, H. Thyrrestrup, R. S. Daveau, C. L. Dreeßen, T. Pregnolato, L. Midolo, P. Tighineanu, A. Javadi, S. Stobbe, R. Schott, A. Ludwig, A. D. Wieck, S. I. Park, J. D. Song, A. V. Kuhlmann, I. Söllner, M. C. Löbl, R. J. Warburton, and P. Lodahl. Indistinguishable and efficient single photons from a quantum dot in a planar nanobeam waveguide. *Physical Review B*, 96(16), 2017.

[8] A. Reiserer and G. Rempe. Cavity-based quantum networks with single atoms and optical photons. *Reviews of Modern Physics*, 87(4):1379–1418, 2015.

[9] N. Kalb, A. Reiserer, S. Ritter, and G. Rempe. Heralded Storage of a Photonic Quantum Bit in a Single Atom. *Physical Review Letters*, 114 (22):220501, 2015.

[10] L. K. Shalm, E. Meyer-Scott, B. G. Christensen, P. Bierhorst, M. A. Wayne, M. J. Stevens, T. Gerrits, S. Glancy, D. R. Hamel, M. S. Allman, K. J. Coakley, S. D. Dyer, C. Hodge, A. E. Lita, V. B. Verma, C. Lambrocco, E. Tortorici, A. L. Migdall, Y. Zhang, D. R. Kumor, W. H. Farr, F. Marsili, M. D. Shaw, J. A. Stern, C. Abellán, W. Amaya, V. Pruneri, T. Jennewein, M. W. Mitchell, P. G. Kwiat, J. C. Bienfang, R. P. Mirin, E. Knill, and S. W. Nam. Strong Loophole-Free Test of Local Realism. *Physical Review Letters*, 115(25):250402, 2015.

[11] B. Hensen, H. Bernien, A. E. Dreau, A. Reiserer, N. Kalb, M. S. Blok, J. Ruitenberg, R. F. L. Vermeulen, R. N. Schouten, C. Abellan, W. Amaya, V. Pruneri, M. W. Mitchell, M. Markham, D. J. Twitchen, D. Elkouss, S. Wehner, T. H. Taminiau, and R. Hanson. Loophole-free Bell inequality violation using electron spins separated by 1.3 kilometres. *Nature*, 526 (7575):682–686, 2015.

[12] S.-K. Liao, W.-Q. Cai, J. Handsteiner, B. Liu, J. Yin, L. Zhang, D. Rauch, M. Fink, J.-G. Ren, W.-Y. Liu, Y. Li, Q. Shen, Y. Cao, F.-Z. Li, J.-F. Wang, Y.-M. Huang, L. Deng, T. Xi, L. Ma, T. Hu, L. Li, N.-L. Liu, F. Koidl, P. Wang, Y.-A. Chen, X.-B. Wang, M. Steindorfer, G. Kirchner, C.-Y. Lu, R. Shu, R. Ursin, T. Scheidl, C.-Z. Peng, J.-Y. Wang, A. Zeilinger, and J.-W. Pan. Satellite-Relayed Intercontinental Quantum Network. *Physical Review Letters*, 120(3):030501, 2018.

[13] M. R. Sprague, P. S. Michelberger, T. F. M. Champion, D. G. England, J. Nunn, X.-M. Jin, W. S. Kolthammer, A. Abdolvand, P. S. J. Russell, and I. A. Walmsley. Broadband single-photon-level memory in a hollow-core photonic crystal fibre. *Nature Photonics*, 8(4):287–291, 2014.

[14] E. Poem, C. Weinzetl, J. Klatzow, K. T. Kaczmarek, J. H. D. Munns, T. F. M. Champion, D. J. Saunders, J. Nunn, and I. A. Walmsley. Broadband noise-free optical quantum memory with neutral nitrogen-vacancy centers in diamond. *Physical Review B*, 91(20):205108, 2015.

[15] H. J. Kimble. The quantum internet. *Nature*, 453(7198):1023–1030, 2008.

[16] N. Maring, P. Farrera, K. Kutluer, M. Mazzera, G. Heinze, and H. d. Riedmatten. Photonic quantum state transfer between a cold atomic gas and a crystal. *Nature*, 551(7681):485–488, 2017.

[17] N. Maring, D. Lago-Rivera, A. Lenhard, G. Heinze, and H. d. Riedmatten. Quantum frequency conversion of memory-compatible single photons from 606 nm to the telecom C-band. *Optica*, 5(5):507–513, 2018.

[18] P. J. Mosley, J. S. Lundeen, B. J. Smith, P. Wasylczyk, A. B. U'Ren, C. Silberhorn, and I. A. Walmsley. Heralded Generation of Ultrafast Single Photons in Pure Quantum States. *Physical Review Letters*, 100(13): 133601, 2008.

[19] A. Eckstein, B. Brecht, and C. Silberhorn. A quantum pulse gate based on spectrally engineered sum frequency generation. *Optics Express*, 19 (15):13770–13778, 2011.

[20] B. Brecht, A. Eckstein, R. Ricken, V. Quiring, H. Suche, L. Sansoni, and C. Silberhorn. Demonstration of coherent time-frequency Schmidt mode selection using dispersion-engineered frequency conversion. *Physical Review A*, 90(3):030302, 2014.

[21] V. Ansari, J. M. Donohue, B. Brecht, and C. Silberhorn. Tailoring nonlinear processes for quantum optics with pulsed temporal-mode encodings. *Optica*, 5(5):534–550, 2018.

[22] N. Onodera, H. Ito, and H. Inaba. Real-time measurement of picosecond optical pulses from an InGaAsP diode laser using an ultrafast streak camera with infrared frequency up-conversion. *Applied Physics Letters*, 43(8):720, 1983.

[23] C. Lin, L. G. Cohen, and H. Kogelnik. Optical-pulse equalization of low-dispersion transmission in single-mode fibers in the 1.3–1.7-micrometer spectral region. *Optics Letters*, 5(11):476, 1980.

[24] K. Garay-Palmett, A. B. U'Ren, R. Rangel-Rojo, R. Evans, and S. Camacho-López. Ultrabroadband photon pair preparation by spontaneous four-wave mixing in a dispersion-engineered optical fiber. *Physical Review A*, 78(4):043827, 2008.

[25] E. Meyer-Scott, N. Montaut, J. Tiedau, L. Sansoni, H. Herrmann, T. J. Bartley, and C. Silberhorn. Limits on the heralding efficiencies and spectral purities of spectrally filtered single photons from photon-pair sources. *Physical Review A*, 95(6):061803(R), 2017.

[26] C. M. Natarajan, M. G. Tanner, and R. H. Hadfield. Superconducting nanowire single-photon detectors: physics and applications. *Superconductor Science and Technology*, 25(6):063001, 2012.

[27] D. Stucki, N. Walenta, F. Vannel, R. T. Thew, N. Gisin, H. Zbinden, S. Gray, C. R. Towery, and S. Ten. High rate, long-distance quantum key distribution over 250 km of ultra low loss fibres. *New Journal of Physics*, 11(7):075003, 2009.

[28] A. Eckstein. *Mastering quantum light pulses with nonlinear waveguide interactions, Kontrolle über Quantenlichtpulse durch nichtlineare Interaktion in Wellenleitern.* PhD thesis, Friedrich-Alexander-Universität at Erlangen-Nürnberg, 2012.

[29] B. Brecht. *Engineering ultrafast quantum frequency conversion.* PhD thesis, Universität Paderborn, Paderborn, 2014.

[30] G. Harder. *Optimized down-conversion source and state-characterization tools for quantum optics.* PhD thesis, Universität Paderborn, Paderborn, 2016.

[31] R. S. Quimby. *Photonics and lasers: an introduction.* Wiley-Interscience, Hoboken, N.J, 2006.

[32] R. W. Boyd. *Nonlinear optics.* Academic Press, Amsterdam ; Boston, 3rd ed edition, 2008.

[33] R. L. Sutherland, D. G. McLean, and S. Kirkpatrick. *Handbook of nonlinear optics.* Number 82 in Optical engineering. Marcel Dekker, New York, 2nd ed., rev. and expanded edition, 2003.

[34] A. Migdall, S. Polyakov, J. Fan, and J. Bienfang, editors. *Single-photon generation and detection: experimental methods in the physical sciences.* Number volume 45 in Experimental methods in the physical sciences. Elsevier/AP, Academic Press is an imprint of Elsevier, Amsterdam ; Boston, 2013.

[35] D. N. Nikogosian. *Nonlinear optical crystals: a complete survey.* Springer-Science, New York, 2005.

[36] J. A. Armstrong, N. Bloembergen, J. Ducuing, and P. S. Pershan. Interactions between Light Waves in a Nonlinear Dielectric. *Physical Review*, 127(6):1918–1939, 1962.

[37] O. Kuzucu, F. N. C. Wong, S. Kurimura, and S. Tovstonog. Joint Temporal Density Measurements for Two-Photon State Characterization. *Physical Review Letters*, 101(15):153602, 2008.

[38] A. Eckstein, A. Christ, P. J. Mosley, and C. Silberhorn. Highly Efficient Single-Pass Source of Pulsed Single-Mode Twin Beams of Light. *Physical Review Letters*, 106(1):013603, 2011.

[39] A. Christ, B. Brecht, W. Mauerer, and C. Silberhorn. Theory of quantum frequency conversion and type-II parametric down-conversion in the high-gain regime. *New Journal of Physics*, 15(5):053038, 2013.

[40] N. Quesada and J. E. Sipe. High efficiency in mode-selective frequency conversion. *Optics Letters*, 41(2):364, 2016.

[41] B. Brecht, A. Eckstein, A. Christ, H. Suche, and C. Silberhorn. From quantum pulse gate to quantum pulse shaper—engineered frequency conversion in nonlinear optical waveguides. *New Journal of Physics*, 13 (6):065029, 2011.

[42] V. Ansari, J. M. Donohue, M. Allgaier, L. Sansoni, B. Brecht, J. Roslund, N. Treps, G. Harder, and C. Silberhorn. Tomography and Purification of

the Temporal-Mode Structure of Quantum Light. *Physical Review Letters*, 120(21):213601, 2018.

[43] D. V. Reddy, M. G. Raymer, C. J. McKinstrie, L. Mejling, and K. Rottwitt. Temporal mode selectivity by frequency conversion in second-order nonlinear optical waveguides. *Optics Express*, 21(11):13840–13863, 2013.

[44] D. V. Reddy and M. G. Raymer. Engineering temporal-mode-selective frequency conversion in nonlinear optical waveguides: from theory to experiment. *Optics Express*, 25(11):12952, 2017.

[45] D. V. Reddy and M. G. Raymer. Photonic temporal-mode multiplexing by quantum frequency conversion in a dichroic-finesse cavity. *Optics Express*, 26(21):28091, 2018.

[46] B. Brecht, D. V. Reddy, C. Silberhorn, and M. G. Raymer. Photon Temporal Modes: A Complete Framework for Quantum Information Science. *Physical Review X*, 5(4):041017, 2015.

[47] M. Allgaier, V. Ansari, L. Sansoni, C. Eigner, V. Quiring, R. Ricken, G. Harder, B. Brecht, and C. Silberhorn. Highly efficient frequency conversion with bandwidth compression of quantum light. *Nature Communications*, 8:14288, 2017.

[48] M. Allgaier, G. Vigh, V. Ansari, C. Eigner, V. Quiring, R. Ricken, Benjamin Brecht, and C. Silberhorn. Fast time-domain measurements on telecom single photons. *Quantum Science and Technology*, 2(3):034012, 2017.

[49] C. K. Law, I. A. Walmsley, and J. H. Eberly. Continuous Frequency Entanglement: Effective Finite Hilbert Space and Entropy Control. *Physical Review Letters*, 84(23):5304–5307, 2000.

[50] A. Monmayrant, S. Weber, and B. Chatel. A newcomer's guide to ultrashort pulse shaping and characterization. *Journal of Physics B: Atomic, Molecular and Optical Physics*, 43(10):103001, 2010.

[51] V. Ansari, G. Harder, M. Allgaier, B. Brecht, and C. Silberhorn. Temporal-mode measurement tomography of a quantum pulse gate. *Physical Review A*, 96(6):063817, 2017.

[52] P. Manurkar, N. Jain, M. Silver, Y.-P. Huang, C. Langrock, M. M. Fejer, P. Kumar, and G. S. Kanter. Multidimensional mode-separable frequency conversion for high-speed quantum communication. *Optica*, 3(12):1300–1307, 2016.

[53] A. Shahverdi, Y. M. Sua, L. Tumeh, and Y.-P. Huang. Quantum Parametric Mode Sorting: Beating the Time-Frequency Filtering. *Scientific Reports*, 7(1):6495, 2017.

[54] M. S. Shahriar, P. Kumar, and P. R. Hemmer. Connecting processing-capable quantum memories over telecommunication links via quantum

frequency conversion. *Journal of Physics B: Atomic, Molecular and Optical Physics*, 45(12):124018, 2012.

[55] N. Curtz, R. Thew, C. Simon, N. Gisin, and H. Zbinden. Coherent frequency-down-conversion interface for quantum repeaters. *Optics Express*, 18(21):22099–22104, 2010.

[56] J. S. Pelc, L. Yu, K. De Greve, P. L. McMahon, C. M. Natarajan, V. Esfandyarpour, S. Maier, C. Schneider, M. Kamp, S. Höfling, R. H. Hadfield, A. Forchel, Y. Yamamoto, and M. M. Fejer. Downconversion quantum interface for a single quantum dot spin and 1550-nm single-photon channel. *Optics Express*, 20(25):27510, 2012.

[57] B. Albrecht, P. Farrera, X. Fernandez-Gonzalvo, M. Cristiani, and H. d. Riedmatten. A waveguide frequency converter connecting rubidium-based quantum memories to the telecom C-band. *Nature Communications*, 5:3376, 2014.

[58] M. Karpiński, M. Jachura, L. J. Wright, and B. J. Smith. Bandwidth manipulation of quantum light by an electro-optic time lens. *Nature Photonics*, 11:53, 2016.

[59] M. G. Raymer and K. Srinivasan. Manipulating the color and shape of single photons. *Physics Today*, 65(11):32, 2012.

[60] J. Lavoie, J. M. Donohue, L. G. Wright, A. Fedrizzi, and K. J. Resch. Spectral compression of single photons. *Nature Photonics*, 7(5):363–366, 2013.

[61] J. M. Donohue, M. D. Mazurek, and K. J. Resch. Theory of high-efficiency sum-frequency generation for single-photon waveform conversion. *Physical Review A*, 91(3):033809, 2015.

[62] K. A. G. Fisher, D. G. England, J.-P. W. MacLean, P. J. Bustard, K. J. Resch, and B. J. Sussman. Frequency and bandwidth conversion of single photons in a room-temperature diamond quantum memory. *Nature Communications*, 7:11200, 2016.

[63] D. N. Klyshko. Use of two-photon light for absolute calibration of photoelectric detectors. *Soviet Journal of Quantum Electronics*, 10(9):1112–1117, 1980.

[64] M. Avenhaus, A. Eckstein, P. J. Mosley, and C. Silberhorn. Fiber-assisted single-photon spectrograph. *Optics Letters*, 34(18):2873–2875, 2009.

[65] R. H. Brown and R. Q. Twiss. A Test of a New Type of Stellar Interferometer on Sirius. *Nature*, 178(4541):1046–1048, 1956.

[66] G. J. Edwards and M. Lawrence. A temperature-dependent dispersion

equation for congruently grown lithium niobate. *Optical and Quantum Electronics*, 16(4):373–375, 1984.

[67] D. H. Jundt. Temperature-dependent Sellmeier equation for the index of refraction, n_e, in congruent lithium niobate. *Optics Letters*, 22(20): 1553, 1997.

[68] P. A. Augstov and K. K. Shvarts. The temperature and light intensity dependence of photorefraction in LiNbO3. *Applied Physics*, 21(2):191–194, 1980.

[69] K. Kato and E. Takaoka. Sellmeier and thermo-optic dispersion formulas for KTP. *Applied Optics*, 41(24):5040, 2002.

[70] K. S. Abedin and H. Ito. Temperature-dependent dispersion relation of ferroelectric lithium tantalate. *Journal of Applied Physics*, 80(11):6561–6563, 1996.

[71] C. Hepp, T. Müller, V. Waselowski, J. N. Becker, B. Pingault, H. Sternschulte, D. Steinmüller-Nethl, A. Gali, J. R. Maze, M. Atatüre, and C. Becher. Electronic Structure of the Silicon Vacancy Color Center in Diamond. *Physical Review Letters*, 112(3):036405, 2014.

[72] B. Pingault, D.-D. Jarausch, C. Hepp, L. Klintberg, J. N. Becker, M. Markham, C. Becher, and M. Atatüre. Coherent control of the silicon-vacancy spin in diamond. *Nature Communications*, 8:15579, 2017.

[73] Y. Zhou, A. Rasmita, K. Li, Q. Xiong, I. Aharonovich, and W.-b. Gao. Coherent control of a strongly driven silicon vacancy optical transition in diamond. *Nature Communications*, 8:14451, 2017.

[74] J. N. Becker, B. Pingault, D. Groß, M. Gündoğan, N. Kukharchyk, M. Markham, A. Edmonds, M. Atatüre, P. Bushev, and C. Becher. All-Optical Control of the Silicon-Vacancy Spin in Diamond at Millikelvin Temperatures. *Physical Review Letters*, 120(5):053603, 2018.

[75] J. A. Armstrong. Measurement of picosecond laser pulse widths. *Applied Physics Letters*, 10(1):16, 1967.

[76] D. J. Kane and R. Trebino. Characterization of arbitrary femtosecond pulses using frequency-resolved optical gating. *IEEE Journal of Quantum Electronics*, 29(2):571–579, 1993.

[77] S. Linden, H. Giessen, and J. Kuhl. XFROG - A New Method for Amplitude and Phase Characterization of Weak Ultrashort Pulses. *physica status solidi (b)*, 206(1):119–124, 1998.

[78] J. Wiersig, C. Gies, F. Jahnke, M. Aszmann, T. Berstermann, M. Bayer, C. Kistner, S. Reitzenstein, C. Schneider, S. Hofling, A. Forchel, C. Kruse, J. Kalden, and D. Hommel. Direct observation of correlations between

individual photon emission events of a microcavity laser. *Nature*, 460 (7252):245–249, 2009.

[79] M. Komura and S. Itoh. Fluorescence measurement by a streak camera in a single-photon-counting mode. *Photosynthesis Research*, 101(2-3): 119–133, 2009.

[80] A. Christ, K. Laiho, A. Eckstein, K. N. Cassemiro, and C. Silberhorn. Probing multimode squeezing with correlation functions. *New Journal of Physics*, 13(3):033027, 2011.

[81] A. B. U'Ren, Y. Jeronimo-Moreno, and H. Garcia-Gracia. Generation of Fourier-transform-limited heralded single photons. *Physical Review A*, 75(2):023810, 2007.

[82] J.-P. W. MacLean, J. M. Donohue, and K. J. Resch. Direct Characterization of Ultrafast Energy-Time Entangled Photon Pairs. *Physical Review Letters*, 120(5):053601, 2018.

[83] R. D. Boggy, R. H. Johnson, J. M. Eggleston, and C. W. Schulthess. Rapid scanning autocorrelation detector, 1983. U.S. Classification 356/450, 968/854, 356/520, 356/121; International Classification G01J11/00, G04F13/02; Cooperative Classification G01J11/00, G04F13/026; European Classification G04F13/02C, G01J11/00.

[84] B. Reitemeier. *A Novel Concept for Fast Terahertz Imaging*. Bachelor Thesis, Philipps-Universität Marburg, Marburg, 2013.

[85] T. Probst, A. Rehn, S. F. Busch, S. Chatterjee, M. Koch, and M. Scheller. Cost-efficient delay generator for fast terahertz imaging. *Optics Letters*, 39(16):4863–4866, 2014.

[86] K. N. Cassemiro, K. Laiho, and C. Silberhorn. Accessing the purity of a single photon by the width of the Hong–Ou–Mandel interference. *New Journal of Physics*, 12(11):113052, 2010.

[87] B. Brecht and C. Silberhorn. Characterizing entanglement in pulsed parametric down-conversion using chronocyclic wigner functions. *Phys. Rev. A*, 87:053810, 2013.

[88] X. Sanchez-Lozano, A. B. U'Ren, and J. L. Lucio. On the relationship between pump chirp and single-photon chirp in spontaneous parametric downconversion. *Journal of Optics*, 14(1):015202, 2012.

[89] G. Gibson, J. Courtial, M. J. Padgett, M. Vasnetsov, V. Pas'ko, S. M. Barnett, and S. Franke-Arnold. Free-space information transfer using light beams carrying orbital angular momentum. *Optics Express*, 12(22): 5448–5456, 2004.

[90] G. C. G. Berkhout, M. P. J. Lavery, J. Courtial, M. W. Beijersbergen, and

M. J. Padgett. Efficient Sorting of Orbital Angular Momentum States of Light. *Physical Review Letters*, 105(15):153601, 2010.

[91] G. Molina-Terriza, J. P. Torres, and L. Torner. Management of the Angular Momentum of Light: Preparation of Photons in Multidimensional Vector States of Angular Momentum. *Physical Review Letters*, 88(1):013601, 2001.

[92] A. Hayat, X. Xing, A. Feizpour, and A. M. Steinberg. Multidimensional quantum information based on single-photon temporal wavepackets. *Optics Express*, 20(28):29174–29184, 2012.

[93] M. Allgaier, V. Ansari, C. Eigner, V. Quiring, R. Ricken, J. M. Donohue, T. Czerniuk, M. Aßmann, M. Bayer, B. Brecht, and C. Silberhorn. Streak camera imaging of single photons at telecom wavelength. *Applied Physics Letters*, 112(3):031110, 2018.

[94] P. Manurkar, N. Jain, P. Kumar, and G. S. Kanter. Programmable optical waveform reshaping on a picosecond timescale. *Optics Letters*, 42(5): 951–954, 2017.

[95] V. Kabelka and A. V. Masalov. Angularly resolved autocorrelation for single-shot time-frequency imaging of ultrashort light pulse. *Optics Communications*, 121(4-6):141–148, 1995.

[96] A. Campillo and S. Shapiro. Picosecond streak camera fluorometry - A review. *IEEE Journal of Quantum Electronics*, 19(4):585–603, 1983.

[97] R. Kodama, K. Okada, and Y. Kato. Development of a two-dimensional space-resolved high speed sampling camera. *Review of Scientific Instruments*, 70(1):625–628, 1999.

[98] L. Gao, J. Liang, C. Li, and L. V. Wang. Single-shot compressed ultrafast photography at one hundred billion frames per second. *Nature*, 516 (7529):74–77, 2014.

[99] M. Aßmann, F. Veit, M. Bayer, C. Gies, F. Jahnke, S. Reitzenstein, S. Höfling, L. Worschech, and A. Forchel. Ultrafast tracking of second-order photon correlations in the emission of quantum-dot microresonator lasers. *Physical Review B*, 81(16):165314, 2010.

[100] M. Aßmann, F. Veit, J.-S. Tempel, T. Berstermann, H. Stolz, M. van der Poel, J. M. Hvam, and M. Bayer. Measuring the dynamics of second-order photon correlation functions inside a pulse with picosecond time resolution. *Optics Express*, 18(19):20229, 2010.

[101] D. N. Fittinghoff, I. A. Walmsley, J. L. Bowie, J. N. Sweetser, R. T. Jennings, M. A. Krumbügel, K. W. DeLong, and R. Trebino. Measurement of the intensity and phase of ultraweak, ultrashort laser pulses. *Optics Letters*, 21(12):884–886, 1996.

[102] A. O. Davis, M. Karpinski, and B. J. Smith. Single-Photon Temporal Wave Function Measurement via Electro-Optic Spectral Shearing Interferometry. In *Conference on Lasers and Electro-Optics (2016), paper FTu4C.6*, page FTu4C.6. Optical Society of America, 2016.

[103] C. Santori, G. S. Solomon, M. Pelton, and Y. Yamamoto. Time-resolved spectroscopy of multiexcitonic decay in an InAs quantum dot. *Physical Review B*, 65(7):073310, 2002.

[104] H. Deng, G. Weihs, C. Santori, J. Bloch, and Y. Yamamoto. Condensation of Semiconductor Microcavity Exciton Polaritons. *Science*, 298(5591): 199–202, 2002.

[105] W. Langbein. Spontaneous parametric scattering of microcavity polaritons in momentum space. *Physical Review B*, 70(20):205301, 2004.

[106] R. Machulka, K. Lemr, O. Haderka, M. Lamperti, A. Allevi, and M. Bondani. Luminescence-induced noise in single photon sources based on BBO crystals. *Journal of Physics B: Atomic, Molecular and Optical Physics*, 47(21):215501, 2014.

[107] N. V. Pletnev, V. V. Apollonov, and V. R. Sorochenko. Registration of picosecond CO2 laser pulses by means of two-stage parametric transformation in nonlinear crystals. *Instruments and Experimental Techniques*, 52(3):412–420, 2009.

[108] S. Andreev, N. Andreeva, I. Matveev, and S. Pshenichnikov. Conversion of Co2-Laser Radiation into the 0.5-Mu-M Region in Non-Linear Crystals. *Kvantovaya Elektronika*, 8(6):1361–1363, 1981.

[109] I. H. White, D. F. G. Gallagher, M. Osinski, and D. Bowley. Direct streak-camera observation of picosecond gain-switched optical pulses from a 1.5 micrometer semiconductor laser. *Electronics Letters*, 21(5):197–199, 1985.

[110] HAMAMATSU PHOTONICS K.K., Systems Division. Universal Streak Camera C5680 Series, 2003.

[111] A. P. Vandevender and P. G. Kwiat. High efficiency single photon detection via frequency up-conversion. *Journal of Modern Optics*, 51(9-10): 1433–1445, 2004.

[112] R. T. Thew, S. Tanzilli, L. Krainer, S. C. Zeller, A. Rochas, I. Rech, S. Cova, H. Zbinden, and N. Gisin. Low jitter up-conversion detectors for telecom wavelength GHz QKD. *New Journal of Physics*, 8(3):32–32, 2006.

[113] J. S. Pelc, L. Ma, C. R. Phillips, Q. Zhang, C. Langrock, O. Slattery, X. Tang, and M. M. Fejer. Long-wavelength-pumped upconversion single-

photon detector at 1550 nm: performance and noise analysis. *Optics Express*, 19(22):21445, 2011.

[114] L. W. Turner. *Electronics Engineer's Reference Book*. Butterworth-Heinemann, London, Boston, 4th edition, 1976.

[115] L. M. Davis and C. Parigger. Use of streak camera for time-resolved photon counting fluorimetry. *Measurement Science and Technology*, 3 (1):85, 1992.

[116] HAMAMATSU PHOTONICS K.K., Systems Division. NIR streak camera C11293-02, 2015.

[117] A. Secroun, A. Mens, D. Gontier, P. Brunel, J.-C. Rebuffie, and C. Goulmy. Experimental and theoretical characterization of noise in a streak camera. *Proc. SPIE*, 3429:32–38, 1998.

[118] O. H. W. Siegmund, J. Vallerga, and B. Wargelin. Background events in microchannel plates. *IEEE Transactions on Nuclear Science*, 35(1): 524–528, 1988.

[119] A. P. Baronavski, H. D. Ladouceur, and J. K. Shaw. Analysis of cross correlation, phase velocity mismatch and group velocity mismatches in sum-frequency generation. *IEEE Journal of Quantum Electronics*, 29(2): 580–589, 1993.

[120] R. Glowinski, S. J. Osher, W. Yin, and Springer International Publishing AG. *Splitting Methods in Communication, Imaging, Science, and Engineering*. Springer, 2016. OCLC: 971204397.

[121] C. L. Van, H. N. Viet, M. Trippenbach, and K. D. Xuan. Propagation Technique for Ultrashort Pulses II: Numerical Methods to Solve the Pulse Propagation Equation. *Computational Methods in Science and Technology*, 14(1):13–19, 2008.

[122] J. R. Cash and A. H. Karp. A variable order Runge-Kutta method for initial value problems with rapidly varying right-hand sides. *ACM Transactions on Mathematical Software*, 16(3):201–222, 1990.

[123] W. H. Press, editor. *FORTRAN numerical recipes*. Cambridge University Press, Cambridge [England] ; New York, 2nd ed edition, 1996.

# ACKNOWLEDGMENTS

If you have read this far, you must really be into frequency conversion. Think about that. Isn't that a weird thing to have as a hobby? But good for you. And thanks for reading.

I would like to thank Prof. Dr. Christine Silberhorn for taking me on as a doctoral student and giving me the opportunity to work with her. I learned a lot, and hope I could contribute to the group. Furthermore, I thank Prof. Dr. Manfred Bayer for being my second supervisor. Working with researchers outside my own group was exciting and hopefully mutually beneficial. I also want to thank both Manfred Bayer and Christine Silberhorn for evaluating this thesis.

Off course, not a day goes by without thinking about the tax payer that financed by research. I received my funding through the SFB TRR 142 "Tailored Nonlinear Photonics: From Fundamental Concepts to Functional Structures". I also had the pleasure to work closely with colleagues within the European Union's Horizon 2020 projects QCUMbER (No. 665148). The collaboration within this project was a pleasure, and the many connections and friendships made during research postings and meetings bear witness to the "idea of a common Europe". Science knows no borders.

I thank Alexander Franzen for providing everyone with the *gwoptics* ComponentLibrary used throughout the setup sketches in this thesis.

This work would not have been possible without collaborations outside of Paderborn. Most notably, the up-conversion project was a collaboration within the SFB TRR 142. The work was conducted with members of Manfred Bayer's group at the TU Dortmund. I have to thank Thomas Czerniuk and Marc Aßmann for helping with getting the streak camera to Paderborn and setting it up. I also thank Johannes Thewes with whom I planned the setup for the final upconversion experiment, which was not yet set up when this thesis was completed. I also thank Benjamin Brecht, who always helped out when questions came up, even though he was formally not a member of the group while he worked in Oxford. There were also collaborations that didn't yield anything within the scope of this thesis, but were productive and entertaining otherwise. I thank Giuseppe Patera for the many discussions on time lenses. While there is none of that stuff in my thesis, the discussions helped me greatly with understanding pulse imaging. Giuseppe Patera the scientist is not to be confused with Giuseppe Patera the accordionist.

Of course I am grateful for the many people here in Paderborn I had the pleasure to work with. First, I want to thank all of those that worked with me on my research directly: John Matthew Donohue, Christof Eigner, Georg Harder, Jano Gil Lopez, Viktor Quiring, Raimund Ricken, Linda Sansoni. I thank Gesche Vigh for the splendid time during her bachelor thesis,during which she pulled that marvelous spinning glass plate thingy from the 3d printer. Good job! Special thanks goes to everyone in the clean room. Honestly, I do only the easy part of making devices, which is doing some simple math and telling others what to do. Ramund does a great job producing our samples, Christof greatly contributed with his new poling setup and designing brilliant optical coatings, Viktor is the master of the coating machine, Laura, Felix and Matteo do fantastic work improving our technology in many aspects, and I know all our current and past trainees also do a lot of helping out in the clean room and even profuce the one or other brilliant sample. If someone feels left out until now: You're up in a second.

These acknowledgments would not be complete if I did not mention some *very* special people from the group. To Regina Kruse: Thank you for the much needed coffee breaks, for Baileys in the morning and Captain Chaos in the evenings. It hasn't been half as much fun since you left. I also thank Vahid Ansari. We shared most of the experimental setup, and for almost 2 years we suffered from the damn thing not working. I believe that during that time, you did most of the heavy lifting, and I'm glad your experiments turned out as good as mine in the end. You deserve much of the credit. I thank Michael Stefzky for bad movies, and Matteo Santandrea for good math. I thank Sonja Barkhofen for pointing out that Paderborn has a university - otherwise I never would have come here. And then there's Thomas Nitsche. We started our time as PhD students on the same day, and I thank you for the fun times in the office. But I will never forgive you for telling me to turn down "Daylight in your eyes“ during our road trip. That song is awesome. Thanks for the many good laughs in the office. I appreciate your sense of humor!

But really everything here in Paderborn is a group effort, and I cherish the many discussions, helping out, borrowing equipment, explaining setups, and the cake.

I thank again Regina Kruse, and also Basti Reitemeier and Rico Weskamp for having a look through my thesis and giving me feedback. You're the best. I also thank Basti for all of the advice with the spinning glass thingy, it was really inspired by his bachelor thesis.

And then there's more. I came to Paderborn for the research, but it's no secret I find the town pretty dull otherwise. I am thankful for the great cycling and climbing community here for making it bearable anyhow. I thank everyone at the RG Paderborn, the Paderborn chapter of the alpine club, the crew at Blocbuster, the crew in Brakel, Georg and Bernd for teaching me how to rock climb, and especially Michi for sharing my wanderlust. And last but not least, thanks everyone who I forgot to mention.

APPENDIX A

# DATA EVALUATION PROCEDURE FOR CROSS-CORRELATION MEASUREMENTS

In chapter 3.4 results for optical cross-correlation measurements on PDC photons were reported. In this appendix, the data evaluation procedure is explained in more detail. The data for the decorrelated state is used as an example.

The converted light from the Lithium Niobate waveguide is deliberately not separated in depth from background arising from, for example, anti-Stokes-scattered pump light, only from the pump beam itself. The absolute time of each detection event on the Si-APD is recorded on an AIT TTM8000 time-to-digital converter (TDC). The signal of the Silicon photodiode placed behind the delay device's chopper wheel is also fed to the TDC, where its arrival time is also recorded. This signal will be called ”trigger“. The data for each measurement was recorded over 150 seconds, which produces about 2 GB of data. It is noteworthy that this, since the TDC is connected via network, produces a network load of about 100 Mbit/s. Heralding was not done, since the time domain envelope of a photon, which is heralded in a broadband manner, is the same as the marginal envelope. The arising background was recorded deliberately, since its count rate can be assumed to be proportional to the pump power at the end of the waveguide. This number is necessary for two reasons:

- The position of the measured signal relative to the delay rotation needs to be visible on the live-view of the arrival time histogram in the lab in order to faithfully place it at a timing, where the pump power follows a mostly flat time dependence and nothing is cut
- Having exact knowledge of relative pump power vs signal height allows to scale the measured signal accordingly in order to account for pump power fluctuations

Off course it would be an option to record pump power separately using an additional APD, but that would cause problems with synchronizing pump and signal measurement. The reason why anti-Stokes-scattered is detected at the converted light's wavelength in the first place compared to the bandwidth compression experiment, is that the light from the Ti:Sapphire laser was used at higher intensity and bandwidth, resulting in much greater peak power.

In post-processing, the relative time between each timetag and the last delay trigger signal is calculated by looping through the entire binary data file. This method is slow, but reliable. In this setup, the rotation frequency of the delay plate of about 50 Hz and the experiment repetition rate of 80.165 MHz are not synchronized, which causes a stitching error when composing the data set from individual delay periods, i.e. the individual arrival times of identical features are shifted relative to each other. The size of the stitching error depends on the number of samples within one delay period, the maximum error is therefore the sample distance, which is merely 12.8 fs, much smaller than the pump pulse duration of 150 fs, and can therefore be neglected.

Since a linear dependence of time and the delay plate's rotation angle can be assumed, the data can now be plotted in form of a histogram over the rotation angle (which will later be used to calculate the actual delay). This histogram of raw data for the decorrelated state is displayed in Figure A.1. It can be seen that there are two large distributions, with two sharp features on each. Between two trigger signals, the delay plate undergoes a full rotation, where 0 degrees corresponds to the plate being parallel to the beam, effectively blocking the pump beam. When the plate rotates, the delay decreases up to an angle of 90 degrees, when the plate is perpendicular to the beam, and then increases again. At 180 degrees the whole procedure repeats, hence the symmetry. The two distributions correspond to the background, which has four maximums where the angle of incidence is the Brewster angle. The overlap with the pulse to be sampled should be achieved between the Brewster angle and perpendicular incidence, where the pump power varies only slowly. This is where the four sharp peaks corresponding to converted counts are found here. The task is now to slice and fold the data to add up the four peaks, subtract background (which can be fitted easily), and scape it according to relative pump power.

The first step is to slice the data in two and overlay the to half distributions. They are in principle identical, and but an error of the placement of the trigger (it is constructed to fire at 0 degrees, but may be off a little bit) has to be assumed. However, this does not matter: Even if the trigger is shifted, the two distributions are equivalent. Therefore, the second half of the histogram can simply be added to the first one. The resulting histogram is shown in Figure A.2.

The second step is to overlap the two remaining peaks. Now these are not identical, but mirror images of each other, since the delay increases decreases towards 90 degrees and then increases again. The histogram therefore has

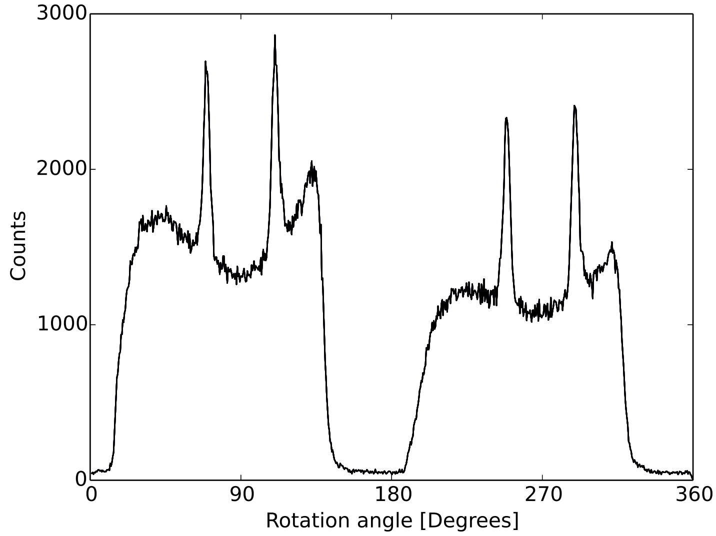

Figure A.1.: Raw data histogram for the entire rotation.

to be folded over. Now, any trigger mismatch would be a problem. However, it can be assumed that the two peaks are exactly centered around the *actual* minimum optical delay. The peaks are therefore fitted with Gaussians, the the slicing point is set to be exactly in the middle between the two peaks. The two halves are indicated in the plotted histogram by color. The folded over and added histogram is shown in Figure A.3.

Up to this point, any stacking fault could be easily identified by fitting and checking the width of the resulting distribution. If the statistical error decreases when data is stacked while the width stays constant, the stacking was accurate. This is the case for this automated procedure. Next, the background is fitted. The boundary of the actual data is set by hand, and the remaining background is fitted with a second order polynomial function, since it approximates the background well. This fit is displayed in turquoise. The fit then serves two purposes. First, it is subtracted from data to gain a background-free distribution. This approach is justified since the background is reasonably flat across the single-photon peak. Second, the relative height of the background is used to scale the data, since less background means less pump power and therefore less conversion efficiency, which is now compensated. The resulting distribution corresponds to the thick solid curve in Figure A.3.

Note that any actual trigger mismatch (the trigger firing at a angle different from zero degrees) would have shown up by now, but the recorded arrival times end at exactly 90 degrees. Therefore the trigger has fired at zero degrees. Otherwise, one would be able to correct for any mismatch, since the data *has* to end at *exactly* 90 degrees.

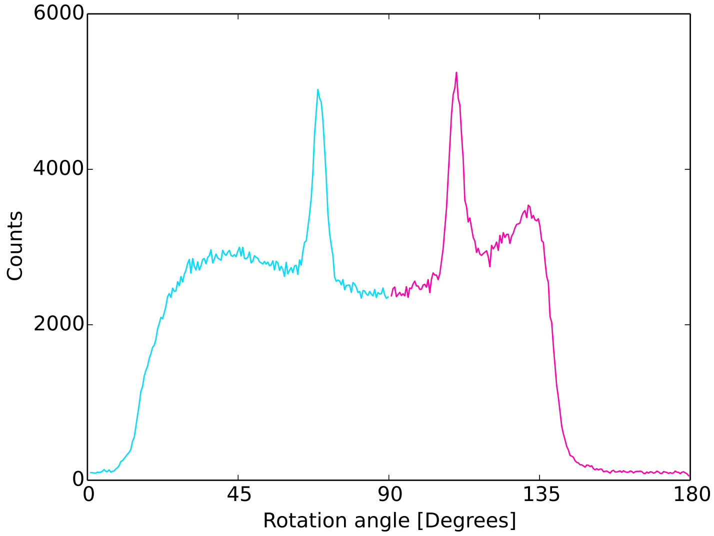

Figure A.2.: Accumulatecd raw data for a half rotation. The peaks were fitted with Gaussians, the the histogram sliced again in the middle between the two fit centers

Now, in a last step, the actual optical delay is calculated from the angle of incidence using equation 3.11. This whole procedure is mostly *blind*, and based on assumptions well justifiable from the experimental design. The only manual part is to set the boundaries of the two peaks in the half distribution shown in Figure A.2, which defines the parts of the data that is used for fitting the peaks, and fitting the background.

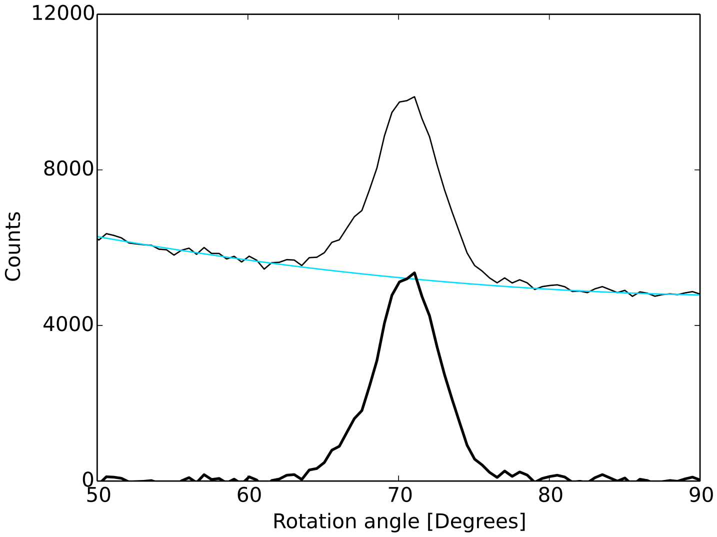

Figure A.3.: Accumulated raw data for a quarter. The turquoise line corresponds to the background fit, the thick solid line represents the scaled and background-subtracted data.

APPENDIX B

# INFLUENCE OF NOISE ON MODE OVERLAP IN THE QPS MODEL

In chapter 3.5.3 the influence of noise on the mode selectivity measurement for the QPS was briefly mentioned. Figure B.1 shows what the modeled noise looks like in the spectrum. The noise is simulated as a normally distributed random deviation from the target spectrum, where the amplitude of the noise corresponds to the standard deviation of the normal distribution. The noise was added on the spectral scale of the measurement resolution. The figure shows a forth order mode with a noise amplitude of 0.1.

Figure B.2 shows the overlap between noisy model spectra with the target spectra. Here, the experimental noise is roughly reproduced by a noise level of 0.03. The influence is uniform in both bandwidth and mode order. Note that this simulated noise corresponds to a single measurement, and would average out in the experimental measurement scenario where each measurement is repeated 8 times. It can be seen that even drastic noise as shown in Figure B.1 reduces the overlap merely to 0.995, showing that the overlap measure is fairly insensitive to noise. Hence, this effect was excluded from the model.

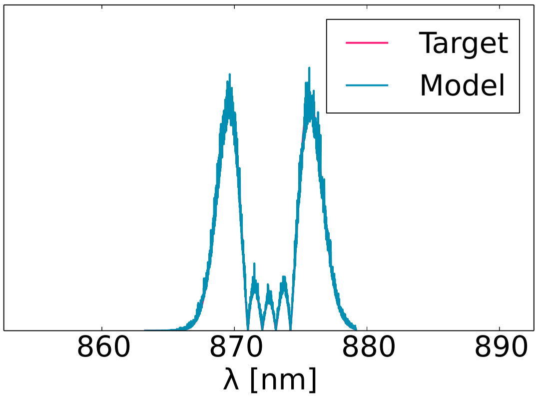

Figure B.1.: Example model spectrum for mode 4 with noise amplitude of 0.1 and bandwidth of 10 nm.

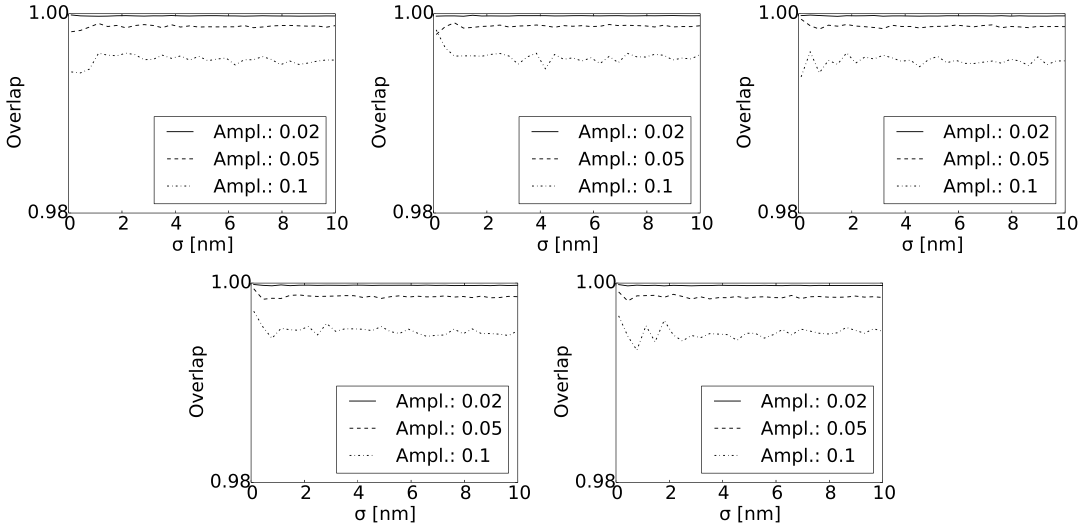

Figure B.2.: Overlap for modes 0 through with three different noise amplitudes.

APPENDIX C

# RAW STREAK CAMERA IMAGES

In chapter 4.2, a background-subtracted streak camera image was shown. Here, the raw data is presented. Figure C.1 shows the unaltered image produced by the camera software by adding 32 consecutive exposures of 32 seconds each. For all images shown, the gain for the multi channel plate electron multiplier was set to 30, which is equivalent to 80 % of the maximum value.

Figure C.2 shows the corresponding background image, where beam impinging on the camera was blocked, ambient light would still been able to reach the camera. Otherwise the image was recorded with setting identical to the ones in the last image. Before subtracting this background image, a median filter with a radius setting of 7 from the *Python Imaging Library*. A median filter replaces every pixel value with the statistical median of the surrounding pixels, effectively removing "hot" pixels, that would interfere with background subtraction. The resulting image is shown in Figure C.3. Subtracting the smoothed image helps to preserve the noise level instead of increasing it. The resulting image shown in chapter 4.2 has some background in the top left corner left. The readout happens in this corner, thus it gets hot, which increases thermal noise. This noise floor depends on many parameters, like the ambient temperature, how many exposures were taken and how recently, since the sensor may cool off again after usage. Therefore the exact background is very difficult to produce in a CCD sensor. However, in the center of the image, which is less prone to thermal noise, the noise level is zero after background subtraction.

Finally, Figure C.4 shown the image used to assess the streak camera's temporal resolution. The incoupling optics of the device are not optimized for the wavelength used, and therefore produce a larger-than-ideal beam waist on the photocathode, which is the limiting factor for temporal resolution. When the deflection voltage is turned off in the device, the image of the incoupling slit on the photocathode can be observed. The brighter spot in the middle corresponds to the PDC signal. Background is not visible, simply because the other recorded features are higher. The camera software automatically scales the

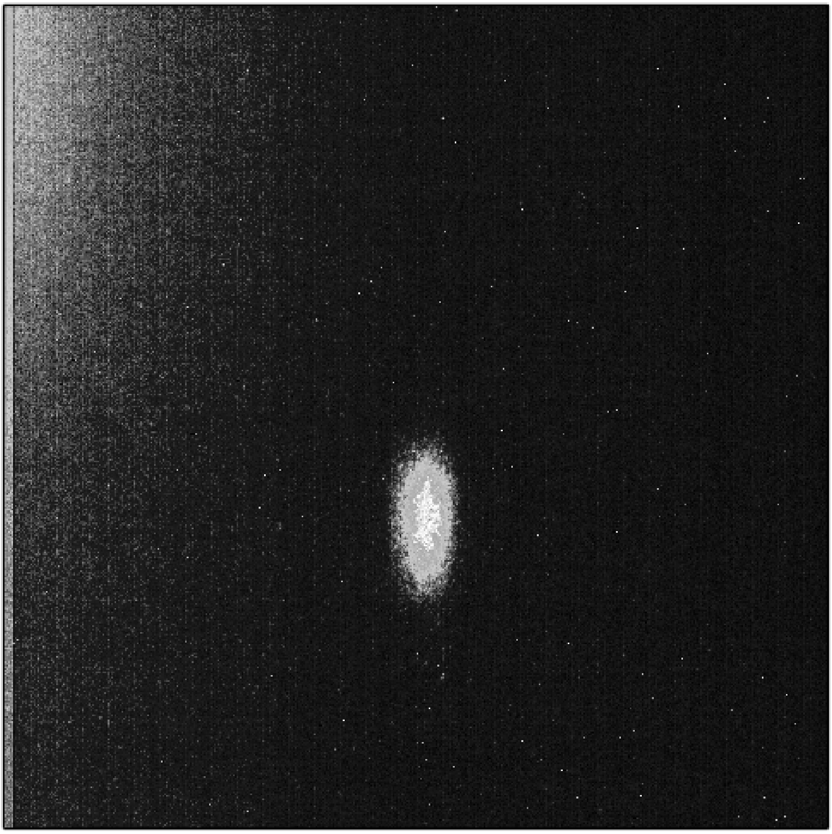

Figure C.1.: Raw image for the decorrelated state. The image was produced by the camera software by adding 32 consecutive exposures of 10 seconds each

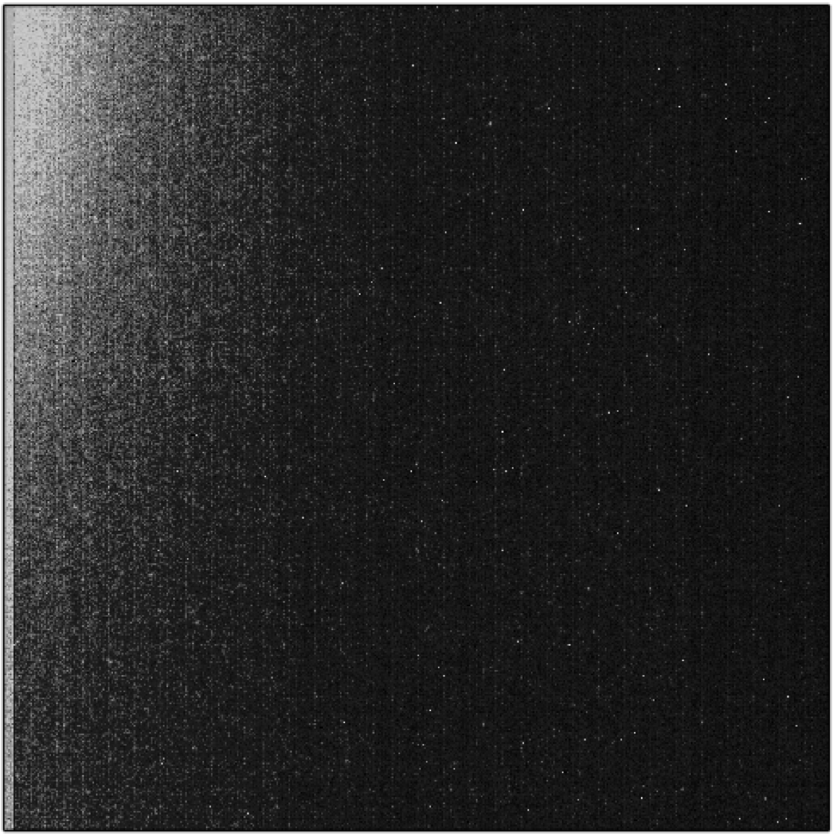

Figure C.2.: Raw background image. The image was produced by the camera software by adding 32 consecutive exposures of 10 seconds each

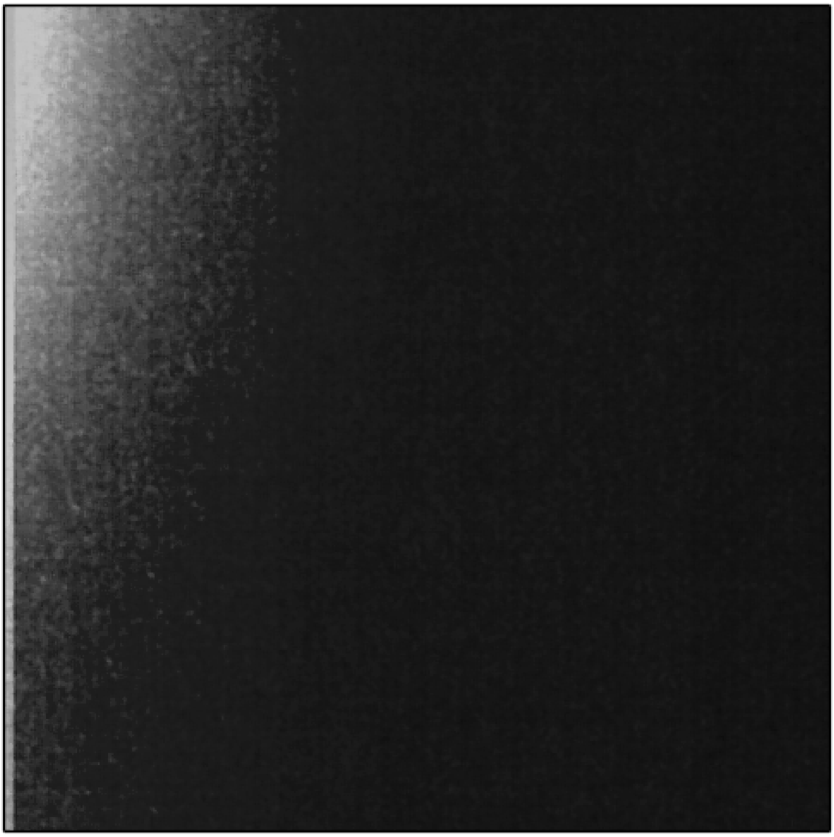

Figure C.3.: Raw background image after applying a median filter with a pixel radius of 7

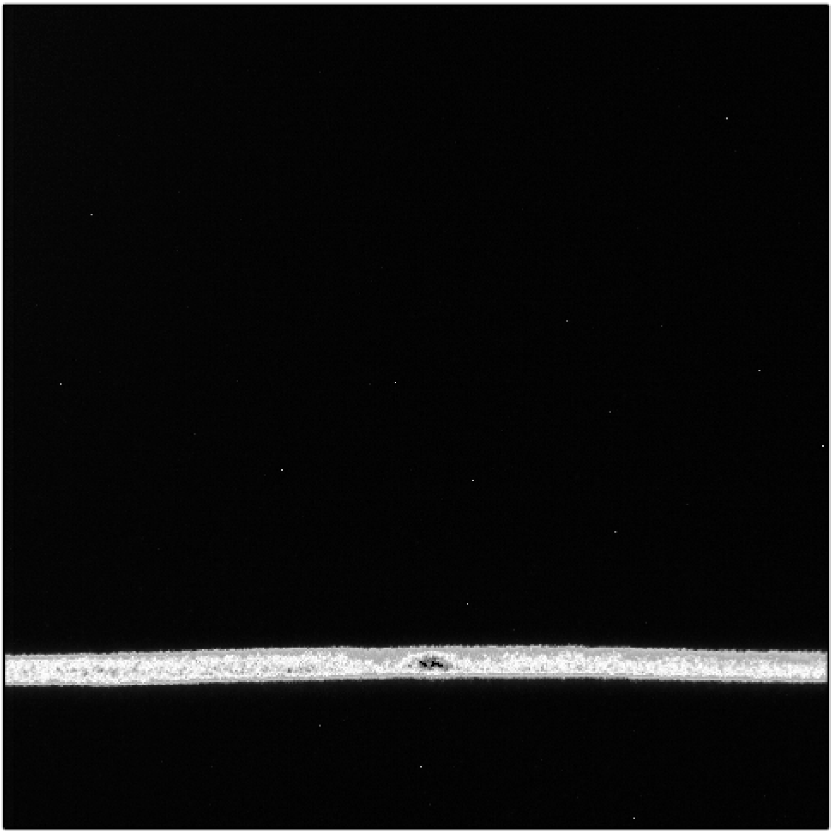

Figure C.4.: Raw image with the deflection voltage turned off

image information to make the best of the 8 bit pixel depth of the file format used. The width of the stripe was then measured using the software *ImageJ* to be 35 pixels, at a image resolution of 1024×1024 pixels. To convert this to temporal resolution, the total extend of the time interval imaged at a certain deflection voltage setting has to be considered. In this experiment, is was 220 ps corresponding to 1024 pixels. Therefore, the temporal resolution in this measurement was $220\mathrm{ps} \cdot 35/1024 = 7.5$.